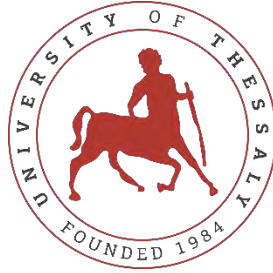UNIVERSITY OF THESSALY

SCHOOL OF ENGINEERING

DEPARTMENT OF MECHANICAL ENGINEERING

AERODYNAMIC DESIGN AND ANALYSIS OF A SOLAR POWERED UAV
(Unmanned Aerial Vehicle)

by

SAVVAS KOKKOS

AND

EFSTRATIOS MORFIDIS

Submitted in partial fulfillment of the requirements for the degree of Diploma
in Mechanical Engineering at the University of Thessaly

Volos, 2020

UNIVERSITY OF THESSALY

SCHOOL OF ENGINEERING

DEPARTMENT OF MECHANICAL ENGINEERING

AERODYNAMIC DESIGN AND ANALYSIS OF A SOLAR POWERED UAV
(Unmanned Aerial Vehicle)

by

SAVVAS KOKKOS

AND

EFSTRATIOS MORFIDIS

Submitted in partial fulfillment of the requirements for the degree of Diploma
in Mechanical Engineering at the University of Thessaly

Volos, 2020

Approved by the Committee on Final Examination:

Advisor   Dr. Pelekasis Nikolaos,

                 Professor, Department of Mechanical Engineering,
                 University of Thessaly

Member   Dr. Bontozoglou Vasilis,

                 Professor, Department of Mechanical Engineering,
                 University of Thessaly

Member   Dr. Stamatelos Anastasios,

                 Professor, Department of Mechanical Engineering,
                 University of Thessaly

Date Approved: [February   , 2020]

AERODYNAMIC DESIGN AND ANALYSIS OF A SOLAR POWERED UAV (Unmanned Arial Vehicle)

SAVVAS KOKKOS

EFSTRATIOS MORFIDIS

Department of Mechanical Engineering, University of Thessaly, 2020

Supervisor: Dr Nikolaos Pelekasis

Professor of Computational Fluid Dynamics

Abstract

This thesis studies the design of a solar powered unmanned aerial vehicle (UAV) with maximum altitude 2000 m that can complete a whole 24 h flight. The analysis uses sun data of the summer season in Greece and by making a first estimation of lift and drag coefficients the study that follows proves that theoretically the concept can be achieved. Besides the sun data the electrical components with the whole composite material weight was estimated using an EXCEL spreadsheet. Having selected the 2D airfoil profiles the study uses the XFLR5 environment to extract the lift and drag coefficients of an arbitrary wing with planform bottom view and then utilizes initially the lifting line theory to get an estimation of the wing aerodynamic behavior. Then the comparison, based on efficiency criteria with the most important one to be the watt consumption of the drag force, takes place and the airfoil that best matches the preferences of the project is used to create the 3D wing. For the validation of the results an experimental setup that calculates the pressure distribution over a 2D foil was introduced but left as future work. After reaching a mesh independent solution using the ANSYS Fluent environment the aero map of the wing was calculated and used to define the optimal Angle of Attack of the selected wing. At this time the fuselage design takes place and comparing the types of the fuselages that Gundmundson introduces two concepts were

chosen. Further study took place in order to achieve the elliptical lift distribution to eliminate the induced drag and the final design of the fuselage the one with embedded wings was finalized. Then knowing the place of the center of pressure and the position of the center of mass, using the xflr5 environment after the stability analysis took place the final geometrical parameters of the tail were calculated and the whole UAV was finalized. As future work has been left the PID tuning of the control surfaces and the experimental setup validation.

ΑΕΡΟΔΥΝΑΜΙΚΟΣ ΣΧΕΔΙΑΣΜΟΣ ΚΑΙ ΑΝΑΛΥΣΗ ΗΛΙΟ-ΤΡΟΦΟΔΟΤΟΥΜΕΝΟΥ ΜΕΑ
(Μη Επανδρωμένο Αεροσκάφος)

ΣΑΒΒΑΣ ΚΟΚΚΟΣ

ΕΥΣΤΡΑΤΙΟΣ ΜΟΡΦΙΔΗΣ

Τμήμα Μηχανολόγων Μηχανικών, Πανεπιστήμιο Θεσσαλίας, 2020

Επιβλέπων Καθηγητής: Δρ. Νικόλαος Πελεκάσης,

Καθηγητής Υπολογιστικής Ρευστοδυναμικής

Περίληψη

Στην παρούσα διπλωματική εργασία μελετάται ο αεροδυναμικός σχεδιασμός ενός ηλιοτροφοδοτούμενου μη επανδρωμένου αεροσκάφους με ικανότητα πτήσης έως 2000 m, το οποίο καλείται να ολοκληρώσει μια πτήση 24 ωρών. Η ανάλυση που ακολουθεί χρησιμοποιεί δεδομένα ηλιακής ακτινοβολίας κατα τις καλοκαιρινές περιόδους στην Ελλάδα και με μία πρώτη εκτίμηση των αεροδυναμικων συντελεστών οπισθέλκουσας και άνωσης η ανάλυση αποδεικνύει ότι θεωρητικά ο στόχος μπορεί να επιτευχθεί. Μετά από έναν ενδελεχή προσδιορισμό του βάρους όλων των ηλεκτρονικών κομματιών που θα χρησιμοποιηθούν καθώς και του βάρους της κατασκευής αυτής καθαυτής γίνεται μία αρχική εκτίμηση του βάρους του μη επανδρωμένου οχήματος. Μετά από την συγκέντρωση αεροτομών που σαν κύριο χαρακτηρηστικό έχουν την μεγάλη απόδοση χρησιμοποιήθηκε το περιβάλλον του XFLR5 προκειμένου να προσδιοριστούν οι διδυαστατοι αεροδυναμικοί συντελεστές της εκάστωτε αεροτομής και εν συνεχεία με την χρήση της μεθόδου της γραμμής άνωσης προσδιορίσθηκαν τα χαρακτηρηστικά ενός φτερου ορθογωνικής κάτοψης που έχει την αντίστοιχη αεροτομή σαν προφιλ. Έχοντας θέσει κάποια κριτήρια σχετικά με την απόδοση των αεροτομών ακολουθεί μια σύγκριση αυτών προκειμένου να επιλεγεί η πίο κατάλληλη για το πρότζεκτ μας. Φυσικά επειδή η θεωρία απέχει από την πραγματικότητα προτάθηκε μια πειραματική διάταξη η οποία υπολογίζει το προφίλ των πιέσεων πάνω από

μια πτέρυγα, κάτι το οποίο όμως αφέθηκε για να γίνει στο μέλλον. Σε αυτό το σημείο όλοι οι υπολογισμοί που έλαβαν χώρα δεν είχαν συνυπολογίσει την συμμετοχή της τριβής μεταξύ του ρευστού και των μοντέλων μας στραφήκαμε στο ANSYS προκειμένου να χρησιμοποιήσουμε ένα μοντέλο τύρβης και να εξάγουμε έναν χάρτη των αεροδυναμικών δυνάμεων προκειμένου να καθορίσουμε την βέλτιστη γωνία προσβολής της πτέρυγας. Ακολουθώντας τις προτάσεις του Gundmundson για το είδος της ατράκτου που μπορεί να χρησιμοποιηθεί συγκρίναμε 2 είδη. Το πρώτο είναι κυλινδρικό ενώ το δεύτερο έχει ενσωματωμένες τις πτέρυγες με τον κυρίως κορμό. Επεκτείναμε την μελέτη των παραμέτρων της πτέρυγας και αλλάξαμε γεωμετρικά χαρακτηρηστικά όπως την συστροφή το είδος και το πάχος της αεροτομής προκειμένου να επιτύχουμε την ελλειπτική κατανομή της άνωσης κατα μήκος του εκπετάσματος του φτερού καταφέρνοντας να εκμηδενίσουμε την επαγώμενη συνιστώσα της οπισθέλκουσας δύναμης. Έχοντας πλέον στα χέρια μας την θέση του κέντρου βάρους και του κέντρου πίεσης μπορούμε πλέον να ολοκληρώσουμε τον σχεδιασμό με την οριστικοποίηση των διαστάσεων της ουράς του μη επανδωμένου οχήματος στέφοντας την προσοχή μας στην ανάλυση ευστάθειας μέσω του προγράμματος XFLR5. Σαν μελλοντική δουλειά αφέθηκε η εκτέλεση του πειράματος που προτάθηκε ανωτέρω καθώς και η βελτιστοποίηση των ενισχύσεων του PID ελεγκτή για τις κινητές επιφάνειες ελέγχου.

Λέξεις-κλειδιά:

Table of Contents

Table of Figures

Chapter1: Introduction

1.1.   Motivation and Objectives

The field of application of energy autonomous UAV is extremely wide. Worldwide there are examples of its application like Human rescue situations, wildlife surveillance, fire detection, observation of inaccessible territories for example radioactive areas as also emissions measurement.

These applications would require remaining airborne during days, weeks or even months. For the moment, it is only possible to reach such ambitious goals using electric solar powered platform. Photovolataic modules may be used to collect the energy of the sun during the day, one part being used directly to power the propulsion unit and onboard instruments, the other part being stored for the night time.

The design manufacturing of an UAV underlies a huge field of study and parts that need to be taken into consideration for making a project like this take flesh and bone. The whole project needs to be split into objectives to be studied separately and in combination with each other since there are compensations to be done in order to find a setup-solution to meet our goal. The goal will be the endurance of the flight off duty which means that the primal goal is the 24-hour flight. If this goal achieved, it is very possible that the duration of the fight will be defined from the sunlight day after day.

The field of the applications is such that a quick responsiveness is not required and in our case will be avoided. The big deal in our case is the steady flight with an acceptable range of flight weather conditions. In terms of automatic control and stability we want our system to be robust, aerodynamically efficient and to have the tendency to reject external disturbances that can be caused from wind fluctuations, with as smaller flight controller's interference as possible.

1.2. History of Solar Powered Flight

1.2.1. The Conjunction of two Pioneer Fields, Electric Flight and Solar Cells

The use of electric power for flight vehicles propulsion is not new. The first one was the hydrogen-filled dirigible France in year 1884 that won a 10 km race around Villacoulbay and Medon. At this time, the electric system was superior to its only rival, the steam engine, but then with the arrival of gasoline engines, work on electrical propulsion for air vehicles was abandoned and the field lay dormant for almost a century. On the 30th of June 1957, Colonel H. J. Taplin of the United Kingdom made the first officially recorded electric powered radio controlled flight with his model "Radio Queen", which used a permanent-magnet motor and a silver-zinc battery. Unfortunately, he didn't carry on these experiments. Further developments in the field came from the great German pioneer, Fred Militky, who first achieved a successful flight with an uncontrolled model in October1957. Since then, electric flight continuously evolved with constant improvements in the fields of motors and batteries. Three years before Taplin and Militky's experiments, in 1954, photovoltaic technology was born at Bell Telephone Laboratories. Daryl Chapin,Calvin Fuller, and Gerald Pearson developed the first silicon photovoltaic cell capable of converting enough of the sun's energy into power to run every day electrical equipment. First at 4 %, the efficiency improved rapidly to 11%.Two more decades will be necessary to see the solar technology used for the propulsion of electric model airplanes.

1.2.2. Early Stages of Solar Aviation with Model Airplane

On the 4th of November 1974, the first flight of a solar powered aircraft took place on the dry lake at Camp Irwin, California. Sunrise I, designed by R.J.Boucher from Astro Flight Inc. under a contract with ARPA, flew 20 minutes at an altitude of around 100m during its inaugural flight. It had a wing span of 9.76 m, weighed 12.25 kg and the power output of the 4096 solar cells was450W. Scores of flights for three to four hours were made during the winter, but Sunrise I was seriously damaged when caught flying in a sandstorm. Thus, an improved version, Sunrise II, was built and tested on the12th of September 1975. With the same wingspan, its weight was reduced to10.21 kg and the 4480 solar cells were able this time to deliver 600W thanks to their 14% efficiency. After many weeks of testing, this second

version was also damaged due to a failure in the command and control system. Despite all, the history of solar flight was engaged and its first demonstration was done.

Figure 1-1: Sunrise I (1974) and Solaris (1976)

On the other side of the Atlantic, Helmut Bruss was working in Germany on a solar model airplane in summer 1975 without having heard anything about Boucher's project. Unluckily, due to overheating of the solar cells on his model, he didn't achieve level flight and finally the first one in Europe was his friend Fred Militky, one year later, with Solaris. On the 16th of August 1976, it completed three flights of 150 seconds reaching the altitude of 50m. Since this early time, many model airplane builders tried to fly with solar energy, this passion becoming more and more affordable. Of course, at the beginning, the autonomy was limited to a few seconds, but it rapidly became minutes and then hours. Some people distinguished themselves like Dave Beck from Wisconsin,USA, who set two records in the model airplane solar category F5 open SOLof the FAI. In August 1996, his Solar Solitude flew a distance of 38.84kmin straight line and two years later, it reached the altitude of 1283m.The master of the category is still Wolfgang Schaeper who holds now all the official records: duration (11h 34min 18s), distance in a straight line(48.31 km), gain in altitude (2065 m), speed (80.63 km/h), distance in a closed-circuit (190 km) and speed in a closed circuit (62.15 km/h). He achieved these performances with Solar Excel from 1990 to 1999 in Germany.

.
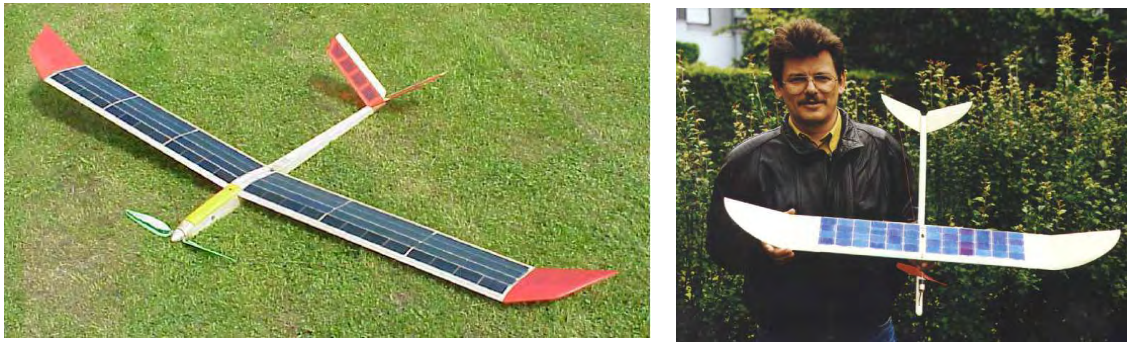
Figure 1-2: Solar Excel (1990) and PicoSol (1998)

We can mention as well the miniature models MikroSol, PicoSol and NanoSol of Dr. Sieghard Dienlin. PicoSol, the smallest one, weighs only 159.5 g for a wingspan of 1.11m and its solar panels can provide 8.64 W.

1.2.3. The Dream of Manned Solar Flight

After having flown solar model airplanes and proved it was feasible with sufficient illumination conditions, the new challenge that fascinated the pioneers at the end of the 70's was manned flights powered solely by the sun. On the 19th of December 1978, Britons David Williams and Fred Tolaunched Solar One on its maiden flight at Lasham Airfield, Hampshire. First intended to be human powered in order to attempt the Channelcrossing, this conventional shoulder wing monoplane proved too heavy and thus was converted to solar power. The concept was to use nickel-cadmium battery to store enough energy for short duration flights. Its builder was convinced that with high-efficiency solar cells like the one used on Sunrise, he could fly without need of batteries, but their exorbitant price was the onlylimit. On April 29, 1979, Larry Mauro flew for the first time the Solar Riser, a solar version of his Easy Riser hang glider, at Flabob Airport, California. The 350Wsolar panel didn't have sufficient power to drive the motor directly and was here again rather used as a solar battery charger. After a three hours charge the nickel-cadmium pack was able to power the motor for about ten minutes. His longest flight covered about 800m at altitudes varying between1.5m and 5m.This crucial stage consisting in flying with the sole energy of the sun without any storage was reached by Dr. Paul B. McCready and AeroVironmentInc, the company he founded in 1971 in Pasadena, California. After having demonstrated, on August 23, 1977, sustained and

maneuverable human-powered flight with the Gossamer Condor, they completed on June12, 1979 a crossing of the English Channel with the human-powered GossamerAlbatross. After these successes, Dupont sponsored Dr. MacCreadyin an attempt to modify a smaller version of the Gossamer Albatross, called Gossamer Penguin, into a man carrying solar plane. R.J. Boucher, designer of Sunrise I and II, served as a key consultant on the project. He provided the motor and the solar cells that were taken from the two damaged versions of Sunrise. On the 18th of May 1980, the Gossamer Penguin, with 13 years old MacCready's son Marshall on board, realized what can be considered as the world's first piloted, solar powered flight.

Figure 1-3: Gossamer Penguin (1980) and its successor, Solar Challenger (1981)

However, the Gossamer Penguin was not safe for a pilot flying at more than a few feet above ground. The Dupont Company, encouraged by the results of the Gossamer Penguin, sponsored MacCready for building a new solar airplane that would cross the English Channel. The Solar Challenger was a 14.2m wingspan high-wing monoplane with 16 128 solar cells offering2500W at sea level. On July 7, 1981, it flew from Puntoise-Cormeilles near Paris to Manston RAF Base near London in 5 hours 23 minutes covering262.3 km, with solar energy as its sole power source and no onboard energy storage system.

As they were in England, the members of the Solar Challenger team were surprised to hear for the first time about a German competitor who was trying to realize exactly the same performance at the same time from Biggin Hill airport. Günter Rochelt was the designer and builder of Solair I, a 16m wingspan solar airplane based on the Canard 2FL from AviaFiber that he slightly modified and covered with 2499 solar cells providing 1800 W. He invited members of the Solar Challenger team to visit him and R.J. Boucher, who accepted the invitation, was very impressed by the quality of the airplane. However, with a little more than half the wing area of solar cells, Solair I didn't have enough energy to climb and thus incorporated a 22.7 kg nickel-cadmium battery. Rochelt didn't realize the Channel crossing this year but on the 21st of August 1983 he flew in Solair I, mostly on solar energy and also thermals, rising currents of warm air, during 5 hours 41 minutes. In 1986, Eric Raymond started the design of the Sunseeker in the United States. The Solar Riser in 1979, Solar Challenger two years later and a meeting with Günter Rochelt in Germany had convinced him to build his own manned solar powered aircraft. At the end of 1989, the Sunseeker was test flown as a glider and during August 1990, it crossed the USA in 21 solar powered flights with 121 hours in the air.

Figure 1-4: Icaré 2 (1996) and Solair II (1998)

In Germany, the town of Ulm organized regularly aeronautical competitions in the memory of Albrecht Berblinger, a pioneer in flying machines 200 years ago. For the 1996 event, they offered attractive prizes to develop a real, practically usable solar aircraft that should be able to stay up with at least half the solar energy a good summer day with clear sky can give. This competition started activities round the Earth and more than 30 announced projects, but

just some arrived and only one was ready to fly for the final competition. On the 7th of July, the motor glider Icaré 2 of Prof. Rudolf Voit-Nitschmann from Stuttgart University won the 100,000DM price. Two other interesting competitors were O Sole Mio from the Italian team of Dr. Antonio Bubbico and Solair II of the team of Prof. Günter Rochelt who took profit of the experiences gained with the Solair I. Both projects were presented in an advanced stage of development, but were not airworthy at the time of the competition. The first flight of Solair II took place two years later in May 1998.

1.2.4. On the Way to High Altitude Long Endurance Platforms and Eternal Flight

After the success of Solar Challenger, the US government gave funding to AeroVironment Inc. to study the feasibility of long duration, solar electric flight above 19 812km (65 000 ft). The first prototype HALSOL proved the aerodynamics and structures for the approach, but it suffered from its subsystem technologies, mainly for energy storage, that were inadequate for this type of mission. Thus, the project took the direction of solar propulsion with the Pathfinder that achieved its first flight at Dryden in 1993. When funding for this program ended, the 30m wingspan and 254 kg aircraft became a part of NASA's Environmental Research Aircraft Sensor Technology (ERAST) program that started in 1994. In 1995, it exceeded Solar Challenger's altitude record for solar powered aircraft when it reached 15392m (50 500 ft) and two years later he set the record to 21 802m (71 530 ft). In 1998, Pathfinder was modified into a new version, Pathfinder Plus, which had a larger wingspan and new solar, aerodynamic, propulsion and system technologies. The main objective was to validate these new elements before building its successor, the Centurion. Centurion was considered to be a prototype technology demonstrator fora future fleet of solar powered aircrafts that could stay airborne for weeks or months achieving scientific sampling and imaging missions or serving as telecommunications relay platforms [17]. With a double wingspan compared to Pathfinder, it was capable to carry 45 kg of remote sensing and data collection instruments for use in scientific studies of the Earth's environment and also 270 kg of sensors, telecommunications and imaging equipment up to24 400m (80 000 ft) altitude. A lithium battery provided enough energy to the airplane for two to five-hour flight after sunset, but it was insufficient to fly during the entire night.

Figure 1-5: Centurion (1997-1999) and Helios (1999-2003).

The last prototype of the series designated as Helios was intended to be the ultimate "eternal airplane", incorporating energy storage for night-time flight. For NASA, the two primary goals were to demonstrate sustained flight at an altitude near 30 480m (100 000 ft) and flying non-stop for at least 24 hours, including at least 14 hours above 15 240m (50 000 ft). In 2001, Helios achieved the first goal near Hawaii with an unofficial world-record altitude of 29 524m (96 863 ft) and a 40-minute flight above 29 261m (96 000 ft). Unfortunately, it never reached the second objective as it was destroyed when it fell into the Pacific Ocean on June 26, 2003 due to structural failures.

In Europe, many projects were also conducted on high altitude, long endurance (HALE) platforms. At the DLR Institute of Flight Systems, Solitair was developed within the scope of a study from 1994 to 1998. The solar aircraft demonstrator was designed for year-around operations in northern European latitude by satisfying its entire onboard energy needs by its solar panels. So far, a 5.2m wingspan proof-of-concept model aircraft was built with adjustable

solar panels for optimum solar radiation absorption. Flight tests were achieved and various projects are still carried out on this scaled version.

The Helinet project, funded by a European Program, ran between January 2000 and March 2003 with the target to study the feasibility of a solar powered high altitude platform of 73m wingspan and 750 kg named Heliplat. It was intended to be used for broadband communications and Earth observation. The project involved ten European partners and led to the construction of a 24m wingspan scale prototype of the structure. Politecnico di Torino, the overall coordinator, is still leading research on Heliplat and also on a new platform named Shampo.
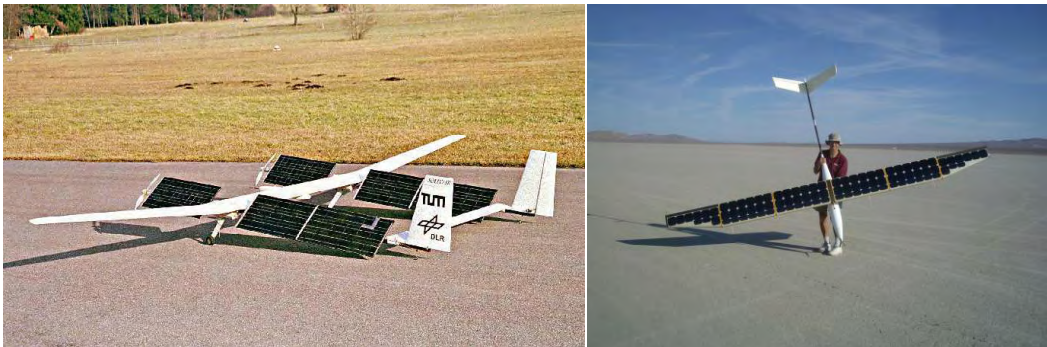
Figure 1-6: Solitair (1998) and Solong (2005)

The objective of Helios to prove the feasibility of eternal flight for an unmanned airplane was reached on the 22nd of April 2005. Alan Cocconi, president and founder of AcPropulsion, flew his Solong during 24 hours and 11 minutes using only solar energy coming from its solar panels and also thermals. The 4.75m wingspan and 11.5 kg airplane confirmed its capabilities two months later, on the 3rd of June, with a flight lasting 48 hours and 16 minutes taking place in California's Colorado Desert.

QinetiQ, a British company, is also very active in the field of solar HALE platforms. Two Zephyr aircrafts were first tested in New Mexico in December 2005, achieving a maximum duration of 6 hours and reaching an altitude of 7 925m (26 000 ft). After an 18-hour flight in July 2006, one Zephyr exceeded the official world record time for the longest duration unmanned flight with a 54-hour flight in New Mexico on the 10th of September 2007, reaching a maximum altitude of 17 786m (58 355 ft). Weighing only 30 kg for 18m wingspan, the aircraft used solar power for the ascent, reverting to Lithium-Sulphur battery power as

dusk fell. QinetiQ expects in the future flight duration of some months at an altitude above 15 240m (50 000 ft).Zephyr has recently been selected as the base platform for the Flemish

HALE UAV remote sensing system Mercator in the framework of the Pegasus project. The targeted platform should be able to carry a 100 kg payload in order to fulfill its missions that are forest fire monitoring, urban mapping, coastal monitoring, oil spill detection and many others.

Figure 1-7: Zephyr (2005) and the future Solar Impulse

The next dream to prove continuous flight with a pilot on board will perhaps come true with Solar-Impulse, a project officially announced in Switzerland in 2003. A nucleus of twenty-five specialists, surrounded by some forty scientific advisors from various universities like EPFL, is working on the 80m wingspan, 2000 kg lightweight solar airplane. After the manufacturing of a 60m prototype in 2007-2008 and the final airplane in 2009-2010, a round-the-world flight should take place in May 2011 with a stopover on each continent.

Of course History is still going on. In early 2007, the DARPA announced the launch of a new solar HALE project. The Vulture air vehicle program aims at developing the capability to deliver and maintain a single 453 kg(1000 lbs.), 5 kW airborne payload on station for an uninterrupted period of at least 5 years.

1.3. Basic Principles

1.3.1. Airplane Aerodynamics

Like all other airplanes, a solar airplane has wings that constitute the lifting part. During steady flight, the airflow due to its relative speed creates two forces: the lift that maintains the airplane airborne compensating theweight and the drag that is compensated by the thrust of the propeller.
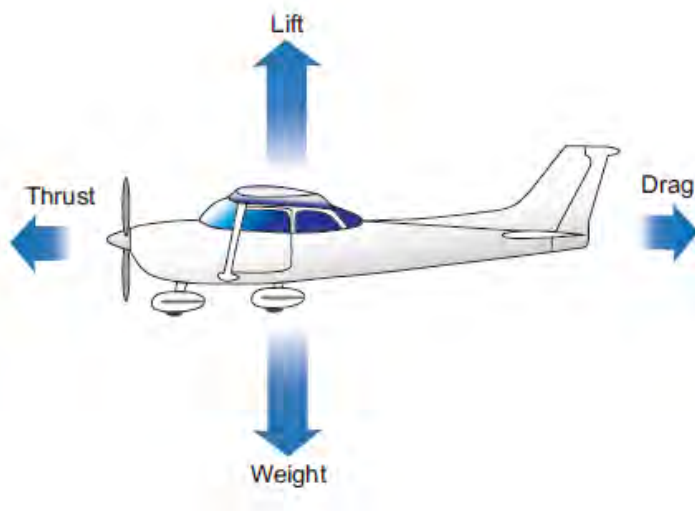
Figure 1-8: Forces acting on an airplane at level flight

The solar panels, composed by solar cells connected in a defined configuration, cover a given surface of the wing or potentially other parts of the airplane like the tail or the fuselage. During the day, depending on the sun irradiance and elevation in the sky, they convert light into electrical energy. A converter ensures that the solar panels are working at their maximum power point. That is the reason why this device is called a Maximum Power Point Tracker, that we will abbreviate MPPT. This power obtained is used firstly to supply the propulsion group and the onboard electronics, and secondly to charge the battery with the surplus of energy.
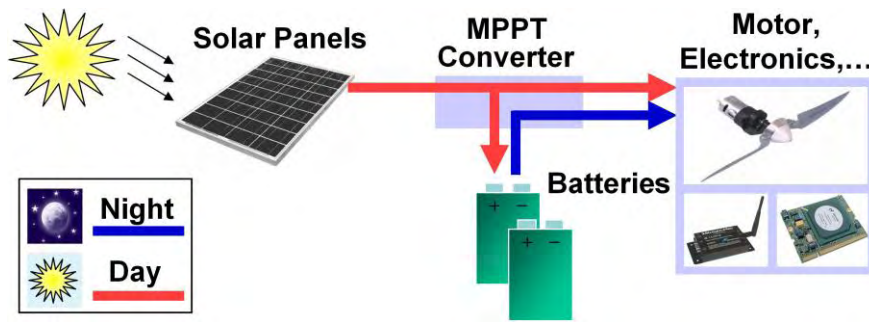
Figure 1-9: Solar airplane basic principle.

1.3.2. Airfoil Dynamics

The following Figure shows the cross section of a wing in a laminar airflow with a constant speed v. The circulation of this airflow creates a different pressure distribution on the upper and lower side of this section that once integrated can be represented as two forces, the lift and the drag. These forces can be calculated using the following equations:
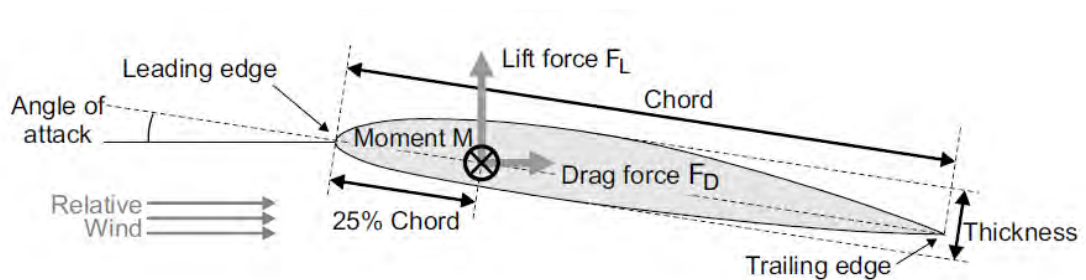
Figure 1-10: Section of an airfoil

$$F_L = C_L \frac{\rho}{2} A u^2$$

$$F_D = C_D \frac{\rho}{2} A u^2$$

Where C_L and C_D are respectively the lift and drag coefficients, ρ is the air density, A the wing area and u the relative airspeed. The CL and CD heavily depend on the airfoil, the angle of attack and the Reynolds number Re which is representative of the air flow viscosity.

$$Re = \frac{\rho u c}{\mu} = \frac{u c}{\nu}$$

Here, μ is the dynamic viscosity that once divided by the air density gives the kinematic viscosity ν and c represents the chord. The dependency on the angle of attack is depicted in figure 10. Increasing it makes the CL increase, but progressively the flow separates from the airfoil starting at the trailing edge and this lets place to a turbulent zone that makes the CD increase. At stall, the lift is maximum but the drag is high too. After this point, the behavior is more difficult to predict or simulate, but basically the drag still increases but without being followed by the lift that drops. Thus, the interesting and safe zone for an airplane is before the stall point, for glider especially at the point where the glide ratio CL/CD is maximum.
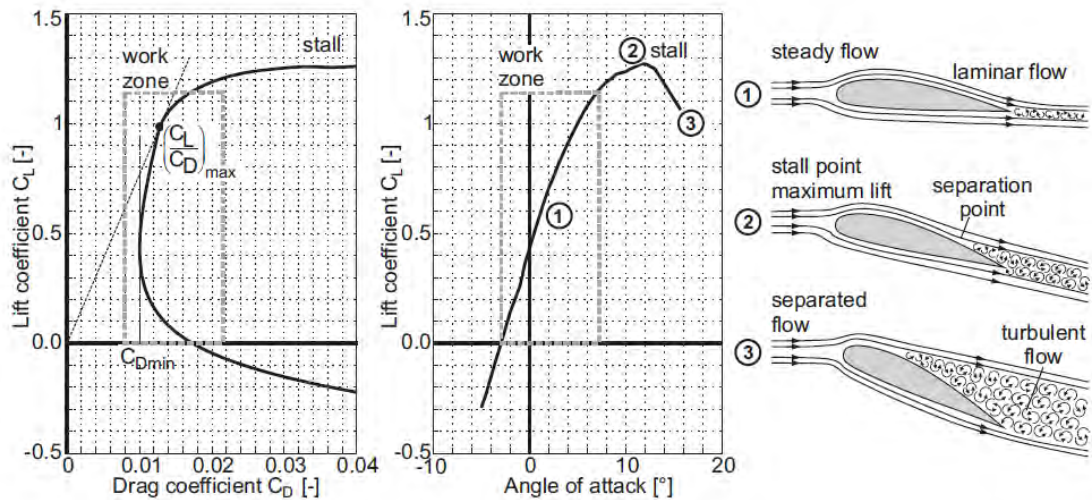
Figure 1-11: Lift and drag coefficients depending on the angle of attack

What was depicted so far is the case of an infinite length wing and inviscid flow but for a real wing, the total drag is the sum of five components:

- C_0 is the drag due to pressure difference
- C_{Di} is the induced drag that is generated from the wingtip vortex
- C_{DS} is the overall shear stress due to friction between the wing and the fluid
- C_{Dw} is created since the object disturbs the surround fluid and a wave extending from the wing is generated pushing outwards the surroundings and this change in momentum is added to the overall drag.

C_{D0}:   Visualizing the flow around and object with the help of steam, we can observe high and low streamline density areas. When the streamlines are closer one to other the fluids speed is greater than areas with greater distance between the streamlines and from Bernoulli's principle we can find out that the first region has lower and the second one greater than the free stream pressure. The integral of the pressure around the airfoil will give us the resultant force which is always perpendicular to the mean airfoil camber as shown below. The projection of this force in an axis parallel to the free stream flow will give us the first term of the drag force which is caused by this pressure difference between the upper and lower surface.

C_{DS}: Since the flow is not inviscid and there is friction between the wing skin and the fluid around it there will be another term that increases drag. This term is called the skin friction drag coefficient and the amplitude of the shear stress is a function of the flow and fluid characteristics:

$$\tau_{xy}=f(Re,\mu,u,P)$$

C_{Di}: Scaling up from the two to three dimensions every finite wing faces a problem that causes the angle if incidence differ from angle of attack that was desired. The final angle of incidence $\alpha_{eff}=\alpha_0-\alpha_i$ where α_0 is the desired angle of attack and α_i is the induced angle of attack because of the downwash created velocity term.

$$\vec{L} = \rho\vec{V} \times \vec{\Gamma}$$

We can extract from the relation above that the lift vector is perpendicular to both velocity and circulation. Since the downwash crated a velocity pointing downwards the result is that the lift vector is now pointing backwards and this creates a new drag term, the induced one.

1.4.   Type of UAVs

1.4.1. Monoplane

A monoplane is a fixed-wing aircraft with a single main wing plane, in contrast to a biplane or other multiplane, each of which has multiple planes. A monoplane has inherently the highest efficiency and lowest drag of any wing configuration and is the simplest to build. However, during the early years of flight, these advantages were offset by its greater weight and lower maneuverability, making it relatively rare until the 1930s. Since then, the monoplane has been the most common form for a fixed-wing aircraft.

Figure 1-12: VTOL Vehicles

1.4.2. VTOL Vehicles

A vertical take-off and landing (VTOL) aircraft is one that can hover, take off, and land vertically. This classification can include a variety of types of aircraft including fixed-wing aircraft as well as helicopters and other aircraft with powered rotors, such as cyclogyros/ cyclocopters and tiltrotors.

Figure 1-13: VTOL Fixed Wing UAV

1.4.3. Multicopters

A multicopter is a rotorcraft with more than two rotors. An advantage of multirotor aircraft is the simpler rotor mechanics required for flight control. Unlike single and double-rotor helicopters which use complex variable pitch rotors whose pitch varies as the blade

rotates for flight stability and control, multirotors often use fixed-pitch blades. Control of vehicle motion is achieved by varying the relative speed of each rotor to change the thrust and torque produced by each.

Due to their ease of both construction and control, multirotor aircraft are frequently used in radio control aircraft and UAV projects in which the names tricopter, quadcopter, hexacopter and octocopter are frequently used to refer to 3-, 4-, 6- and 8-rotor rotorcraft, respectively.

Figure 1-15: Tricopter

Figure 1-14: Quadcopter

Figure 1-17: Hexacopter

Figure 1-16: Octocopter

Chapter2: Preliminary Analysis

The monoplane selection for the purpose of our application give us plenty of room for tuning and modification in the geometry while still maintaining a very simplistic and delicate way of achieving our goal. The greatest advantage among different kinds of aerial vehicles is the large wing areas that is necessary to exist in order to acquire enough irradiation from the sun for the whole system to function in the desired point. At this point we need to do some preliminary calculation and analysis in order to acquire the desired goals for the aerodynamic coefficients and the area need for the solar energy gathering.

2.1 Solar Irradiance in Greece

The irradiance depends on a lot of variables such as geographic location, time, plane orientation, weather conditions and albedo that represents the reflection on the ground surface. A typical diagram of solar irradiation during day can be seen below. The interpolated data can be then integrated and acquire either the average amount of irradiation or the total amount of irradiance that is emitted over an area. Our goal here is to use some average values and see weather our solar powered UAV can be used throughout the year or if it is restricted from weather conditions during winter season. Radiation data for the city of Volos show that the irradiation ranges from 1.93 kWh/m^2/day up to 6.85 kWh/m^2/day which corresponds to 80 and 285 W/m^2 respectively.
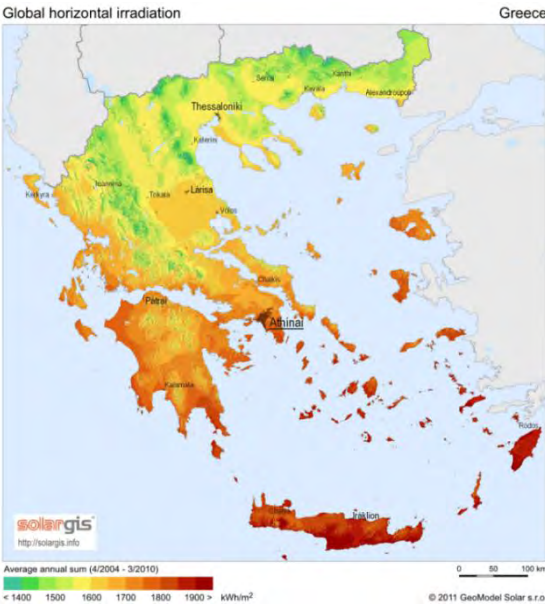
Figure 2-1: Solar Irradiance

Table 2-1: Solar Irradiance

Jan	Feb	Mar	Apr	May	Jun	Jul	Aug	Sep	Oct	Nov	Dec
1.93	2.60	3.64	4.80	5.64	6.85	6.74	6.06	4.69	2.97	1.93	1.55

The above table denotes the average solar insolation measured in $kWh/m^2/day$ .As can be seen the solar irradiation of the winter months with combination of the weather uncertainty and the lack of thermals that help the uav to gain altitude without the use of electrical energy do not indicate that the goal of 24hour flight can be achieved. Different sources of irradiation data were taken into account to crosscheck that the amount of the irradiance is not very far apart. Taking into consideration all the efficiencies of the electrical components, the motor and the gearbox we can calculate the desired power consumption based on the radiation or the radiation that needs to be emitted for the uav to fly during night.

2.1.1. Solar Cell Selection

One factor that defines the architecture of the wing itself and the making process is the kind of the solar cells that will be used in this project. Numerous avionics projects have proposed different ways of placing orientating and protecting the solar cells but most of them have some compensation between the integrity of the airfoil profile, the safety of the solar power itself and the efficiency of the whole array. The solar cell itself does determine in some way the size of the cord and the span. The number of the solar cells across the airfoil define the chord of it and the total energy that the system requires to operate is a function of the area of solar cell array that will be defined by the span of the wings. Besides choosing the architecture of the wing, the solar cells have to be the most effective so that our system does not lack of electrical energy. Even if the system can absorb as much energy as it needs in order to fly all night we also need to make sure that it is adequate while in mission where the target flying path is not to gather as much sun irradiation and maybe the gliding and the thermal

chasing process will be replaced by the desired mission. That said we can understand that there is no room for efficiency losses in the selection of the panels.

One mounting technique which is not very efficient is to take small rectangular stiff panels and stick them on the upper side of the wing. The benefit of this method is that the small area of each panel allows to cover even the tiniest gaps in the whole glider, and they play not a very important role in the wing dimensions. They can even cover the moving control areas like ailerons rudders etc without adding much weight. The major disadvantage of those cells is that the airfoil should not have great gradients in its geometry because the cells in order to be placed they will remove the curvature altering the whole geometry. One can think of it as integrating a continuous function with the trapezoid method. The final shape of the wing will be way different from the designed one and all the minor edges on the wing can cause early flow separation and thus decreasing the efficiency of the uav. This method was used as an initial concept in sunsailor (Israel 2006).

The second mounting technique is the safest for the solar cells themselves because they are encapsulated inside the wing and mounted on the spars and ribs of it. This method preceds that the architecture of the wing will not be made by composite materials as we plan but with some spar and rib grid and that the upper skin of the glider will be made by a transparent material. That way the cells may be very well protected by the surrounding wing but there are some serious disadvantages that make them unwanted for our purposes. First of all the spar and rib architecture is a pretty complicated structure that needs further study in order to get the desired stiffness of the wing. It can also result in a very bulky heavy and compact assembly without sufficient space for extra electronics after the manufacturing process. The encapsulation of the solar cells comes with the insufficient head disposal increasing the temperature inside the wing and thus decreasing the effectiveness of all the electronic components. But again the major disadvantage is that the geometry of the upper wing skin has to be made by a transparent material which in most cases is of a membrane type. The membrane might have adequate rigidity to endure hard maneuvering and temperatures but some of the irradiance will be reflected from the surface and they cannot guarantee that the geometry of the wing will remain as was designed.
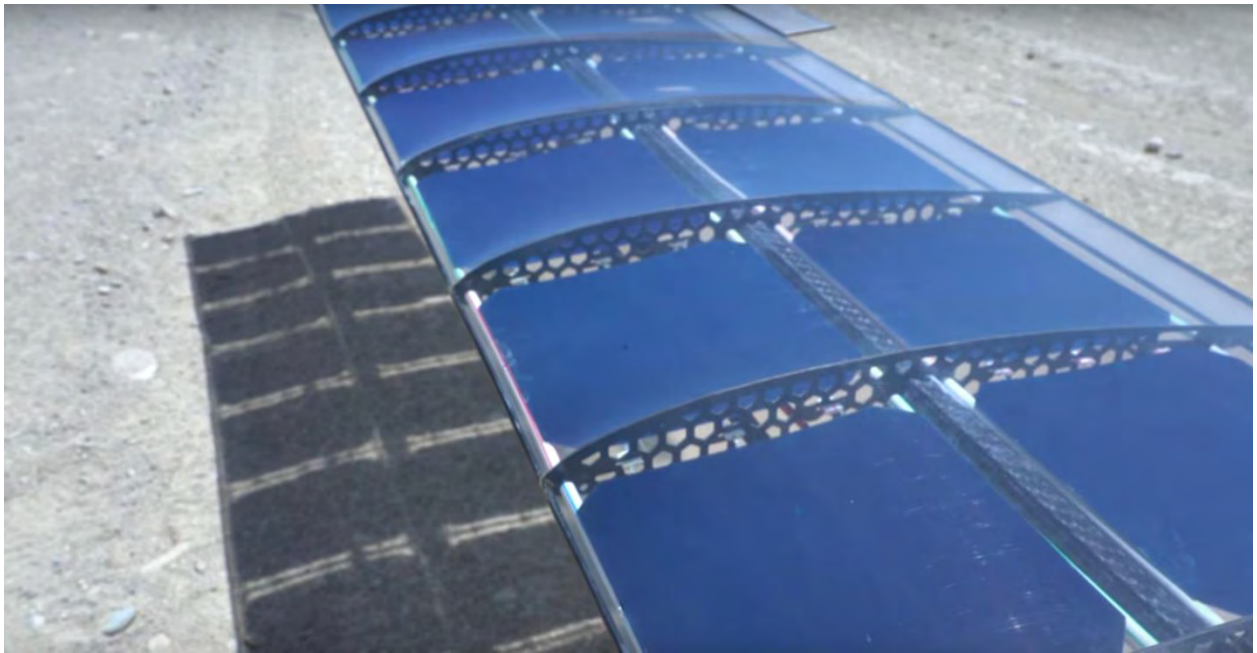
Figure 2-2: Encapsulated Solar Cells

The third and base on the above thoughts concept is to use flexible solar panels. As their name indicates the solar panels are flexible up to 45 degrees and their efficiency rises up to 24% which is one of the most efficient solar panel that exists today. They have rectangular shape with 12.5 mm side and as all the solar cells they can be connected serial or parallel based on the current and the voltage required. They can be mounted on the outter surface of the wings not effecting the manufacturing process and since they are flexible they can enfold the wing. They are only 0.3 mm thick and there is no need to create a slot in the wing in order to keep the curvature of the wing intact. As for the thermal behavior the placement in the outer surface of the construction will provide the desired cooling.

Figure 2-3: Flexible Solar Cells

The selection was very clear and without doubts. The Maxeon Gen II left no space for controversies for the type of the solar cell that will be used as well as for the type of the manufacturing process of the UAV. The composite combined with the foam is a robust material selection we previous validation in a race car aerodynamics package and the existence of the flexible solar panel allows us to use this method to incarnate our project.
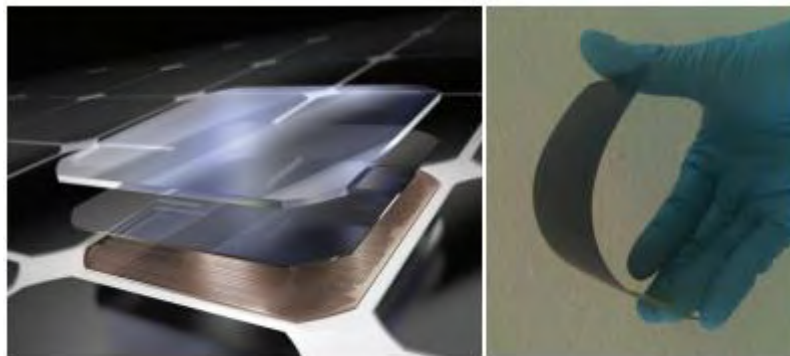
Figure 2-4: Maxeon Gen II

2.2.   UAV Type Selection

In chapter one we did present some of the aerial vehicles that exist today and some of them might be appropriate for surveillance but very few can be capable to succeed the 24-hour flight endurance time. All the multicopters and VTOL airplanes do have the advantage of the easiest control among the others but their power consumption exceeds our limitations.

Their major issue is that their shape consists of very small area for solar cell placement and even if they do the model becomes bulky and stiff and in most cases aesthetically poor. The ideal airplane shape is the monoplane because of its simplistic shape and the relative big area to weight ratio, it can be light weight and can absorb the amount of energy that we require. The other advantage of the monoplane is that the simplistic shape of it is that once knowing the airfoil profile there are only two variables do be defined, the chord and the span of the wing. Since we do need to place some cells on the outer surface we can understand that the chord cannot be arbitrary but it should have adequate space for the panels to be placed. Thus the chord has to be at least 12.5 cm times the rows of the solar cells that will be placed. In example one row of cells will result in a very long wing which is not desired because of the stress concentration in the base of the wing and a huge amount of cell rows will result in a very short wing and as we did present in the first chapter the smallest the aspect ratio the lower the efficiency of the wing. The answer will be found somewhere in the middle but we need do take into consideration that the airfoil profile should not have great gradients for the cells to be placed, to be placed in a small angle of attack for the greater sun irradiance absorbance and the chord of the wing will be such that the efficiency is great enough end the stresses can be handled by the composite material.

2.3.   Initial Sizing

The initial sizing method that is introduced in Snori Gudmundson General Aviation Airc is based on preliminary calculations and is based on thrust to weight ratio to define parameters of the UAV such us stall speed maximum lift coefficient cruising speed and then calculate based on standard tables the wing area of the airplane. Since we do not have yet chose an appropriate motor and propeller we need to find an alternative way to calculate the properties of the wing that we need. Furthermore, our analysis will be based on the level flight and will ignore the take off and the landing of the aerial vehicle. The initial calculations of the power consumption and the efficiencies of the electronics were taken from similar projects. The power needed is calculated as:

$$P_{out} = n_{propeller} n_{reducer} n_{MPPT} n_{electronics} n_{solar\_cells} * sun\_irradiation$$

Table 2-2: Electronics' efficiencies

$N_{propeller}$	$N_{reducer}$	N_{mppt}	$N_{electronics}$	N_{solar_cells}
0.85	0.95	0.97	0.93	0.24

Based on the irradiation data in Volos during the summer season the amount of daily irradiation is 250watt/m². For that irradiation power the Pout is equal to 46.0071 watt/m². This means that for a wing area of one square meter we need to have a drag power consumption of around 23 watts in order for the rest of the power to be stored in the batteries and used overnight. As Snori gundmundson indicates typical drag coefficient values for high efficiency devices are between 0.04-0.05 for Gliders and typical cruising speeds are around 10 m/s. So for those two values taking the worst scenario of the uav C_d coefficient which is 0.05 we can calculate the initial Area of the wing.

$$P_{drag} = \frac{1}{2}\rho C_D A u^3 \Leftrightarrow$$

$$46 = \frac{1}{2} * 1 * 0.05 * 10^3 A \Leftrightarrow$$

$$A = 1.84 \ m^2$$

We can round the area of the wing in 1.9m² making things more strict in order of drag power. So now that we do have the area of the wing we need to define the chord of it. As said before we need to have adequate space for the cells to be placed on it. The two concepts of placing one and three rows of cells are have disadvantages the first one in the margin of the stresses and the second one in the efficiency of the wing. Thus placing two series of panels will result in a chord that is more or less, greater than 25 centimeters. Considering that we need space for the ailerons and the leading edge section that the panels cannot be placed due to the tilt of them we can say that a sufficient chord will be in around 30 centimeters. The planform area of the wing is 1.84m² and with a 0.3 m chord the span of the wings will be 6meters long. All the above calculations are based on speeds that gliders fly and data that

were taken in literature. During the design process those dimensions are very likely to be altered to match our criteria.

2.3.1. Lifting Line Theory(LLT)

Based on Jan (Lan, 1997) who quotes Prandtl's the lifting line theory as a bridge to connect the 2D airfoil Cl and Cd coefficients with the 3D wing parameters we can have an expression of the wing aerodynamic coefficients with a very simply way just by using an Excel Sheet. As he denotes

From the Momentum Method:

According to the linear momentum principle, assuming uniform downwash over the span of the wing S':

$$L = \rho V(S'V)\frac{w_1}{V} = \rho w_1(S'V)$$

And from the Energy Method which relies that

The work done on the air mass per unit time equals the kinetic energy increase per unit time.

Therfore :

$$D_i V = \rho S'V \frac{w_1^2}{2}$$

Dividing by V yields:

$$D_i V = \rho S' \frac{w_1^2}{2}$$

Recalling Eqn:

$$L = \frac{D_i}{a_i} = \frac{\rho S' \frac{w_1^2}{2}}{\frac{w}{V}}$$

From this it follows that:

$$\rho w_1(S'V) = \rho S' \frac{V w_1^2}{2w}$$

From this, it is now seen that:

$$2w = w_1$$

This result means that the induced downwash far behind the wing is twice that of the downwash on the wing itself. The area, S' may be written as: $S' = \frac{\pi b^2}{4}$. Thus, it is seen that the equation may be written as:

$$L = \rho(2w)\frac{\pi b^2}{4}V$$

This is just another way of writing previous equation. Now solving for the downwash, w:

$$w = \frac{2L}{\rho \pi b V^2} = \frac{C_L q S V}{\pi q b^2} = \frac{C_L S V}{\pi b^2} = \frac{C_L V}{\pi A}$$

The angle, α_i may now be written as:

$$\alpha_i = \frac{w}{V} = \frac{C_L}{\pi A}$$

Also, it follows that:

$$D_i = L a_i = C_L q S \frac{C_L}{\pi A}$$

The induced drag coefficient can therefore be written as:

$$C_{D_i} = \frac{D_i}{qS} = \frac{C_L^2}{\pi A}$$

These equations are only valid for wings with uniform downwash distribution. The latter can be achieved only if the span loading of the wing is elliptical. It has been shown that in such a case the induced drag coefficient is a minimum. It is shown as Jan Roskam implies that this condition can be achieved using an elliptical planform. When, as is normally the case, the downwash distribution is not uniform, a correction factor "e" called Oswald efficiency factor is introduced to yield:

$$C_{D_i} = \frac{C_L^2}{\pi A e}$$

Therefore, the induced angle, α_i can be written as:

$$\alpha_i = \frac{C_L}{\pi A e}$$

Experimentally it has been found that e ranges from 0.85 to 0.95 for a wind by itself.

The factor Ae is frequently referred to as the effective aspect ratio: A_{eff}. The total drag coefficient for a wing can therefore be written as:

$$C_D = C_{D_0} + \frac{C_L^2}{\pi A_{eff}}$$

Where: C_{D_0} is the lift independent sum of skin friction and pressure drag.

The factor Ae can be used to determine the lift curve slope of one wing from knowledge of the lift curve slope of another wing. To show this, assume that two wings have high but different aspect ratios. Also assume that both wings use the same airfoil. According to Prandtl's Lifting Line Theory if these wings are placed at the same effective angle of attack, $\alpha_a = \alpha - \alpha_0$, their lift coefficient, C_L will be the same. The angle $\alpha_a = \alpha - \alpha_0$ is called the absolute angle of attack and a_0 is the angle of attack for zero lift. Therefore:

$$a_{a_1} - \frac{C_L}{\pi(Ae)_1} = a_{a_2} - \frac{C_L}{\pi(Ae)_2}$$

$$\alpha_{a_1} = \alpha_{a_2} + \frac{C_L}{\pi}\left\{\frac{1}{(Ae)_1} - \frac{1}{(Ae)_2}\right\}$$

Because the lift curve slope, a, is related to the lift coefficient by:a

$$C_L = a a_a$$

It follows that:

$$\frac{C_L}{a_1} = \frac{C_L}{a_2} + \frac{C_L}{\pi}\left\{\frac{1}{(Ae)_1} - \frac{1}{(Ae)_2}\right\}$$

From the latter the lift curve slope of one wing follows from that for the other wing from:

$$a_1 = \frac{a_2}{1 + \frac{a_2}{\pi}\left\{\frac{1}{(Ae)_1} - \frac{1}{(Ae)_2}\right\}}$$

Again, this equation allows an estimate of the lift curve slope, a_1 of one wing with effective aspect ratio, $(Ae)_1$ if the corresponding, but different, properties of the other wing are known. This result should be used only for high aspect ratio wings. Generally, for A>5 the relation works well. The previously shown figure shows the effect of aspect ratio of wings with the same angle of attack for zero lift. Note that wings of varying aspect ratio tend to have

approximately the same angle of attack for zero lift. The lift curve slope is seen to decrease significantly with increasing aspect ratio. That effect agrees with Eqn (4.30).

For the same wing area and for the same airfoils, the wing zero lift drag is also essentially independent of aspect ratio. Application of induced drag equation to two wings which differ only in aspect ratio yields:

$$C_{D_i} = C_{D_2} + \frac{C_L^2}{\pi}\left\{\frac{1}{(Ae)_1} - \frac{1}{(Ae)_2}\right\}$$

The drag polars show that, although the drag coefficients at zero lift are essentially independent of aspect ratio marked reductions in the drag coefficient C_D, occur as the aspect ratio is increased. This is particularly true at high values of lift coefficient, C_L.

Equations 4.27 and 4.31 can be used to reduce the data to a wing with a common aspect ratio. It can therefore be concluding, that the characteristics of a wing of one aspect ratio may be predicted with considerable accuracy from similar data on a wing of different aspect ratio.

Eqn(4.30) can be used to determine the lift curve slope of a wing 1 when the characteristics of a wing 2 with the same airfoil section are known. If wing 2 has an infinite aspect ratio (i.e. is the equivalent of a two-dimensional airfoil selection), Eqn (4.30) can be reduced to:

$$a_1 = \frac{a_\infty}{1 + \dfrac{a_\infty}{\pi Ae}}$$

As it was previously mentioned the above equation produces good results only for wins with aspect ratios larger than 5 and with sweep angles below about 15 degrees. In our case the UAV will not utilize the sweep angle and so the above assumption can take place.

We can now use the above methodology to estimate the lift and the drag of a planform wing with arbitrary profile of airfoil used in it. Thus we can obtain. The two dimensional data the xflr5 simulations to get a first estimation of the plane characteristics. The first option is to take the slope of the Cl vs AoA curve of the airfoil, interpolate them integrate the polynomial equation and use the zero lift angle of attack value as a condition to calculate the integration constant, or we can either begin from the zero lift angle of attack and since we know the slope of the curve we can apply a shooting method (Taylor series with one term for example), to find the value of the lift at the next point. From the next point we again know the slope of the curve and by 'shooting' again we obtain the Cl of the new angle of attack and so on until we reach the angle of attack that we desire. In our case we used the second method with only one term in the Taylor series also known as Euler's method for solving first order differential equations with increment of one degree. It is also important to mention that if we chose to calculate the Cl in more than 15 points the first method has a tremendous

disadvantage because high order polynomials tend to oscillate between the interpolation values and thus either some Spline method should be used or break the whole domain in smaller spaces and apply the polynomial interpolation in sections.

2.3.2. High Lift Devices

We can say that an airfoil is a device that can generate enough lift force with relatively small generation of drag otherwise it can be called a bluff body. The airfoil pool that we are interested in is the high efficiency ones which means that the ratio of the Cl to Cd ratio is relatively higher from other airfoils and this means that they can generate the same amount of lift while producing less drag. A family of this kind of airfoils and the most common and widely use onces are the NACA 4-digit and NACA-5digit. Although that NACA airfoils tend to have a very consistent behavior in different Reynolds numbers and maintain a high efficiency we will not use them as a main wing airfoil but we will only use a symmetrical one as control surface in the empennage of the glider. Most of the airfoil coordinates that we collected can be found online via the site http://airfoiltools.com/ . The diagrams for the airfoil's behavior are extracted by using the XFLR tool. The following table summarizes the airfoil name the application that they were designed for, the projects that they were used at and some geometrical parameters such as maximum airfoil thickness, foil perimeter and the cross area of them. These specs will later on be used on the weight estimation method and also as criteria for airfoil rejection. The pool consists of 31 airfoils with the NACA0012 not included because it won't be used as a lift device but as a control surface

Table 2-3: Airfoil list, its application and the project that they selected from

Airfoil	Application	Paper
Phoenix	RC by Brett von Perlick	Analysis of airfoil for solar powered flying wing UAV
HS 3.0/9.0B	Solaris_Project	
S5020	Selig group Low Raynolds high lift airfoil	
S5010	Selig group Low Raynolds high lift airfoil	
EH 2.0/10	By John Yosh for Eh tailless RC aircraft	
HQ 3.0/8.0	Quabeck RC sailplane	
S905	Selig group Low Raynolds high lift airfoil	Airfoil Optimization for a Solar Powered Aircraft
SG6040	Wind turbine high lift airfoil	Airfoil selection
FX-63137	Wortmann FX 63-137 human power aircraft airfoil	
Aquila 9.3%	Sailplane application	Solar_powered_uav
Medium S9000 (9%)	Low Reynolds number airfoil used on the Blackhawk R/C sailplane	
S9037 (9%)	Low Reynolds number airfoil used on the Opus R/C sailplane	
WE3.55.	Solaris Project	
E387	Low Reynolds nunmber airfoil	AirfoilSelectionforaSolarUAVWingDesign
NACA 63412	Naca 5-digit high Cl/Cd group airfoil	
LA2573A	Modified versions used in business conceptual design	
SD7032	Selig/Donovan low Raynolds High lift airfoil	saleem2018 & sunsailor_israel
HN 1036	Widely used in gliders	XFLR5_Mode_Measurements
BC 2101	No coordinates found	Design and Performance of Low Reynolds Number Airfoils for solar-powered flight
BC 2125	No coordinates found	
E374	Eppler E374 low Reynolds number airfoil	Design considerations and modeling of a small and low altitude solar powered UAV
OA209	ONERA/Aerospatiale OA209 rotorcraft airfoil (Constructed from patent and smooth	Extensive wind tunnel tests measurements
SG6042	Selig / Giguere SG6042 wind turbine airfoil (high L/D)	Aerodynamic design of a MALE UAV
NLF0215	NASA/Langley/Somers NLF(1)-0215F natural laminar flow airfoil	
SA7038	Selig / Ashok Gopalarathnam SA7038	
NLF1015	NASA/Langley/Somers-Maughmer NLF(1)-1015 natural laminar flow airfoil	
EPPLER 423	Eppler E423 high lift airfoil	erodynamic design analysis of a UAV for superficial research of volcanic environmer
LKH 2411		2m_4kg
NACA 2412	Naca 4-digit high Cl/Cd group airfoil	
Selig 1223	Selig S1223 high lift low Reynolds number airfoil	Hartney.Su11
PSU 94-097	Maughmer PSU 94-097 winglet airfoil	Winglet design of a male...
Naca0012	Minimum drag and symmetrical foil for control surface wings (ailerons,rudervators)	

The coordinates of all the above airfoils were found and inserted inside the XFLR5 environment in order for the 2D simulation stages to take place.

2.3.3. Weight Estimation

In aviation literature there are some widely used methods that estimate the weight of the aerial vehicle weather it's a glider, a passenger plane or a small uav. Those methods are based on statistical data for the wing architecture the fuselage and the whole motor and propeller assembly. It's a fair method for the developer to obtain a realistic estimated weight with a safety factor coefficient reapplied in the calculations. Our weight estimation process although was not based on the literature statistical methods but we gathered all the necessary components that we need for this project we found the technical data of each compound and obtained the dimensions and the weight of each part. All the parts were then designed using the SOLIDWORKS CAD environment and defined as custom material with the desired density in order for the mass of the part to match the one of the real life object. The most difficult part of the uav assembly to define its mass is the composite ones because the properties of the final object will vary and are a function of the resin and the hardener that will be used during the vacuum forming. From previous experience with composite materials in formula

student wing manufacturing process, we can estimate the amount of the carbon fiber mass that will be used as well as the carbon to resign ratio and the overall volume of the polyurethane foam that will be used inside the wings.

For the estimation of the total mass we considered taking the worst case scenario. The heaviest part of the wing and fuselage part is the resign and the carbon fiber cloth. The foams that will be used have density around 30kg/m3 and thus we can tell that their contribution to the whole glider mass is not of vital importance. That said the weight of a wing with rectangular top view can be acquired as:

$$m_{total} = m_{carbon} + m_{poluourethane}$$

Or

$$m_{total} = A_{carbon} * \frac{Carbon_{mass}}{Area} + A_{foil} * b * \rho_{foam}$$

Where A_{foil} is the area of the chosen airfoil, b is the span of the wing and ρ_{foam} is the density of the foam. As was discussed previously the carbon mass is the greater one because it includes the mass of the resin with a 0.4 carbon to resign ratio. Thus to acquire the worst case scenario we did calculate the perimeter of all the airfoils and then we calculated the mass of the wing that uses the corresponding foil as profile. The results of the structural mass prediction are shown in the table below:

Table 2-4: Structural weight estimation

Structural		Component	Area (m2) or Volume (m3)	Weight/area (g/m2) or Density (g/m3)	Number	Overall	
			Main_Wing				
perimeter(m)	0.620008806	Skins	7.440105672	267	1	1986.508214	g
cross area(m2)	0.00748581	Foam	0.04491486	3000	1	134.74458	g
span(m)	6	Winglets				0	g
chord(m)	0.3	Tube_skin	0.08792	267	4	93.89856	g
tube_diam(m)	0.02	Tube_core	0.000219911	3000	4	2.638937829	g
			Fuselage				
		Body					g
		Cover				400	g
		Globe					g
		Tube					g
			Empennage				
Vertical			**Naca0012**				
perimeter(m)	0.60634232	Skins	0.60634232	267	1	161.8933994	g
cross area(m2)	0.007269926					0	g
span(m)	1	Foam	0.007269926	3000	1	21.80977773	g
chord(m)	0.3					0	g
Horisontal			**Naca0012**				
perimeter(m)	0.60634232	Skins	0.181902696	267	1	48.56801982	g
cross area(m2)	0.007269926					0	g
span(m)	0.3	Foam	0.002180978	3000	1	6.542933319	g
chord(m)	0.3					0	g
						0	g
Tube	Carbon						g
length(m)	1.5		0.20724	267	1	55.33308	g
OD(m)	0.022						
			Propeller				
Diameter = 600mm					1	100	
		STRUCTURAL WEIGHT				3011.9375	g

Besides the mass of the structural components, we also need to take into consideration the mass of the electrical parts that will be used in this project and even add a payload mass that may be added in the future. Because of the amount of the batteries that we need to use in order for the glider to endure a whole night flight the total weight of the electrical components pay a very serious role in the overall process. We did thought neglect the contribution of wires, tie wraps spacers etc.

Table 2-5: Electronics weight estimation

Electrical				
Component	Number	Weight/Part(g)	Overall	
Servo	4	71	284	g
Pixhawk_FC	1	90	90	g
Li-Ion	72	48	3456	g
Charging PCB	1	100	100	g
Solar Cell sotern	88	7	616	g
ESC	1	53	53	g
Motor-Reducer	1	300	300	g
Pitot_Tube	1	67	67	g
Receiver	1	1.8	1.8	g
Video_Transmiter	1	9.61	9.61	g
Antenaz	1		0	g
Camera			0	g
Misc(wires,spacers,etc.)			0	g
OVERALL			**4977.41**	**g**
TOTAL	**8989.347503**			

The total mass of the glider is somewhere around 9 kilograms with the condition that the resign that will be added to the carbon wings will be such that the ratio of 0.4 will be preserved. The weight estimation process itself allows for the designer to know the target lift that needs to be produced by the wings and by extension the lift coefficient of the uav since we do know the area of the solar panels that need to be placed in order for the desired voltage and current to be generated. So we do know the amplitude of the weight of the airplane but it is not enough for the whole design process. Later on in the stability analysis we will see that the distribution of the mass along the longitudinal and the transverse axis will also have a major impact in the stability and the response of the glider while flying or maneuvering. For now, we only need the amount of the weight in order to calculate the desired lift and drag coefficients.

Chapter3: 2D Analysis

As was previously discussed the LLT is a method that can allow us to save time by running 2D simulations and then, since our wing has an Aspect ratio of 20, map the existing results to a planform wing that was created by extruding the profile of the airfoil. The above simulation took place in XFLR5 environment and there is the capability of batch analysis which means that the user gives as input the desired range of angles of attack and Reynolds number and the simulations take place one after another.

3.1. 2D simulations
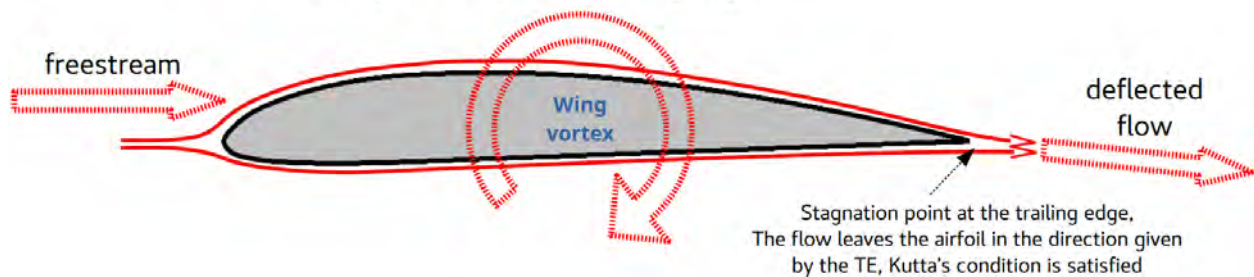
Figure 3-1: Kutta's condition

The 2D XFLR5 simulation environment solves the Euler's equations which arise from the Navier-Stokes equation with the assumption of inviscid and irrational flow around the 2D airfoil. The above assumptions can give some good results only in cases where the Reynolds number is high enough and the viscous term of the drag is negligible. In other words, the farther we are from the creeping flow the more precise the results that we will acquire. Those two assumptions come along with the Kutta condition in the trailing edge of the airfoil. The Kutta condition indicates that in an inviscid flow the speed of the fluid in the upper and the lower side of the airfoil match at the trailing edge and the wake remains calm and undisturbed.
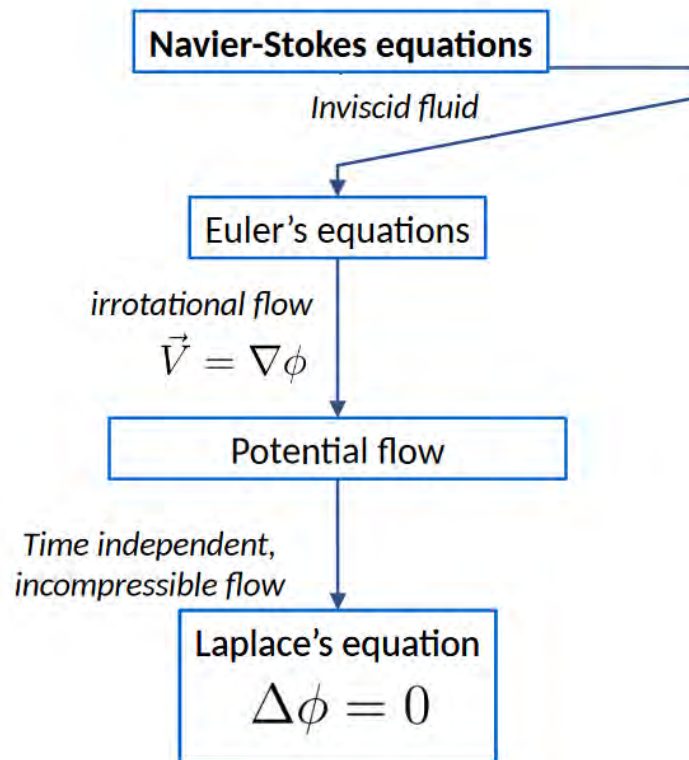
Figure 3-2: XFLR5 2d simulation Laplace Equation

The examination of the steady flight of the uav in the altitude of 2000 meters has as a result the atmospheric pressure to drop around 78.000 Pa and the density of the air to decrease around 10 percent which means that at that altitude is equal to 1. Along with the density the viscosity of the air has also decreased and reached 17.84E-06 Pa*s. It will be later on used on the 3D simulation with the VLM method. The Reynolds number is calculated at that speed and altitude and is equal to Re=250.000 and the corresponding Mach number is Ma=0.036 which is far away from the 0.3 area where the flow is considered compressible. That said we used the batch analysis method and run calculations for each airfoil from -5 up to 15 degrees Angle of Attack in order to capture the zero lift angle of attack for the 3D wing estimation process. All the airfoil results had the form that we did expect with some having better efficiency over others.
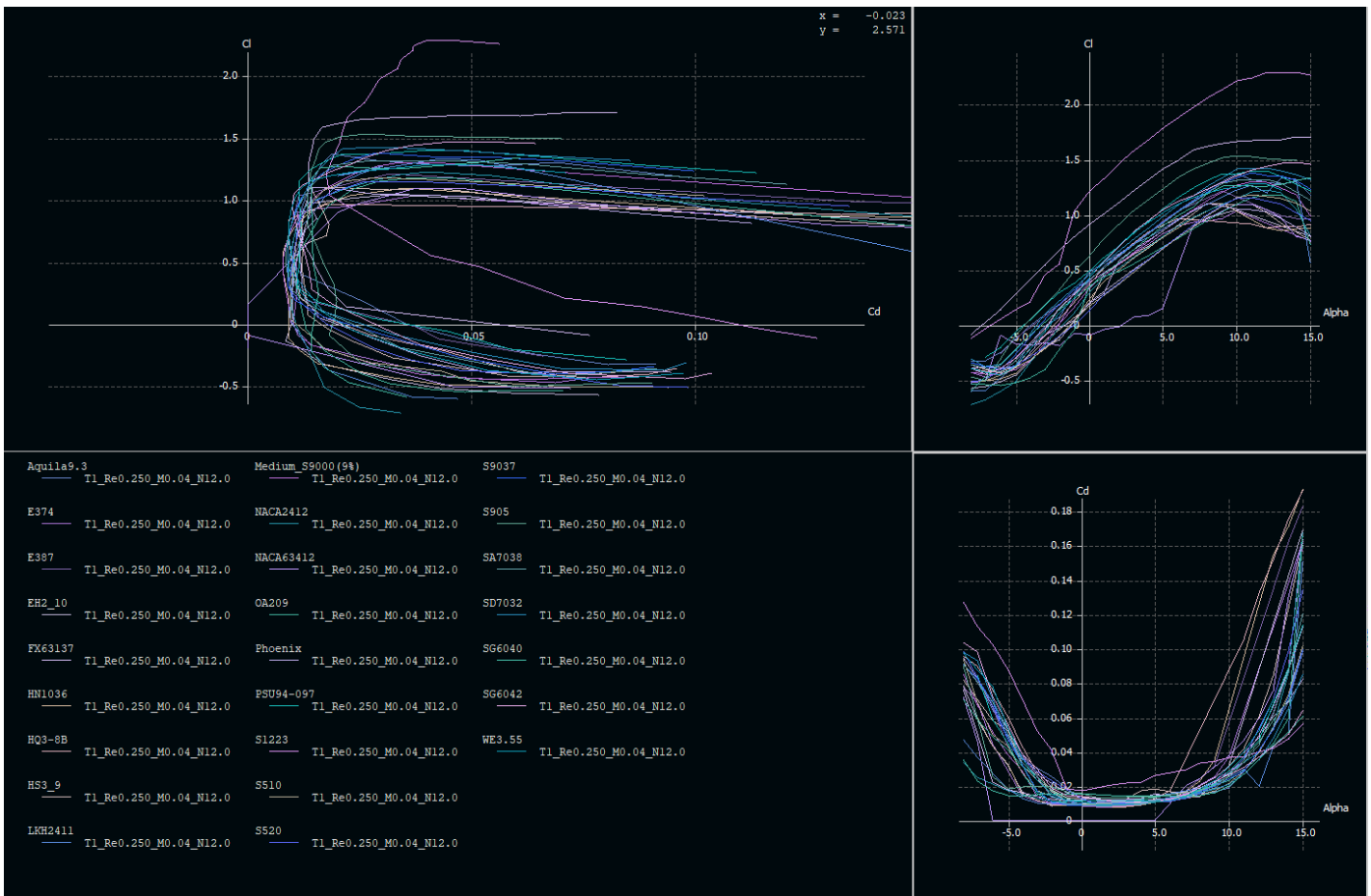
Figure 3-3: Airfoils @ Re=250.000 & AoA from -5 to 15 Simulations

The top left diagram is the polar of the Cl with respect to Cd. We can see that the Selig 1223 has a very efficient behavior as both the Cl vs Cd polar and the Cl vs AoA diagrams indicate. But it is too early to rule among others because the flow around it is inviscid and because of its shape it's difficult to be constructed and the great gradients make a favorable environment for the boundary layer to evolve and when the flow becomes turbulent the detachment of it will occur making the whole uav occasionally unstable. Furthermore, there is no induced drag generated and an airfoil that has the desired behavior might not be able to operate at that Angle of attack because of the downstream that the two counter rotating wingtip vortices create. All the results were imported in an EXCEL spreadsheet and with the

use of the previous methodology that was developed and by using Taylor Series with only one term the 3D Cl and Cd data were calculated for all the above operation points.

3.2.   Selection Criteria and 2D Airfoil Comparison

Once the initial size of the whole airplane was defined and the preliminary dimensions of the wing we had to choose among a wide variety of airfoils and wing types. We came across with 30 different airfoils each of one is considered either high performance or high lift device in low Reynolds number flights. At first we did utilize the XFLR5 environment for the majority of the cases, because of the ease and the short simulation time of it. In avionics projects phenomena such us wing flutter and wind fluctuations, boundary layer detachment and reattachment, the effects of the roughness of the wing surface, compressibility effects, propeller wake etc. that can alter the nature of the flight and that transient simulation have to take place in order for a better understanding and design of the glider. However, our thesis does not extend to that level and a steady state simulation is used in all cases for comparison. So our first goal is to reject the majority of the airfoils and pick those that have the better performance. So we did set some strict criteria in order to start restricting our choices. Thus the criteria that were set focus on the aerodynamic performance of the wing and in miscellaneous factors that can affect our glider. Most popular and of main importance are the following:

- High $\frac{Cl}{Cd}$ ratio

- Lift distribution within the desired flight range (constant function of velocity is preferable)

- Maximum thickness for structural installation with batteries encapsulation in the wing

- High $\frac{Cl^{\frac{3}{2}}}{Cd}$ ratio. This is a term that was extracted for maximum endurance- minimum power consumption

- Adequate lift in moderate angles of attack for high solar irradiation absorbance

- Low Cm amplitude for minimum torsional stress concentration at the fuselage-wing connection

- Maximum thickness of the airfoil must not be less than 30mm so that there is enough space for the batteries and the shell around them to be placed.

- Minimized drag power consumption

Most of the above criteria are widely used in avionics projects and even in cases where the aerodynamic design of an object influences the losses due to drag forces. Some of the above criteria are set to match our preferences like the lift distribution is not a mandatory and can have small to zero impact on other cases. But the most direct and physically understood criterion by the majority of the popularity is the power drag losses. It shows how well the construction behaves when moving inside a fluid and after all it is the parameter that we need to optimize for max endurance flight.

The first section of the 2D airfoil comparison is the easy part because we can take advantage of the two criteria the one of the airfoil thickness and the second one that takes into consideration the Value of Cl to Cd ratio and remove all the airfoil that tend to stand off the rest. We also observed that at some airfoils the stall occurs at relatively small angles of attack and they were immediately removed from the selection pool. After this stage we were left with 16 airfoils that are summed up in the following table.

Table 3-1: 16 best airfoils

S905	SG6040	FX-63137	AQUILA 9.3%	PSU94-097
S9037 9%	WE3.55.	SD7032	SG6042	
SA7038	NLF1015	EPPLER423	SELIG1223	

For the above airfoils we then used the Prantlds lifting line theory that was developed in the previous chapter and for a monoplane of a wing with AR=20 and C=0.3 we extracted the Lift and Drag forces.

3.2.1. 2D to 3D Estimation

The simulation in the XFLR5 were using nondimensionalization hence the airfoil had length equal to 1. This means that the match of the 3D data will happen by using the Drag calculation formula and the area of the wing with the fixed aspect ratio will give us the final pressure drag and lift. Now we do have the resulting Cl of the two dimensional airfoil from the XFLR simulations with increment one degree. We did not keep all the values from -5 up to 15 degrees but we reduced that range so that the data of each airfoil include the zero lift angle of attack.

Table 3-2 :Phoenix XFLR Data

xflr5 v6.10.03   Possible

Calculated polar for: Phoenix

1 1 Reynolds number fixed   Mach number fixed

xtrf = 1.000 (top)   1.000 (bottom)
Mach = 0.036   Re = 0.250 e 6   Ncrit = 12.000

alpha	CL	CD	CDp	Cm	Top Xtr	Bot Xtr	Cpmin	Chinge	XCp	dCl/dα	3D Alpha	3D CL	Lift (kg)	Cdi	Cd_3D_estimation	CL^(3/2)/CD	CL/CD
-2	-0.02	0.0217	0.0157	-0.027	0.688	0.106	-0.879	0	-1.09	0.067	0.067327777						
-1.703264095										0.067	0.067327777						
-1	0.0474	0.0163	0.0106	-0.02	0.605	0.265	-0.503	0	0.666	0.154	0.153922004	0.04734921	0.62616912	4.19785E-05	0.016331978	0.630856067	2.89917161
0	0.2017	0.013	0.0051	-0.017	0.568	0.041	-0.593	0	0.337	0.087	0.086879702	0.20127121	2.6617091	0.000758516	0.013738516	6.5725316	14.6501426
1	0.2887	0.0124	0.0038	-0.011	0.52	0.05	-0.69	0	0.287	0.302	0.300753477	0.28815091	3.81064883	0.001554681	0.013944681	11.09229546	20.6638589
2	0.5909	0.0118	0.0058	-0.051	0.492	1	-0.937	0	0.335	0.089	0.089272978	0.58890439	7.78796013	0.006493679	0.018293679	24.70393547	32.1916878
3	0.6803	0.0123	0.0063	-0.047	0.47	1	-1.052	0	0.317	0.09	0.089372694	0.67817737	8.96854972	0.008611678	0.020921678	26.69429298	32.415056
4	0.7698	0.013	0.0071	-0.043	0.443	1	-1.249	0	0.303	0.08	0.079499284	0.76755006	10.150458	0.011030994	0.024010994	28.00592605	31.9666099
5	0.8494	0.0156	0.01	-0.038	0.398	1	-1.583	0	0.291	0.1	0.100140144	0.84704935	11.2017955	0.013434411	0.029054411	26.83187322	29.1538984
6	0.9497	0.014	0.0084	-0.034	0.373	1	-2.28	0	0.282	0.085	0.085383812	0.94718949	12.5260978	0.016798672	0.030808672	29.92142892	30.7442493
7	1.0352	0.0144	0.009	-0.029	0.299	1	-3.64	0	0.272	0.066	0.065531581	1.03257331	13.6552551	0.01996379	0.03433379	30.56043935	30.0745506
8	1.1008	0.0147	0.0088	-0.021	0.201	1	-5.016	0	0.261	-0.025	-0.024509557	1.09810489	14.5218769	0.022578176	0.037248176	30.8930456	29.4807694
9	1.0763	0.0221	0.0152	5E-04	0.019	1	-4.935	0	0.241	-0.03	-0.030014331	1.07359533	14.1977505	0.02158154	0.04369154	25.46030295	24.5721558
10	1.0463	0.0278	0.0213	0.02	0.016	1	-5.053	0	0.221	-0.004	-0.003900242	1.043581	13.8008263	0.020391705	0.048151705	22.13999804	21.6727737
11	1.0424	0.0363	0.0305	0.031	0.017	1	-5.179	0	0.21	-0.016	-0.015803974	1.03968076	13.7492476	0.020239567	0.056539567	18.74983845	18.3885518
12	1.0266	0.0501	0.0454	0.037	0.021	1	-4.998	0	0.202	-0.066	-0.065668562	1.02387678	13.5402481	0.019628929	0.069738929	14.85580777	14.6815674
13	0.961	0.0672	0.0632	0.033	0.023	1	-4.732	0	0.202	-0.074	-0.074488202	0.95820822	12.6718148	0.017191786	0.084341786	11.12108209	11.3610141
14	0.8866	0.0877	0.0842	0.022	0.023	1	-4.381	0	0.21	-0.072	-0.072383291	0.88372002	11.6867464	0.014622802	0.102312802	8.119738853	8.63743347
15	0.8143	0.1125	0.1094	0.005	0.023	1	-3.817	0	0.227			0.81133673	10.7295143	0.01232547	0.12481547	5.855086138	6.50028982

The previous table is an example of what a spreadsheet of an airfoil looks like after the data have been imported inside excel. We can tell that the data include the zero Cl angle of attack since the Cl starts from negative values and then they rise above zero. The zero lift angle of attack was calculating with linear interpolation of the values prior and after it. The second stage is to calculate the rate of change of the Cl with respect to the angle of attack. To do so we used the discretized derivative and the slopes were calculated as

$$\frac{dCl}{da} = \frac{Cl_{i+1} - Cl_i}{a_{i+1} - a_i}$$

For i ranging from 0 to the n-1 value of Cl. Then the relation that was extracted from the Lifting line theory in chapter 2 94.30) can help us to calculate the Cl curve slope of the corresponding rectangular wing.

$$a_1 = \frac{a_\infty}{1 + \frac{a_\infty}{\pi A e}}$$

Where a_1 is the slope of the wing and a_∞ is the slope of the airfoil. Here the e term is the Oswald efficiency factor and it is equal to 1 for the elliptic lift distribution. The K column in the excel worksheet uses the above formula to calculate the slope and then with Eulers method we calculated the L column which has the 3D wing Cl slope. We can see that in the Phoenix and then in the column M finally the Cl of the wing is found. The above methodology allows us also to calculate the pressure difference drag and the induced drag but since the flow is inviscid the friction drag term is neglected. The estimation of the 3D wing Cd is used to compare the airfoils based on the efficiency criteria. As we know the Reynolds number of our wing is pretty low and the friction drag cannot be neglected but at this point since the airfoils have not great gradients on them and the flow can be considered laminar we only use the calculated values for comparison and further reduce the amount of the airfoils in our pool. After the final airfoil is chosen we will proceed in Ansys CFD simulations using turbulence models for better results.

3.3.   Airfoil Comparison and Rejection Stages

Having reduce the amount of airfoil profiles that we currently have in our hands we need not to just estimate the lift of a wing with the LLT but we also need to compare our data with other methods and then validate the results with a real life testing. The next stage in the rejection process is to take advantage of the imbedded Vortice Lattice Method that the XFLR5 extension has implemented and use them to further compare and then reject the remaining airfoils. To do so we designed the 13 above wings and we did run simulations with the VLM method.

A solution for three-dimensional wings of any general form can be obtained by using a vortex lattice model. For incompressible, inviscid flow, the wing is modelled as a set of lifting panels. Each panel will contain a single horse-shoe vortex. A bound vortex is located at the panel 1/4 chord position with two trailing vortex lines shed from each end.
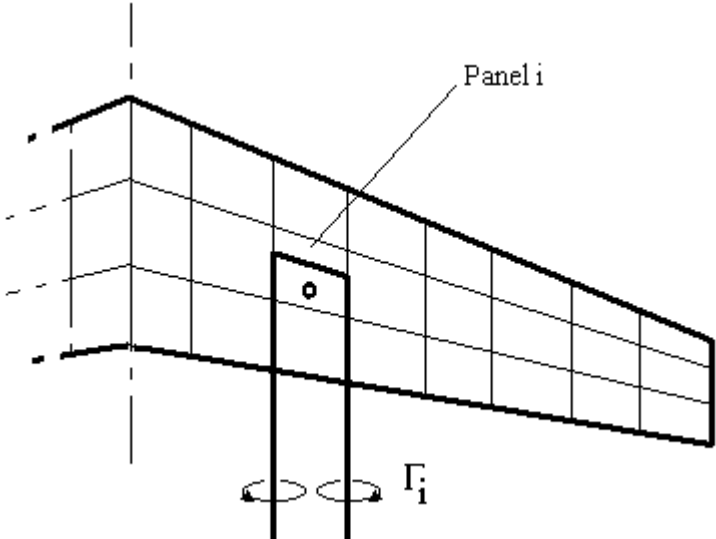

Figure 3-4: VLM Panels And Circulation Γi

Both span-wise and chord-wise variation in lift can be modelled as a set of step changes from one panel to the next.

The required strength of the bound vortex on each panel will need to be calculated by applying a surface flow boundary condition. The equation used is the usual condition of zero flow normal to the surface. For each panel the condition is applied at the 3/4 chord position along the center line of the panel. The normal velocity is made up of a freestream component and an induced flow component. This induced component is a function of strengths of all vortex panels on the wing. Thus for each panel an equation can be set up which is a linear combination of the effects of the strengths of all panels. A matrix of influence coefficients is created which is multiplied by the vortex strengths and equal to a right hand side vector of freestream effects.

$$V_n = 0 = V_\infty \sin(\theta) + w_i$$

$$w_i = \sum_{j=1}^{N} A_{i,j} \Gamma_j$$

Thus

$$\sum_{j=1}^{N} A_{i,j}\Gamma_j = -V_\infty \sin(\theta)$$

The influence coefficient $A_{i,j}$ will represent the induced flow on panel **i** due to the vortex on panel **j**. If all panels are assumed to be approximately planar then this influence coefficient can be calculated as a relatively simple application of the Biot-Savart law along the three component vortex lines.
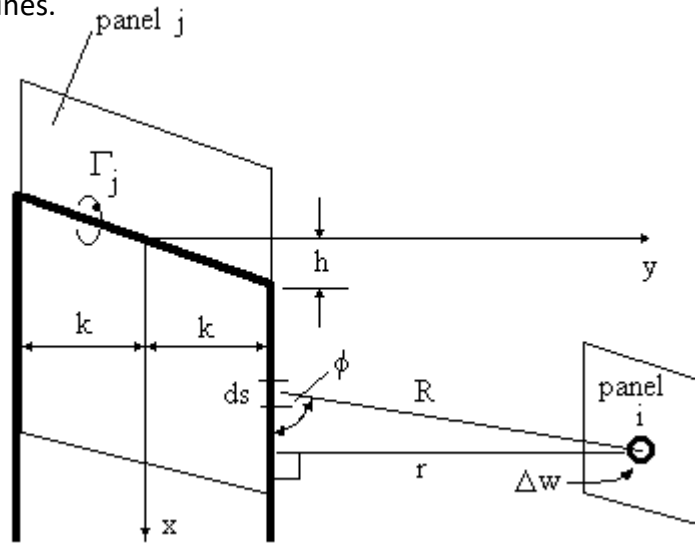

Figure 3-5: Panel

The result of this integration leads to the following formulae for influence coefficients in general.

Thus

$$\Delta w = \frac{1}{4\pi}\frac{\sin(\varphi)}{r^2}\Gamma_j.ds$$

$$w_{i,j} = \int \frac{1}{4\pi}\frac{\sin(\varphi)}{r^2}.ds.\Gamma_j = A_{i,j}.\Gamma_j$$

where the integration is done in three parts, the two trailing lines and the bound vortex, giving

$$A_{i,j} = \frac{1}{4\pi}\left(A_{\text{bound vortex}} + A_{\text{left trailing}} + A_{\text{right trailing}}\right)$$

where

$$A_{\text{bound vortex}} = \frac{1}{(x+h)(y-k)-(x-h)(y+k)}\left(\frac{2h(x+h)+2k(y+k)}{R_1} - \frac{2h(x-h)+2k(y-k)}{R_2}\right)$$

$$A_{\text{left trailing}} = -\frac{1}{(y+k)}\left(1+\frac{x+h}{R_1}\right)$$

$$A_{\text{right trailing}} = \frac{1}{(y-k)}\left(1+\frac{x-h}{R_2}\right)$$

where

$$R_1 = \sqrt{(x+h)^2 + (y+k)^2}$$

$$R_2 = \sqrt{(x-h)^2 + (y-k)^2}$$

The right-hand side terms for the boundary condition equations will depend upon the freestream velocity, the angle of attack for the wing and the slope of the panels due to camber effects.

$$\sin(\theta) = \sin\left(\alpha - \beta_i\right) \approx \alpha - \beta_i \approx \alpha - \left(\frac{dz}{dx}\right)_i$$
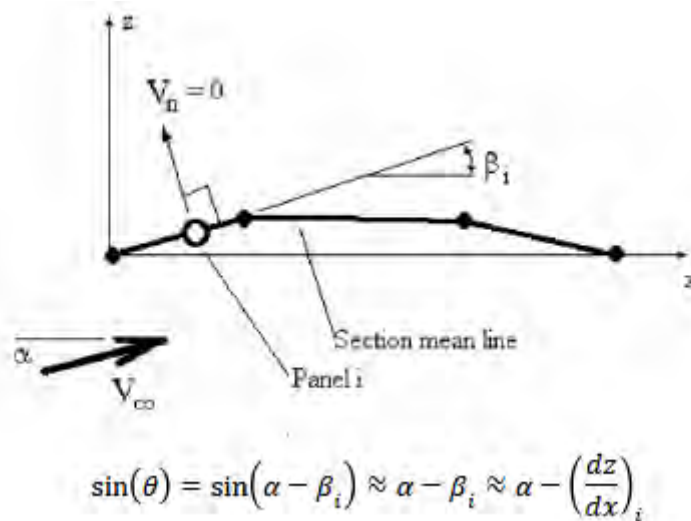
Assuming all the angles are small. A solution for the strength of the vortex lines on each panel is found by solving the matrix of equations for the strength of each vortex panel, Γ_j.

The lift coefficient for the wing at a given angle of attack will be obtained by integrating the panel lift distribution. The lift on a particular panel can be found using the Kutta Law.

$$L_i = \rho V_\infty \Gamma_j 2k$$

Therefore, lift of wing is the sum of all panel lift components,

$$L = \sum_{i=1}^{N} L_i$$

The downwash velocity induced at on a panel can be calculated once the strength of the wing loading is known. The variation between local flow angles for the panel and the freestream velocity can be found. A consequence of this downwash flow is that the direction of action of each panel's lift vector is rotated relative to the freestream direction. The local lift vectors are rotated backward and hence give rise to a lift induced drag. By integrating the component of panel lift coefficient that acts parallel to the freestream across the span then the induced drag coefficient can be found.

$$D_i = \rho V_\infty \Gamma_i \sin(\alpha_i)$$

Which is the induced drag from panel i.

Therefore, the lift induced drag of the wing is

$$D_{induced} = \sum_{i=1}^{N} D_i$$

The induced flow angle ($\alpha_i \approx \frac{w_i}{V_\infty}$) represents a rotation of the lift vector backward and must be calculated from the velocities induced on the bound vortex of the panel by other panels and the freestream.

Pitching moment about the wing root leading edge can be calculated by summing the panel lift multiplied by a moment arm which extends in the x-direction from the leading edge of the wing to the center of the bound vortex for the panel.

At this point a standard wing design procedure would first calculate the Cl and Cd for a specified Reynolds number or we could better say for a fixed velocity for the angle range that the wing might fly and repeat the above process until we have data for a desired velocity range. Then we would calculate based on our weight estimation the stall speed or the stall angle that the airplane needs to fly in order to maintain a constant altitude and then compare the above wings and chose the best one. This process is very time consuming and with the help of XFLR we can choose the option of constant lift generation, which in our case want to be equal to our weight and then acquire all the stalling velocities of each angle. This option saves us from multiple simulations and can give us a very clear view of each airfoil characteristics. With span equal to b=6 meters and chord C=0.3 m we have the above data for each wing and import them in EXCEL.

Table 3-3: PSU Stall Speeds For Each AoA

xflr5 v6.13

Wing name :   Plane Name
Wing polar name : T2-VLM2-10.0kg-x0.0m-Inviscid

alpha	CL	CDi	CDv	CD	Cm	QInf	XCP	u (m/s)	Lift (kg)	Drag (kg)	Drag_Energy (Watt)	Min Power (Watt)
-4	0.016864	0.000019	0.02792	0.027939	-0.11498	80.3968	2.0563	80.35474	10	16.56724	13046.314	30.199
-3	0.11233	0.000252	0.01597	0.016222	-0.13861	31.1506	0.3717	31.13464	10	1.444138	440.635	AoA (degrees)
-2	0.207768	0.000803	0.01121	0.012013	-0.16228	22.9047	0.2349	22.89299	10	0.578193	129.718	6
-1	0.303115	0.001671	0.01121	0.012881	-0.18595	18.9631	0.1843	18.95344	10	0.424954	78.933	
0	0.398309	0.002855	0.0117	0.014555	-0.2096	16.5426	0.1579	16.53414	10	0.36542	59.211	
1	0.493288	0.004352	0.01161	0.015962	-0.23321	14.8649	0.1417	14.85736	10	0.323584	47.114	
2	0.587991	0.006159	0.01195	0.018109	-0.25673	13.6153	0.1307	13.60838	10	0.307981	41.073	
3	0.682356	0.008272	0.01197	0.020242	-0.28014	12.6389	0.1229	12.63241	10	0.296649	36.724	
4	0.776322	0.010686	0.01181	0.022496	-0.30342	11.8493	0.1169	11.84325	10	0.289777	33.633	
5	0.86983	0.013393	0.01146	0.024853	-0.32653	11.1943	0.1123	11.18857	10	0.285722	31.329	
6	0.962819	0.016389	0.01151	0.027899	-0.34944	10.64	0.1086	10.63456	10	0.289764	30.199	
7	1.055232	0.019663	0.01392	0.033583	-0.37214	10.1634	0.1056	10.15822	10	0.318252	31.682	
8	1.147011	0.023209	0.01729	0.040499	-0.39458	9.7483	0.1031	9.743343	10	0.353083	33.714	
9	1.2381	0.027015	0.02124	0.048255	-0.41675	9.3829	0.101	9.37808	10	0.38975	35.820	
10	1.328442	0.031072	0.0292	0.060272	-0.43862	9.0582	0.0992	9.053583	10	0.453704	40.255	
11	1.417985	0.035368	0.03776	0.073128	-0.46016	8.7675	0.0976	8.763064	10	0.515718	44.289	
12	1.506675	0.039891	0.04698	0.086871	-0.48134	8.5056	0.0963	8.501234	10	0.576574	48.036	
13	1.594461	0.044629	0.068	0.112629	-0.50214	8.2681	0.0952	8.263896	10	0.706377	57.207	
14	1.681292	0.049568	0.0891	0.138668	-0.52253	8.0518	0.0942	8.047671	10	0.82477	65.047	
15	1.767122	0.054695	0.1136	0.168295	-0.54248	7.8538	0.0933	7.849799	10	0.952368	73.264	

The above sheet gives us an example for the stall speeds of the PSU foil for each angle of attack from -4 up to 15 degrees. We can see that the lift column only has the value of 10 kg which is the target lift that we need to generate for our plane in order to glide and not decent. Again the most direct criterion in the rejection stage of the power of the drag that is consumed during steady flight. We do use this criterion because it is the most direct and does not let any misunderstandings behind the wing behavior. If we did chose another criterion, then there is a simple thought that can lead to wrong airfoil selection. The drag force can be calculated as a function of the Drag Coefficient C_d times velocity squared. When stall occurs the drag coefficient has increased dramatically and the speed of the glider is relatively steady this means that in the C_d, V product the C_d term plays the determinant role. But in steady laminar flow flight in small angles of attack the drag coefficient increases linearly but the drag force increases mostly due to the velocity increase. So there is a compensation weather the designer should place the wing in a smaller angle of attack and design it to fly at higher speeds or if the angle of attack should be increased and the velocity of the vehicle should be decreased. The power consumption gives us the answer because we can compare for the different stall speeds the power consumption. We also need to take into consideration that due to disturbances in the flight the angle of attack will not remain constant but it may alter and fluctuate. So it is

important to compare the range of the drag power that will be consumed to get a better understanding of this phenomenon. We can see that the distribution of the PSU airfoil around the 6 degrees remains relatively constant. It is a desired behavior for our application and for application where efficiency is the determinant factor.

After the second stage that was described above we have the pool with the top 10 most efficient airfoils. The selection is not that obvious and for that reason we need to develop a point gaining system that will split them and will distinguish the best of them. An indicative value of the behavior of the remaining airfoils can be observed in the diagrams bellow. The selected airfoils are the 4 best of the pool based on the drag power consumption as was previously described.
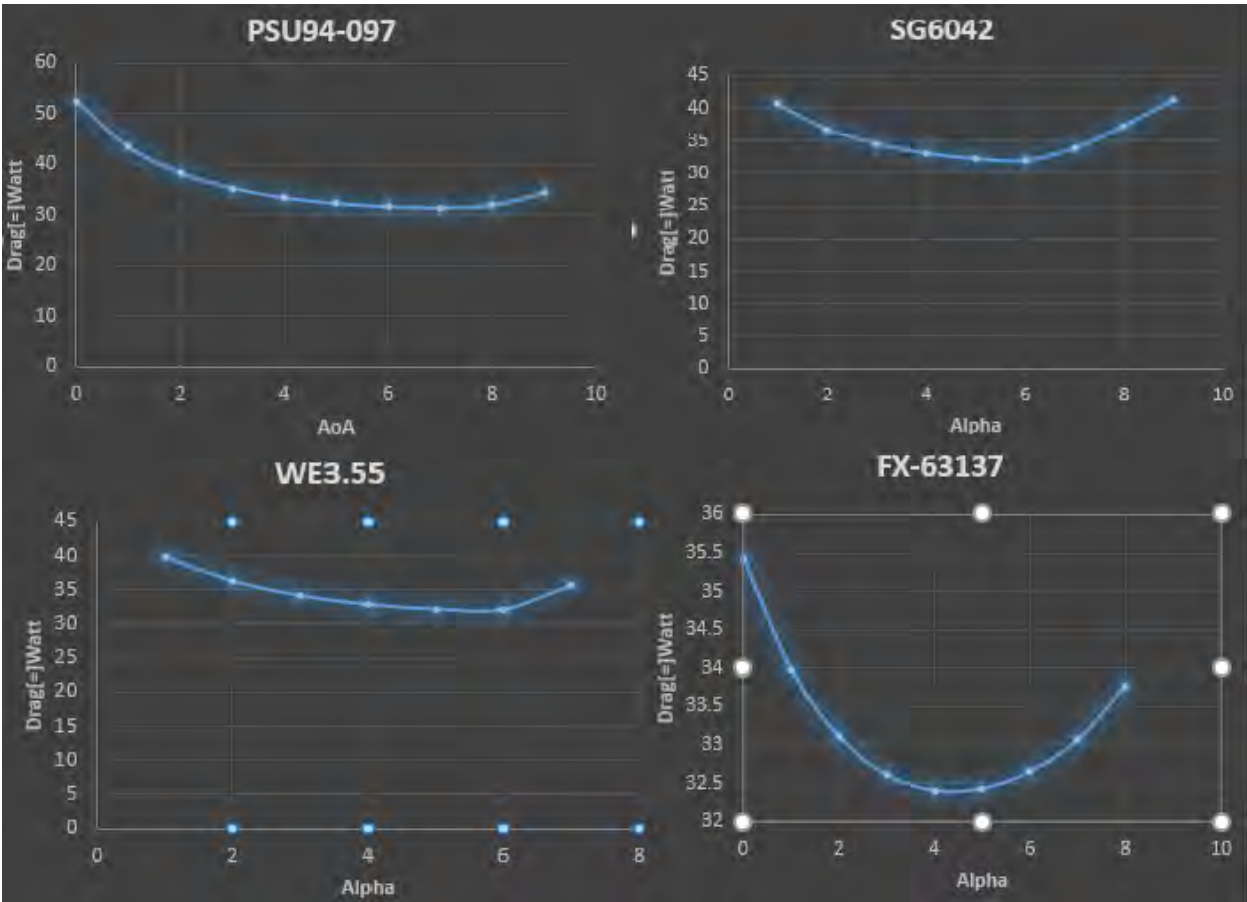
Figure 3-6: Top 4 airfoils

All of the airfoils have the same local minimum value of power consumption which is 30 watts. But we can also observe the behavior of them in greater and smaller angles of attack. For example, the Wortman airfoil has a pretty constant consumption while the FX increases rapidly on either side of the local minimum. This behavior is not positive and we do not want them to act like that unless we can guarantee that the designed operation point will not change during flight.

Table 3-4: Voting Method

ID	Parameter	Selection	Airfoil 1	Airfoil 2	Airfoil 3	Airfoil 4	Airfoil 5	Airfoil 6	Airfoil 7	Airfoil 8	Airfoil 9	Airfoil 10	Column1
1	Re for stall												
2	Re for best ROC												
3	Re for cruise												
4	Target Cl,max												
5	Cl for best ROC												
6	Cl for target cruise												
7	Name		PSU	SG6042	WE3.55	FX	S9037	S905	SD7032	SG6040	Aquilla	S1223_LLT	
8	Thickness ratio												
9	Lift for data bellow		10	10	10	10	10	10	10	10	10	10	
10	CD,min	(lowest is the best)	0.033213	0.031928	0.032433	0.040502	0.026552	0.041387	0.02919	0.033744	0.032146	0.049349	S9037
11	(CL/CD),max	(max is the best)	31.674284	31.764188	31.518114	29.080416	33.289959	28.654143	32.017335	29.829036	30.060536	25.0760502	S9037
12	CL^(3/2)/CD,max	(max is the best)	32.487348	31.988398	31.866466	31.560157	31.298139	31.204203	30.952434	29.926582	29.550073	27.8950968	PSU
13	Drag power, min	(lowest is the best)	31.4774	31.9687	32.091052	32.4025	32.6738	32.7721	33.039	34.1712	34.6066	36.6598	PSU
14	CD,min	(lowest is the best)	6	3	5	8	1	9	2	7	4	10	
15	(CL/CD),max	(lowest is the best)	4	3	5	8	1	9	2	7	6	10	
16	CL^(3/2)/CD,max	(lowest is the best)	1	2	3	4	5	6	7	8	9	10	
17	Drag power, min	(lowest is the best)	1	2	3	4	5	6	7	8	9	10	
18	Overall	(lowest is the best)	1	4*	2*	3*					S.K.	S.K.	

The voting method compares the colored cell parameters that are in the second column and the best of each airfoil is given the lowest number. This means that each airfoil gathers points based on its performance of each parameter and then the whole column is added. The airfoil that its points sum is the smallest one is the one that has the better overall performance. That way we are allowed to compare the airfoils based on the desired criterion. The star on the Overall row means that the placement has been altered because that airfoils might have gathered smaller amount of points but the criteria are not the desired. For example, we did discus that the Cl to Cd ratio might mislead the reader and therefore despite the fact that the SG6042 airfoil has a smaller sum of points the PSU is the best airfoil since the Endurance criterion and the minimum power consumption are more important and direct that the Cl to Cd ratio and therefore the places have been swapped. Another aspect that was not taken into consideration during the voting process is the distribution that was referred previously. We can observe that the SG6042 might have better Cl to Cd ratio but the lowest consumption is not extended for a great range like the PSU.

3.4.   Experimental Setup

The simulation stage is really important in the design of the UAV but since the XFLR5 is a tool that has not been used in the industry widely and the projects that are designed are not based to it we cannot claim that the results have the desired precision and besides doing a further simulation with some turbulence model we designed an experimental setup that will allow us to validate the results. There was a greater need to compare the 2D simulation results with a real life testing rather than the 3D wing results. One way of validating is by wind tunnel testing in the three dimensional wing. Since our university's wind tunnel cross section area is not that big we have to scale down the model in order to obtain the Lift of our wing. Furthermore, drag force calculation demands the existence of a scale measuring method in the x axis which our University wind tunnel is not designed for this. Our proposition to calculate only the pressure drag that is generated by an airfoil is to tight fight a wing that has span equal to the width of the wind tunnel and then measure the static pressure on the upper and the lower area of the wing using silicon tubes and create a manometer. That said, the experimental set up consists of :

- A 3D printed wing with holes along its chord wise direction. The holes will be created along its chord for measuring the local static pressure in the upper and lower side.
- Silicon tubes that will be used as manometers to measure the static pressure in each hole.
- 3D printed adapters that will mount the wing in the side panels of the wind tunnel and will allow us to change the angle of attack of the wing in the desired range (0-10 degrees).

The two dimensional flow assumption is accurate enough since there will be no gap between the wind tunnel glass and the wing and so the circulation distribution along the span of the wing will be the same in each transverse plane. The two major problems that will make our results deviate from the two dimensional flow is first and foremost the 3d printed wing surface roughness because it can translate the transition point of the boundary layer further forward and cause the stall to occur at lower angles of attack and at even higher Reynolds number as well as the location of the pressure measuring holes because if they are placed

close to the wind tunnel wall the development of the boundary layer can alter the acting pressure over the airfoil. Another aspect to be taken into consideration is the size of the holes, their number and the alignment. Placing them one really close to another can cause recirculation of the airflow above them causes the flow that each hole meets be different. In order to avoid such problems, we will try to avoid placing holes one rear another in the 3d printed model. Furthermore, the frontal area of objects that will be tested inside a wind tunnel should not exceed the 5% of the wind tunnel's cross section area because otherwise the boundary layer that is created from its walls will affect the flow around the object. In our case the maximum thickness of our airfoil is 29.5mm and therefore the speed on the upper and lower area will be increased since the Venturi effect takes place. The speed increase can be calculated from the continuity equation as:

$$\dot{m} = \rho v A = constant$$

$$\rho v_1 A_1 = \rho v_2 A_2$$

$$u_2 = u_1 \frac{A_1}{A_2} = u_1 \frac{H}{H-T}$$

Where the H and T are the wind tunnel height and the airfoil maximum thickness respectively. As a result, the velocity u_2 will be:

$$u_2 = u_1 \frac{700}{700-29.5} = 1.044 u_1$$

The design of the wing took place in Solidworks design environment. The wing is made in parts since the building height of the 3d printer is 165 mm the wing will be made in 5 parts. The middle part will be the one to carry the pressure line holes and will be connected to the others with press to fit assembly. Each hole is designed to a plane tangent to the wing surface as shown below:
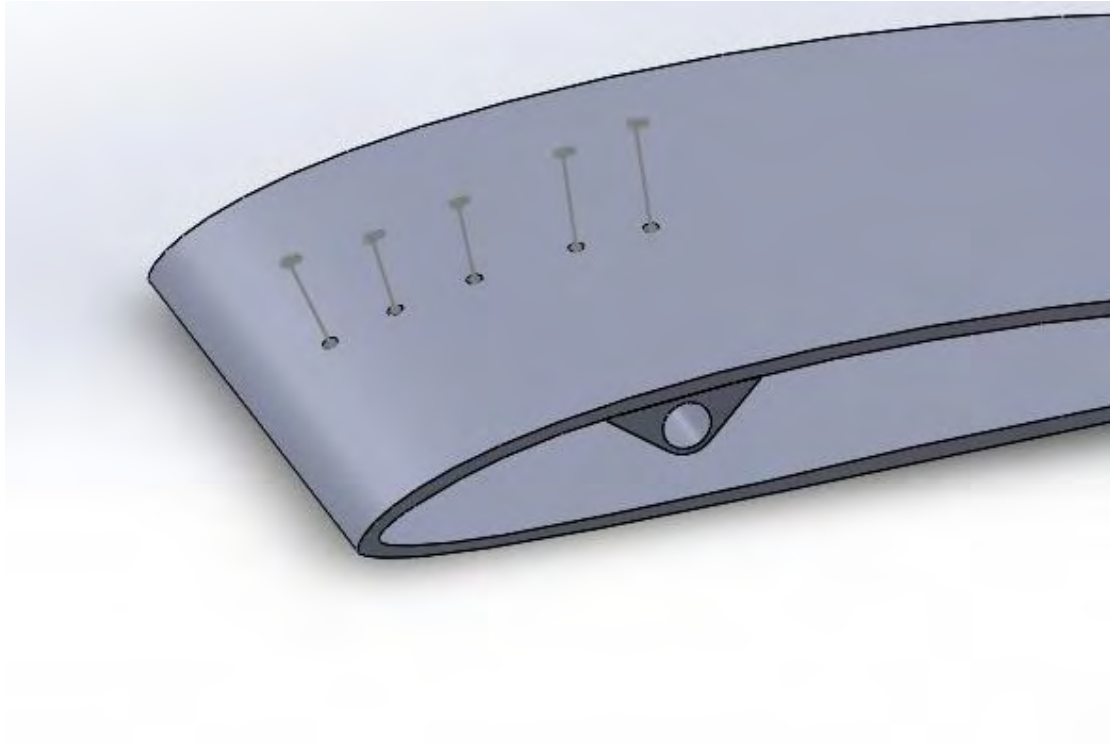
Figure 3-7: Cross Section of the 3D printer Airfoil

As was shown from the Mathew McCarty's thesis the hole diameter in pressure measurement can range from 1.5mm up to 5.4 mm without observing any strange behavior in the pressure coefficient. The following diagram gives a visual representation of the values fluctuation which in our case can be considered negligible.
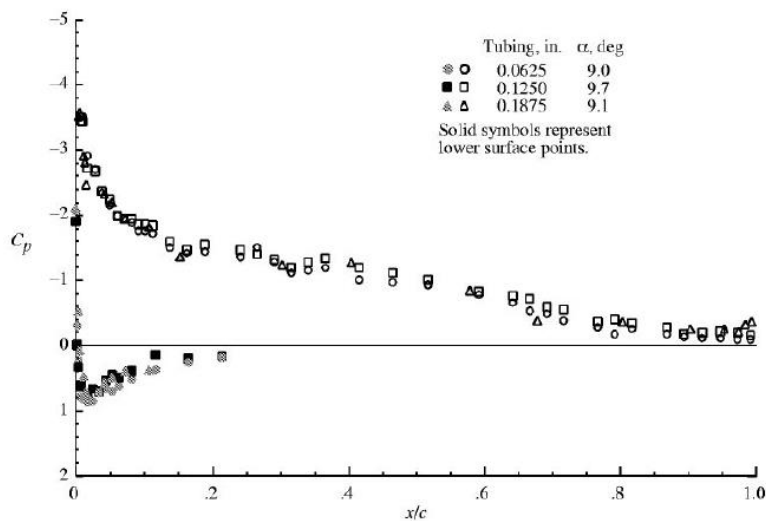
Figure 3-8: Hole diameter comparison

Once knowing the pressure distribution of an object we can extract the pressure coefficient (C_p) and by integrating it around it we can obtain the total force that acts on it. As the figure 2 indicates we need to find the projection of the Lift vector to the perpendicular direction and then integrate the local Cp to acquire the generated lift.
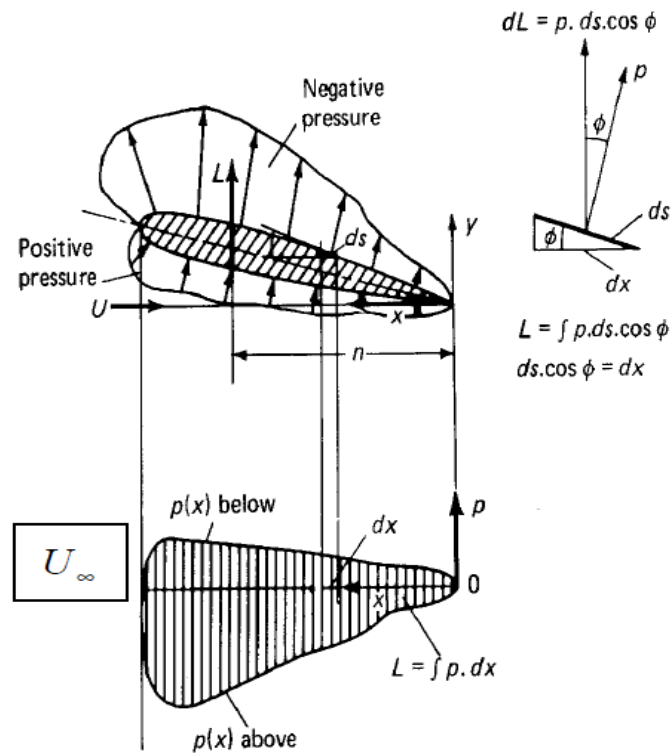
Thus we can write:

$$C_L = \frac{\int_C (p_i - p_\infty) \sin(\theta)\, ds}{\frac{1}{2}\rho U_\infty^2 c}$$

Where θ is the angle of surface normal to free-stream flow. The 15 pressure values that will be acquired will let us interpolate them and get expressions of the pressure distribution. It is important to be noted that we have to split the points and create 2 or even three functions because high order polynomials tend to oscillate between the interpolation

points. Knowing the airfoil coordinate set will allow us to calculate the slope of the curve at the same points and such the sin(θ) term will be known.

Given of a function f(x) we can write:

$$\int_a^b f(x)dx \approx \sum_{i=1}^{15} f_i w_i \ ,$$

Where f_i is the function to be integrated, f_i is the value of the function at the desired points and w_i is the weight at each of these points whose value depends on the method that will be used.
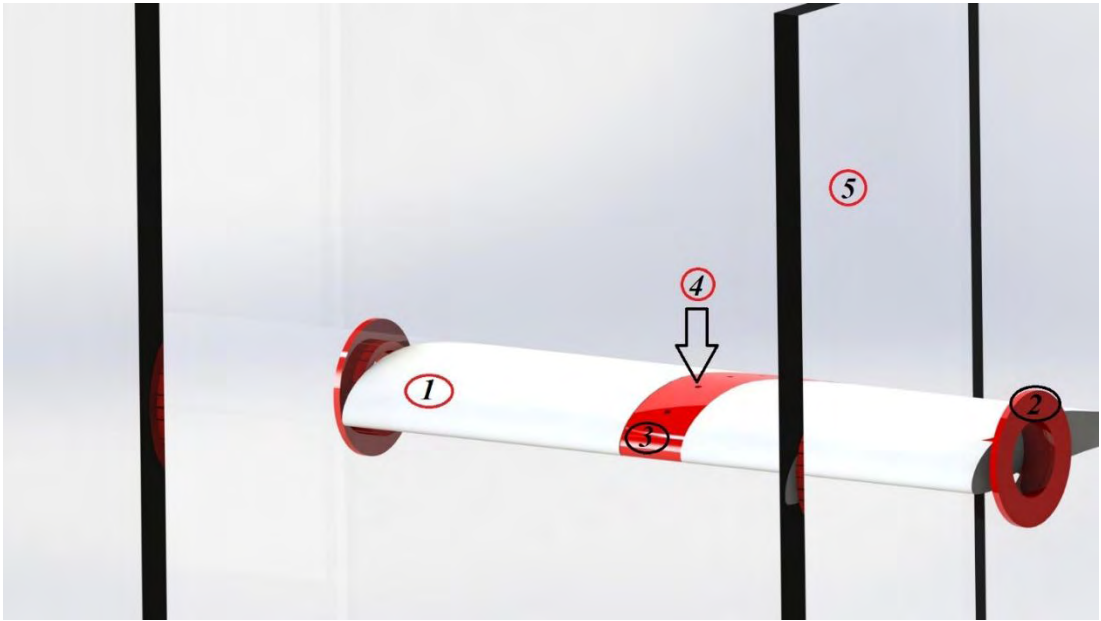
Figure 3-9: Experimental Setup Render

Table 3-5: Parts for the experiment

PART NUMBER	
1	3D printed airfoil
2	3D printed adapter/goniometer
3	3D printed Airfoil
4	Pressure tube lines
5	Wind tunnel side glass walls

The goniometer is 3D printed and the indications are engraved on it while still in the printing process. In case the precision of the angle measuring is not enough the 3D printed airfoil can have a specifically designed slot to enter a Gyroscope. The adapter is bored so that the pressure tubes can come outside the airfoil and end up to the manometer.
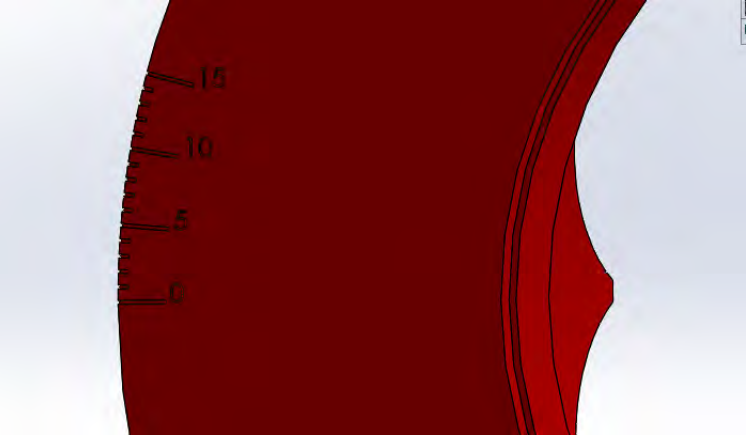
Figure 3-10: 3D printed adapter/goniometer

The experimental setup was not performed and was let as future work.
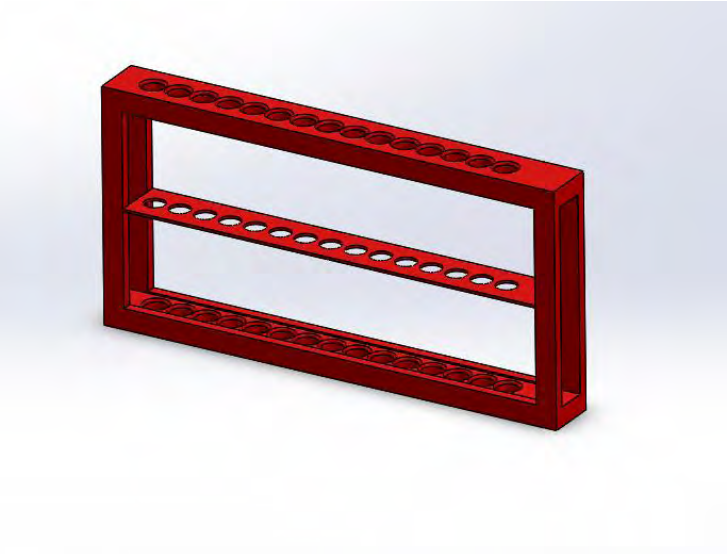
Figure 3-11: Manometer tube holder

Chapter4: Wing

With the end of the 2D simulation process and having validated the results with the experimental setup that was proposed in the previous section our next step is to define the parameters of the three dimensional wing and study their effect on the aerodynamic behavior of our plane.
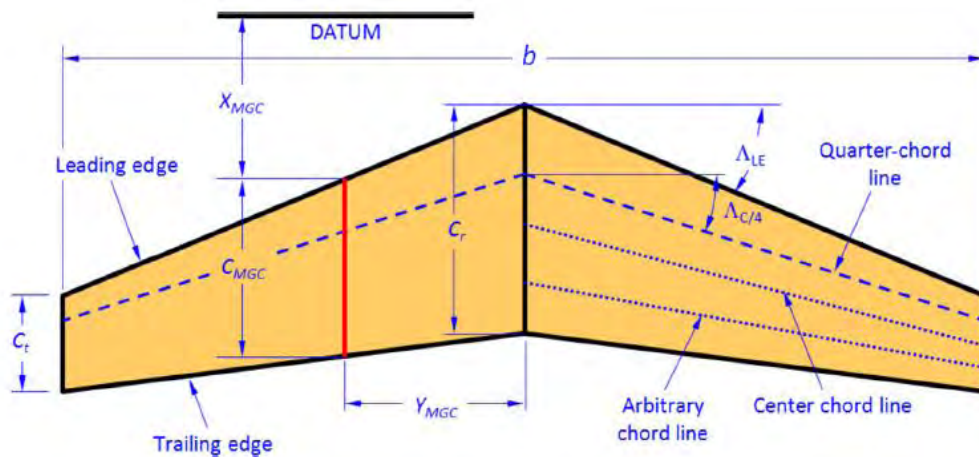
Figure 4-1: Fundamental definitions of a trapezoidal wing planform

The above figure represents the fundamental definitions of an arbitrary 3d wing and all the parameters that can alter its top view shape. Other parameters that cannot be present by the top view is the dihedral angle and the twist of the wing in the spanwise direction. The first one plays an important role in the lateral stability around the roll axis as it will be shown later on the stability section, while the second one is used to decrease the angle of incidence in the wingtip and by that way decreasing the amplitude of the counter wingtip vortices that tend to be generated from the pressure difference above and under the wing.

Figure 1 shows the general definitions for the geometry of the trapezoidal planform and indicates important details of such sections. A leading edge is the part of a lifting surface that faces the direction of intended movement. The trailing edge is opposite to that side. The root is the inboard side of the planform and, as can be seen in the figure, is where the two trapezoids join. This would typically be the centerline of the aircraft or the plane of symmetry. Although the term root sometimes refers to where the wing intersects the fuselage, that

definition is not used in this text because the geometry of the fuselage may be changing and thus defining a wing chord there would lead to some undesirable issues. The tip is the side opposite of the root e it is the outboard side. The distance between the left and right tip is called the span, denoted by the variable b. The transverse dimension is called chord. Thus we talk about a root-chord or tip-chords the length of the corresponding sides, denoted by the variables Cr and Ct, respectively. We also call the ratio of the tip-chord to the root-chord the taper ratio, denoted by l. Another important ratio is the aspect ratio, AR, which indicates the slenderness of the wing. Both are expressed mathematically below. The quarter-chord line is drawn from a point one fourth of the distance from the leading edge of the root-chord to a point one-fourth of the distance from the leading edge of the tip chord. It is important because two-dimensional aerodynamic data frequently uses the quarter-chord point as a reference when presenting pitching moment data. Scientific literature, for instance the USAF DATCOM, regularly uses the quarter-chords a reference point for its graphs and computational techniques. Additionally, this is often the location of the main spar in lifting surfaces and it is very convenient to the structural analysts to not have to perform moment transformation during the design of the structure. The center chord line is obtained in a similar fashion to the quarter-chord line and is sometimes used as a reference in scientific literature, although not as frequently. Other important parameters are the sweep angles of the leading edge and quarter-chord line, denoted by LLE and LC/4, respectively. The mean geometric chord (MGC) of the planform is often (and erroneously) referred to as the mean aerodynamic chord (MAC), which is the chord at the location on the planform at which the center of pressure is presumed to act. The problem is that this location is dependent on three-dimensional influences, such as that of the airfoils, twist, sweep and other factors, not to mention angle-of-attack, in particular when flow separation begins. Authors who refer to the MGC as the atypically acknowledge the shortcoming, present the geometric formulation presented here to calculate it, before continuing to call it the MAC. In this text, we will break from this convention and simply call it by its appropriate title e the MGC. The importance of them is that it can be considered a reference location on a wing, to which the location of the center of gravity is referenced and even for a quick preliminary estimation of wing bending moments inside it. Therefore, it is important to also estimate what its span wise station, yMGC, is.

Wing Span:

$$b$$

Wing Area:

$$S = b(\frac{C_r + C_t}{2})$$

Aspect ratio- General:

$$AR = \frac{b^2}{S}$$

Taper ratio- constant-chord:

$$AR = \frac{b}{C_{avg}}$$

Taper ratio:

$$\lambda = \frac{C_t}{C_r}$$

Average chord:

$$C_{avg} = \frac{C_r + C_t}{2} = \frac{C_r}{2}(1 + \lambda)$$

Mean geometric chord (MGC):

$$C_{MGC} = (\frac{2}{3})C_r(\frac{1 + \lambda + \lambda^2}{1 + \lambda})$$
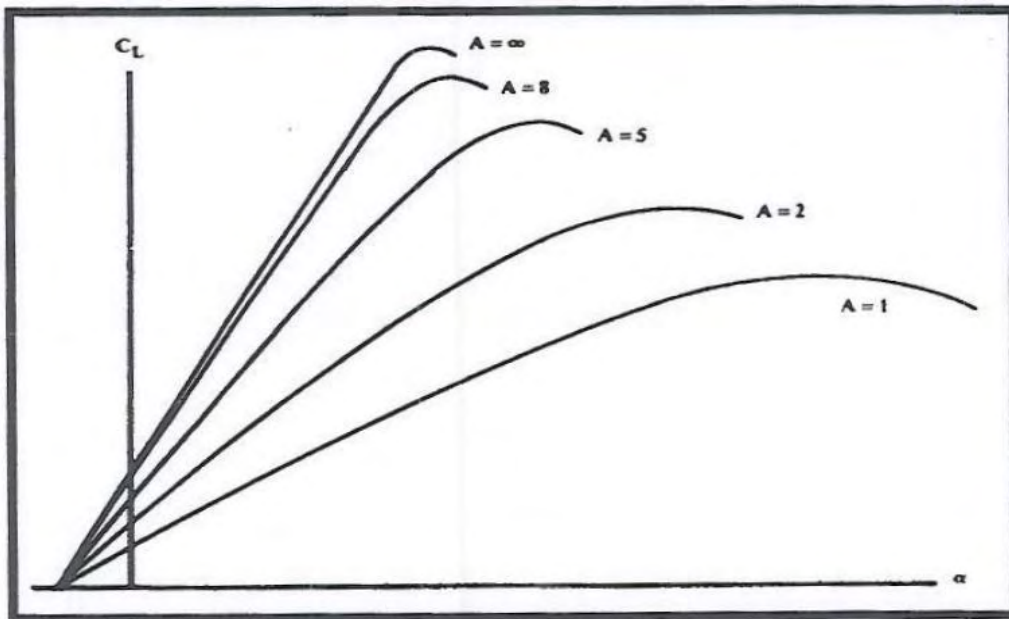
Mean aerodynamic chord(MAC):

$$C_{MAC} \approx C_{MGC}$$

Y-Location of MGC$_{LE}$:

$$y_{MGC} = (\frac{b}{6})(\frac{1 + 2\lambda}{1 + \lambda})$$

X-Location of MGC$_{LE}$:

$$x_{MGC} = y_{MGC} tan\Lambda_{LE}$$

Our goal is to define the above parameters so that the final wing setup meets our criteria. To begin with we have to understand what are the differences of a 3d wing aerodynamic behavior compared to its foil. The simplest wing that can be generated from an airfoil is the planform because it has steady chord along its span, has no twist or taper ratio and overall is an extrusion of the foil to the 3rd dimension. Comparing the lift coefficient of a 2d foil with its planform wing for a constant chord C for different angles of attack we can see that increasing the span of the wing and such the AR of it the C$_l$ curve tends to increase and try to match the one of the airfoil as shown in the figure below.

The above phenomenon occurs due to the induced vortices and thus decreasing the efficiency of the wing. These two counter rotating wingtip vortices create a downwash behind the wing and thus they alter the trajectory of the incoming wind by an angle, induced angle of attack.
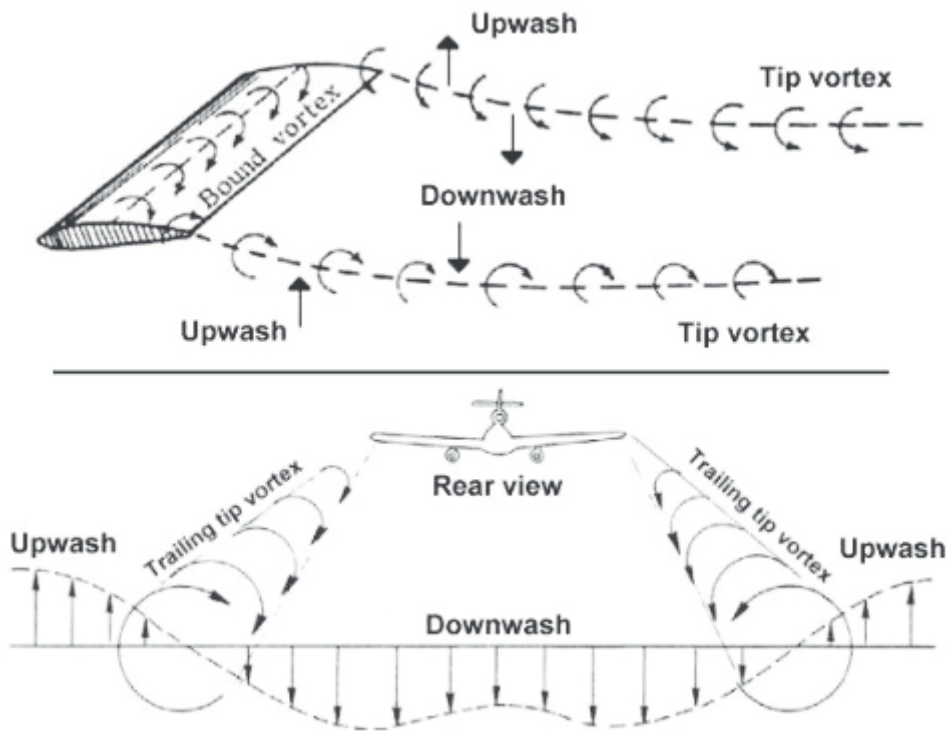
Figure 4-3: Counter rotating wingtip vortices

For high aspect ratios the region of the wing that is affected by the two vortices is a small fraction of the whole wing and as a result the overall lift coefficient tends to match the 2-dimensional foil. Plotting the Cl vs AoA of a wing we can expect the behavior that is described in the graph below and note some notable points on the diagram such as the zero lift coefficient angle of attack, the slope of the linear section and the peak value as well as the post stall region and the second peak that most authors and diagrams neglect. The diagram below shows the general behavior of the Cl coefficient and a bit after stall occurs.
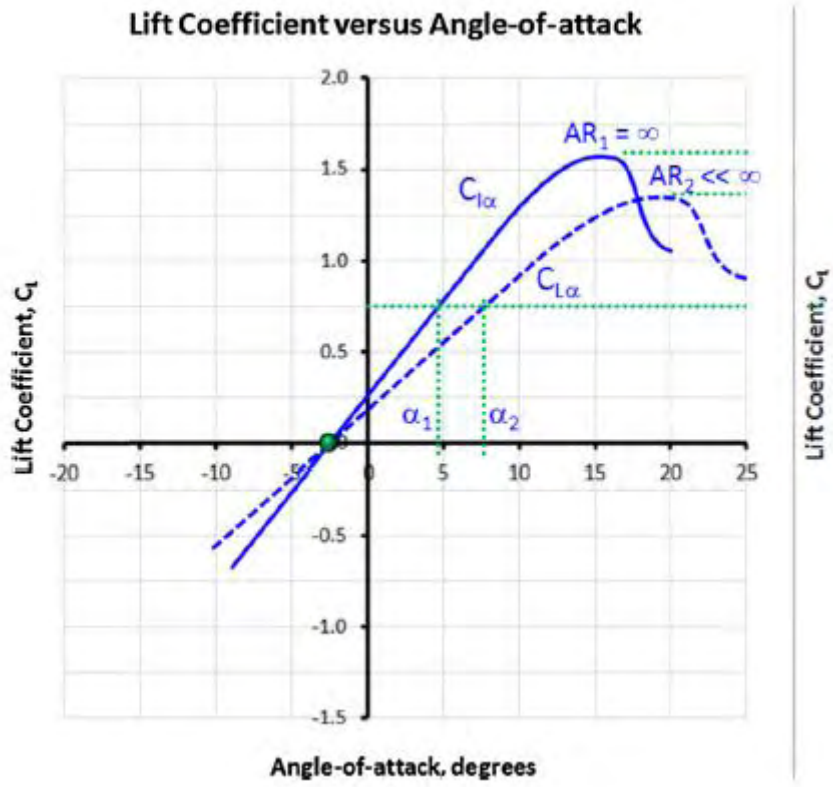
Figure 4-4: Typical diagram of Cl vs AoA

The continuous curve shows the behavior of a wing with an infinite span which concurs with the 2D wing curve. We can see there is an angle of attack where the lift coefficient is equal to zero and it is below zero. This indicates that the chosen airfoil has a cambered profile cause otherwise, in case of being a symmetrical airfoil, the zero-lift angle would have been in the zero degrees angle of attack. It is important to notate this specific point cause later on it will help use define the wing characteristics of an arbitrary wing based on the two-dimensional data of the airfoil. Furthermore, it is worth mentioning that the above diagram ranges between -20 to 25 degrees. This range is not enough to show the second peak of the curve after the stall region as was previously mentioned. One of the reasons that someone wants to use a high lift device at its post stall region is only as an airbrake that needs to utilize high drag coefficient and still maintain a high lift coefficient while breaking. Otherwise the same lift coefficient can be achieved in lower angles of attack without sacrificing that much of energy in winning the drag force.

4.1.　　Ansys CFD Simulation

Computational Fluid Dynamics (CFD) is the use of applied mathematics, physics, numerical analysis and data structures to solve and analyze problems that involve fluid flows and visualize how a fluid (*air is the fluid for Aerodynamics*) flows as well as how it affects objects as the flow pass. Computational fluid dynamics is based on the Navier-Stokes equations. These equations describe how the velocity, pressure, temperature, and density of a moving fluid are related. Computers are used to perform the calculations required to simulate the interaction of liquids and gases with surfaces defined by boundary conditions. With high-speed supercomputers, better solutions can be achieved. Initial experimental validation of such software is performed using a wind tunnel with the final validation coming in full-scale testing. The current generation of CFD packages generally is capable of producing accurate solutions of simple flows. The codes are, however, designed to be able to handle very complex geometries and complex industrial problems. When used with care by a knowledgeable user CFD codes are an enormously valuable design tool.

In this chapter there will be a brief representation of the workflow process that someone can follow in order to achieve simulating the field around an object that comes in contact with a fluid. In our external aerodynamics simulation, we need to calculate the pressure and the velocity field of a 3D wing and by extension the aerodynamic characteristics of the wing and of the whole uav respectively. The results that will be acquired from the simulation process have to be validated with real life testing like wind tunnel testing or some prototype data acquisition. The CFD process has to be accompanied with real life constants that need to be calculated and altered base on each case study. In our case we will use the default values of the Ansys fluent platform in all the physical constants except the very simple ones such us density and we did chose to use the k-epsilon turbulence model because of previous experience. Our previous experience is based on the participation in our University's FSAE team in the aerodynamics field. Simulations of a FormulaSAE car were more complex and included more simplified model of the car compared to the real one. After the manufacture of the car took place the validation process calculated a magnitude of error of around 13% with some parts of the car not included in the simulation process. The flow of the intake and the exhaust was not included and some parts of the transmission were not inserted in the simulated model. So by comparing the two case studies we can assume that the real life

model will have less error than the FSAE car because of the simpler and less complex phenomena around our geometry.

Our workflow starts with the design process which occurred in the Solidworks CAD environment in order to get the 3 dimensional geometric description of the examining object which initially was the planform wing. Once having the geometry most simulation Suites have embedded tools in order to simplify and 'clean' some geometrical faults. This process is called Pre-processing. With the end of it the geometry is ready to be discretized into smaller elements. An example of pre-processing is the removal of tiny details or patch gaps that their overall contribution to the result is negligible and the removal of them will help the mesh generation. The second stage is the discretization of the subdomain which is called mesh generation. It consists of the surface mesh generation, the boundary layer elements generation in the case of external aerodynamics simulation and finally the volume mesh generation. Once having acquired the mesh of the geometry we then pass to the solution section. We define the boundary conditions in the control volume, as they will be discussed later, and then our whole problem is being deduced in solving a system of linear equations. Finally, all the simulation suites offer a user friendly way of monitoring and calculating the desired variables such us temperatures velocity and pressure contours, mass flow, etc. with a UI program called the post processing.

It has to be mentioned that the designer has to design having in mind that the produced geometry will have to generate a mesh based on it. It is usually a painful task to get mesh with good quality in difficult geometries. Most program suites do not have a good preprocessor and thus the geometry cleanup has to take place in the CAD software.

Figure 4-6: Simulation process

4.1.1.   Geometry Preparation

The main difference between designing for production and designing for simulation is the pre process of the simulation which is the meshing. During simulations and especially external aerodynamic simulation some defects of the geometry and some minor changes can alter slightly the result of the simulation but offer you less computational time and less meshing time. For example, deleting the bolt and the nut in an airplane that exceeds the surface of a 200 square meter, has not a major impact in the overall aerodynamic behavior of the model in the simulation and it can save you some computational time and even decrease the amount of effort you need to make in order to obtain the mesh of your geometry. The major aspects that someone who designs for external simulation has to take into consideration are:

- Overlapping faces
- Intersecting geometry
- Proximity regions
- Zero thickness geometry
- Very thin shells or features

A strong preprocessor like ANSA can avoid the designer bumping on those problematic areas but since most of the free and commonly used software has embedded or even no preprocessors the above have to be taken into consideration during the design process.

Overlapping faces: They are faces that for a reason coexist in the same region and during the meshing process the mesh will be generated on both of them and the result will be a mixed area of elements that do not match the quality criteria and as a result even if the meshing process succeeds the fluent solver will crash.

Intersecting geometry: Intersecting geometry is the area where two features or entities have common points and some region of the space is common for both of them. In example we can think a sphere inside a cube. Again, the mesh process will try to take place between them, and the result will not allow us to run the calculation during solving.

Proximity regions: These regions are some areas where the meshing that will be created between them has to be very fine and the element size has to be really small in order for the gap to be filled. These regions are regularly problematic because a sizing method has to be added to allow for further decrease in the size of the elements. The major difficulty is the boundary layer generation process because this will inflate the elements towards the adjacent proximity surface.

Zero thickness geometry: Zero thickness geometry are usually areas where two surfaces meet with the angle between them to be really small. This is the major problem of our geometry and it is in the trailing edge of the wings. The region where the upper and the lower surfaces meet they create an area where the mesh cannot be generated cause the skewness of the elements will be greater than 0,9 which is not an acceptable value for the fluent solver or the amount of the small elements that have to be generated in order for the area to be described is not reasonable and having lots of those areas will dramatically increase the number of your element. One way of overcoming that problem is to either cutoff a small portion of the trailing edge that can cause an imperceptible effect on the wing or to filet that edge. We chose the first option because if we want to fit more than 2 elements in the trailing edge the size of the elements had to be lower than 0.3mm which is lower than the defeaturing size and as a result the filet would have been replaced by a flat area. As shown in the picture below the thickness of the trailing edge was set at 1mm and the minimum element size of that

region se to 0.5mm. That way the mesh generation algorithm can mesh the rear side of the trailing edge with elements across its span without causing the number nor the quality of them to exceed the limitations.
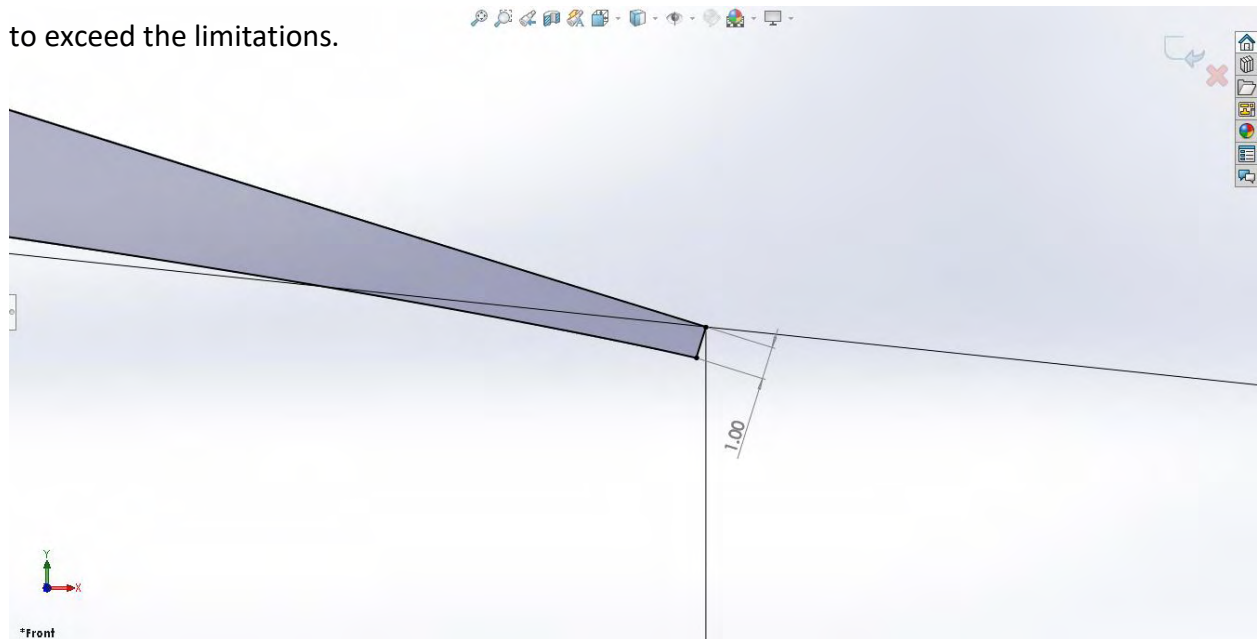
Figure 4-7:Trailing Edge cutoff

This technique is widely used in wing simulation area but it abrogates the Kutta condition in the end of the wing and thus creates a vortice aft of the wing and thus 'steals' some kinetic energy of the air that ideally could have been used to generate more lift.

After the clean-up and simplifications like the one shown above are done the next step is to define the control volume where the calculation will occur. In the case of external aerodynamics simulation, the control volume can be seen as a wide wind tunnel where the walls of the tunnel are really far from the geometry and thus, they do not affect our flow close to the object. Instead of the faces of the control volume being a static wall which as a boundary condition is translated to no slip condition and no penetration condition now these faces are considered as a symmetry and thus they simply do not affect physically the field inside the domain. That said we can understand that during the pre-Processing the Fluid Domain inside which the CFD simulation is going to take place must be defined carefully to ensure the reliability of the results. In most external aerodynamics the Fluid Domain has the shape of a rectangular box and represents a virtual wind tunnel in which the body of interest must be

placed and must be ensured that there is always enough space between the inlet, the geometry and the outlet so, that the boundary conditions could be met with the geometry of the uav included thus the dissipation of vortices downstream from the wing does not disturb the solution upstream and the pressure at the stagnation point evolves reasonably. The entrance to the wind tunnel is typically placed about 4-5 times the characteristic length ahead of the geometry and an inlet velocity is defined on it. Respectively the exit of the wind tunnel is placed about 8-10 times the characteristic length behind the geometry and is considered as a pressure outlet while the side walls of the domain are placed about 2-3 times the characteristic length further. Typically, the ratio of the vehicle cross section to the wind tunnel cross section is within a certain range. This ratio is called blockage ratio and has to be less than 6% or even less than 2% depending on the inlet velocity and the kind of results that the user wants to examine on each case. As a result, the effects of the Fluid Domain walls on the pressure distribution and thus, the drag coefficient are small. Otherwise, the flow field around the uav is disturbed by wall influences. The user must also consider taking advantage of symmetries in the geometry and run the simulation in the symmetrical section. After the calculation is complete the complete part can be regenerated by the symmetrical part of the geometry.

To reduce the total cell number, and therefore computing time, a symmetry plane was used down the center of all the geometries. Symmetric Computational domain may be used to reduce the computation effort without significant loss of accuracy and can save up to 50% or more in simulation turnaround time. Additionally, you can use the shortage memory to run more accurate simulations with more mesh cells clustered in areas of interest. However, it is not always given that a symmetric model will also have a symmetric flow field. For instance, the flow over a symmetric cylinder in a certain Reynolds number range exhibits vortex shedding that is clearly not a symmetric flow field. However, for external flow over airplanes and gliders the flow is symmetric enough to only run a simulation on symmetric half model. Symmetric simulations are also not applicable if the domain boundaries represent the walls of a real wind-tunnel. In this case the simulation should take into account the related wall effects. Simulations with complete vehicle domain is recommended when the uav is tested in cornering or if a correlation with experimental data has to be done.

Once the geometry is inserted into the Ansys design modeler we need to create the enclosure with the dimensions described above. Once we did that, we now need to remove the airplane geometry from the domain and we want to keep only the fluid volume to examine. This can be achieved with the Boolean operation in the tool tab of the Ansys design modeler. The remaining faces that in contact with the fluid will later on be assigned as walls and this is how the wing affects our velocity field. After the pressure distribution on those faces is calculated the forces that act on the plane will be calculated with numerical integration and projected on each direction giving us the total amount of drag and lift that the air above the plane is generating.

Besides the control volume domain, we can clearly understand even from our intuition that some areas around the under examination object play a more important role in the overall aerodynamic behavior. In the case of a car the flow behind the wheel or over the cockpit or even right above the wings are more crucial than that in the free stream right before the geometry where the air stays undisturbed. Since those areas are of a greater importance, we can increase the number of the elements or even the order of the base functions in order to capture the phenomena with more detail. Within the user interface meshing program of the Ansys suite we can use the so called size boxes. Those boxes have as a main function not to allow the element size increase above one specific value. We did place two of those boxes one in the wing and fuselage and one around the empennage. Other techniques are to gradually decrease and increase the size of the elements across the domain so that there is some room for the element size transition to happen.
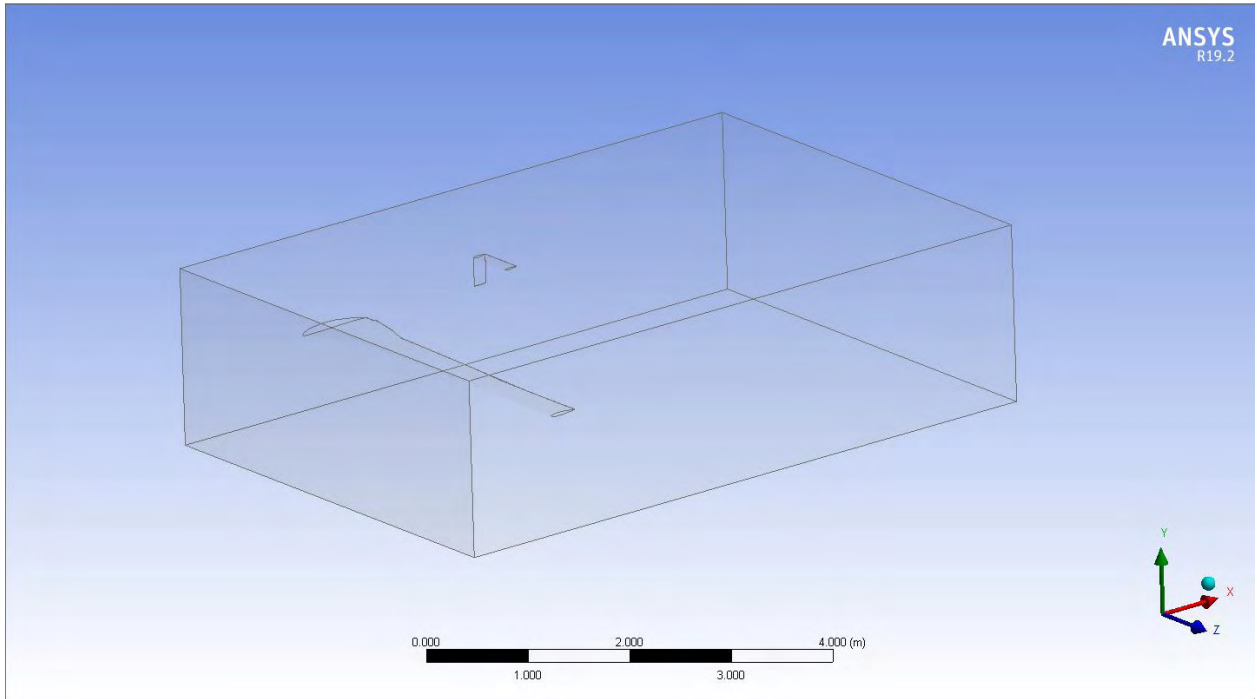
Figure 4-8: Control Volume of the uav without the size boxes
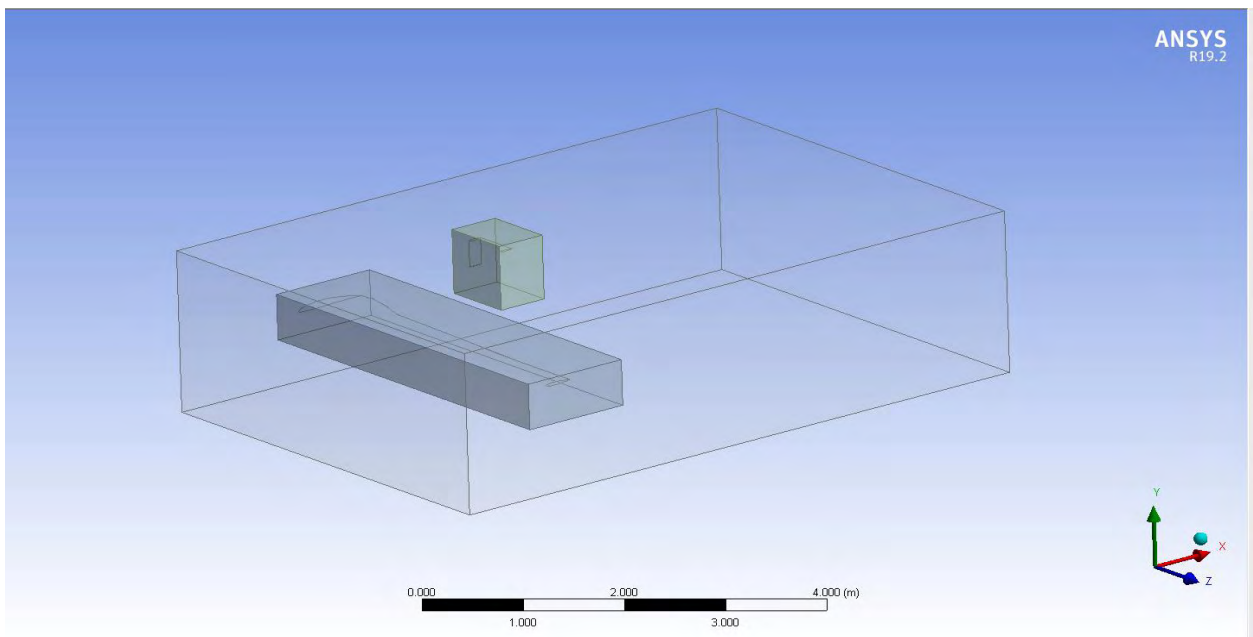
Figure 8: Fluid domain with the size boxes included

While at the preprocessing section it is commonly used to name the planes of the domain so that the program will automatically define those with the correct boundary conditions. All of the faces that define the wing and the empennage we will apply the boundary condition later on while solving. All the other areas are named based on the property of the face. In example we have the velocity inlet as well as the pressure outlet and all the plane surrounding faces are called symmetry.
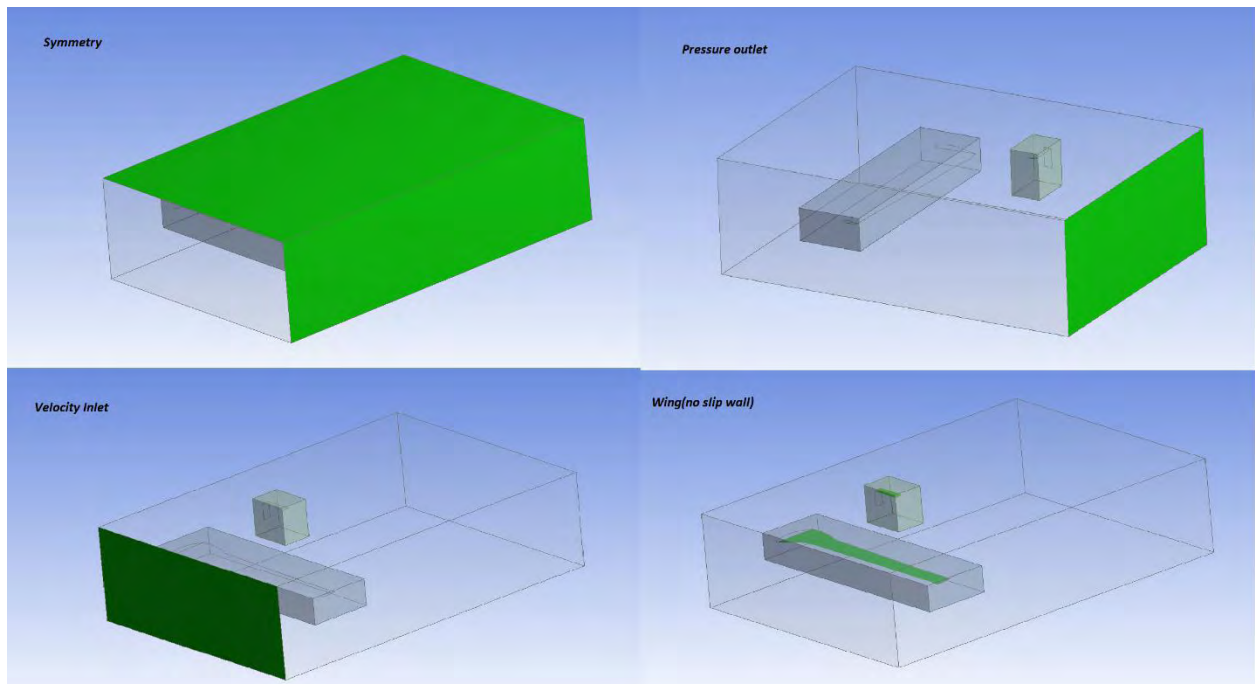
Figure 4-9: All the faces that boundary conditions will be applied.

4.1.2. Meshing

Meshing is the part of the simulation that the whole domain will be discretized into finite elements. The meshing process begins with defining the type of meshing that the user wants to generate. The two main categories are the structured and unstructured mesh.

Structured grids are identified by regular connectivity. The possible element choices are quadrilateral in 2D and hexahedra in 3D. This model is highly space efficient, since the neighborhood relationships are defined by storage arrangement. Some other advantages of structured grid over unstructured are better convergence and higher resolution. While on the other
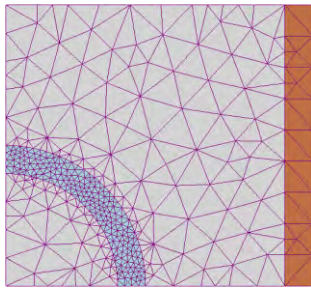
Figure4-10: Unstructured grid
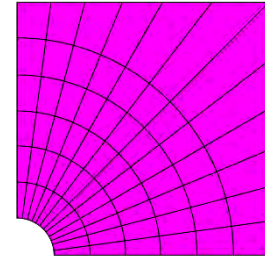
Figure 4-11: Structured grid

hand. An unstructured grid is identified by irregular connectivity. It cannot easily be expressed as a two-dimensional or three-dimensional array in computer memory. This allows for any possible element that a solver might be able to use. Compared to structured meshes, this model can be highly space inefficient since it calls for explicit storage of neighborhood relationships. These grids typically employ triangles in 2D and tetrahedral in 3D. The second one is a more robust because the existence of small triangular in 2D and pyramids in the 3D allows for small gap filling without increasing excessively the amount of elements that we use. The combination of those two types of elements create another category the Hybrid one where the structured grid is used in easy to create areas while in the tighter areas the pyramids can fill the hardest areas.

The first step is the surface meshing procedure which is imposing of the estimated average element size on the whole vehicle geometry. The most common type of elements that is used for a CFD simulation is the triangle elements. Triangle cells are shaped of 3 sides and is one of the simplest types of mesh. The faceted triangular surface resolution has to meet several requirements. For a typical airplane shape, pressure or form drag is dominant over skin friction, so the accuracy of the drag and lift predictions are largely determined by the accuracy of the predicted static pressure distribution on the body. This pressure distribution is strongly affected by the locations of flow separation and reattachment. Even though that the mesh must be very fine in the critical regions there is still the problem of knowing where these regions are and how fine the mesh should be. Along solid surfaces there will be a boundary layer and so there must be several points close to the surface in a direction normal to the surface. This allows the numerical solution to model the rapid variation in velocity through the boundary layer. Another example is where a surface has a large amount of

curvature causing a rapid variation in pressure in the flow direction. However, large flow gradients also exist in areas of the flow away from the solid surfaces, like in the wake behind the car. Creating a suitable mesh in these areas is more difficult as the exact location of the critical areas is difficult to determine.
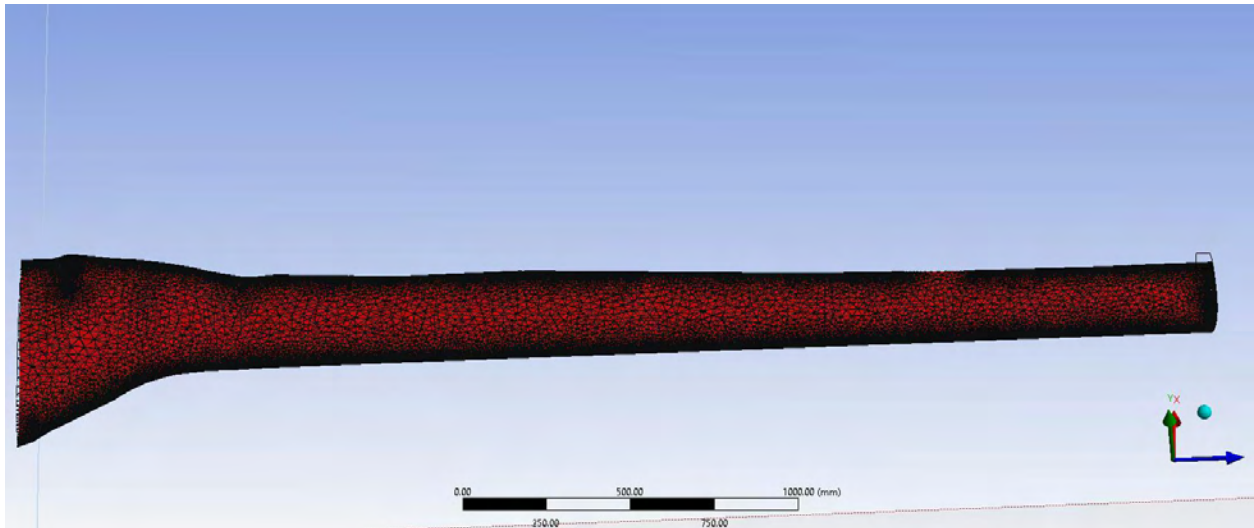
Figure 4-12: Typical trias surface mesh

After the average element size is defined the user defines the range of the element size and the maximum acceptable angle between two adjacent vectors of an element and the choice for the algorithms to try to capture the curvature of the geometry which is really important because otherwise the surface will be destroyed or it will not have the desired resolution. Typical values of the curvature normal angle are between 12 to 18 degrees (the smaller the angle the finer the mesh). In all our cases previously and after the mesh dependency we did chose 12 degrees which corresponds to fine meshing. We can also see in the picture above that around the half of the chord where the curvature of the wing is not changing dramatically like in the leading edge the size of the cells is greater and this is caused by the above normal angle.

After the surface meshing is complete on all the areas of the control volume we will create some elements that are called the layers. As we know from basic fluid dynamics when a fluid comes in contact with a wall then the friction between the fluid layers cause the fluid

speed to decrease when getting closer to the wall where we make the hypothesis that the fluid has zero speed (no slip condition). Thus the viscosity of the fluid is responsible for the creation of the boundary layer. In order to capture the friction effects between the fluid and the surface and calculate the friction fraction of the drag in our device we need to generate the layers which practically is an extrusion of the pre-generated surface elements. Getting a proper layer generation is not an easy task because of their prism shape they cannot be fitted everywhere with the criteria that we set. Proximities my cause these elements to intersect and create overlapping faces or even elements that exist in the same place in space. Before the generation exist the user needs to have an idea of the boundary layer thickness because this will define the number and the size of the cells. The first element size was determined by the use of Y+ calculator that had as inputs the velocity the density and the dynamic viscosity we took as a result the height of the first layer and the local Reynolds number.
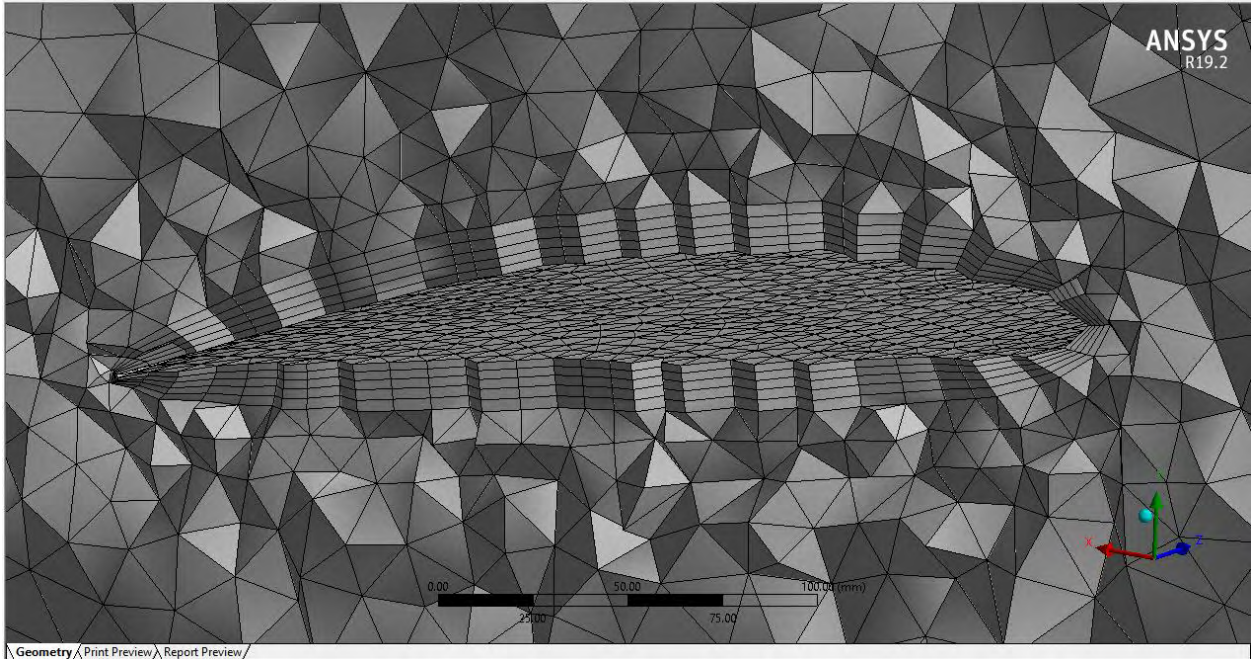
Figure 4-13: Layers generation

As we can see in the figure above the augmented elements that come in contact with the faces of the airfoil are the boundary layer ones. Ansys has lots of algorithms for defining the layers the most commonly used is by giving the aspect ratio of size to thickness of the first

layer and then the growth size which multiplies the height of the previous layer and thus the height is growing when moving away from the wall. That way the mesh tends to be denser closer to the airfoil where the great pressure gradients exist and sparser away from the surface where the velocity profile tends to become linear.

The last part and the less painful is the volume mesh creation. It is mentioned that the boundary layer elements have volume but we describe them as boundary and we don't include them in the volume mesh because of the specific use they have in the whole meshing process. That said the rest of the volume elements will be generated between the layers of adjacent areas. This process is easier than the previous two because there are no geometry anomalies that will disturb our mesh nor have the trend to interfere with each other. Furthermore, the prism element is having the most convenient shape and can easily fil gaps and still have high quality criteria. Our final mesh belongs in the hybrid mesh category since the most part is made up with prisms which though coexist with tetras or hexas. Just like the surface mesh size, the two size boxes for the airplane model and the single one for the wing simulation will also regulate the size of the volume mesh.
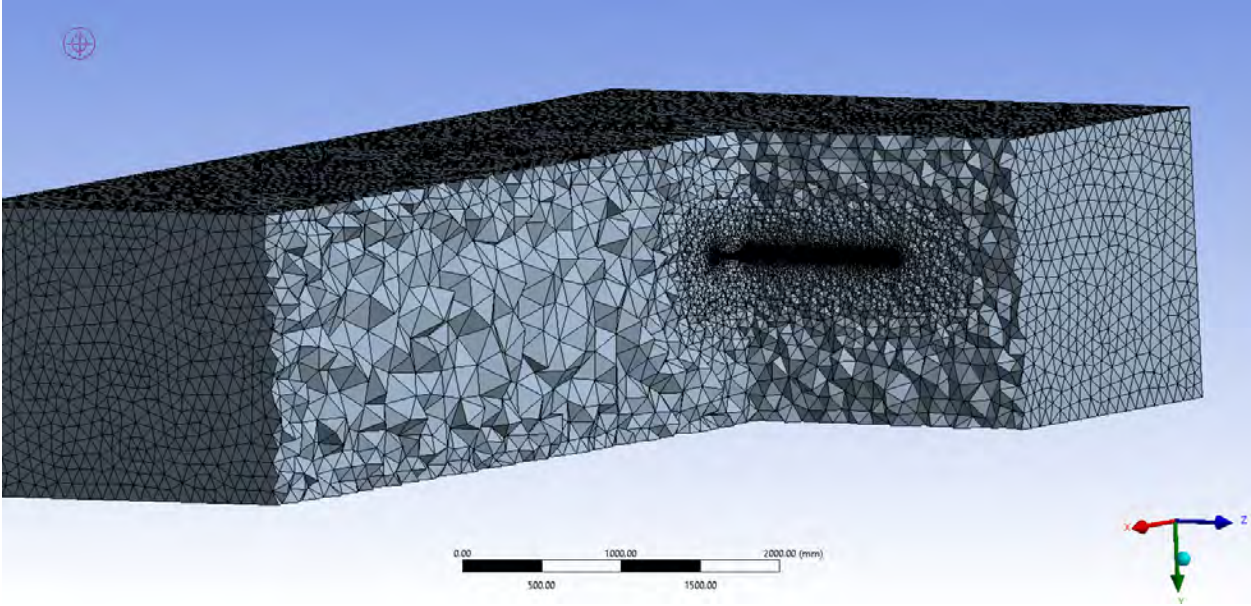
Figure 4-14: Volume mesh

4.1.3. Solving Process

After the *pre*-Processing is completed and all the models are successfully meshed the CFD cases are ready to be solved, using ANSYS-*Fluent.* At this section are defined the numerical methods and the parameters of the CFD solver like the solving algorithms, the turbulence models, the boundary conditions, the convergence criteria, the monitors of interest, the number of iterations and anything else needed to properly solve each case. The governing equations for the time dependent three-dimensional fluid flow and heat transfer around a body are the continuity equation, momentum equations and energy equation. The general approach in long range glider or uav external aerodynamics is to assume incompressible and isothermal flow, as Ma << 0.3, which is in the velocity of 20-30m/s with common altitude 2000m and it is unlikely that the flow will reach this velocity anywhere in the domain. Thus, the energy equation can be neglected and the momentum- and continuity equations can be written on incompressible form, neglecting the density terms. The same solver settings are used for all the models, so they are going to be described only once for all the cases. On the diagram bellow are shown the steps of the solving process as they are followed for all models, until the final results reach the desired accuracy. The steps that will be described in this chapter can be summarized and presented in the following schematic.
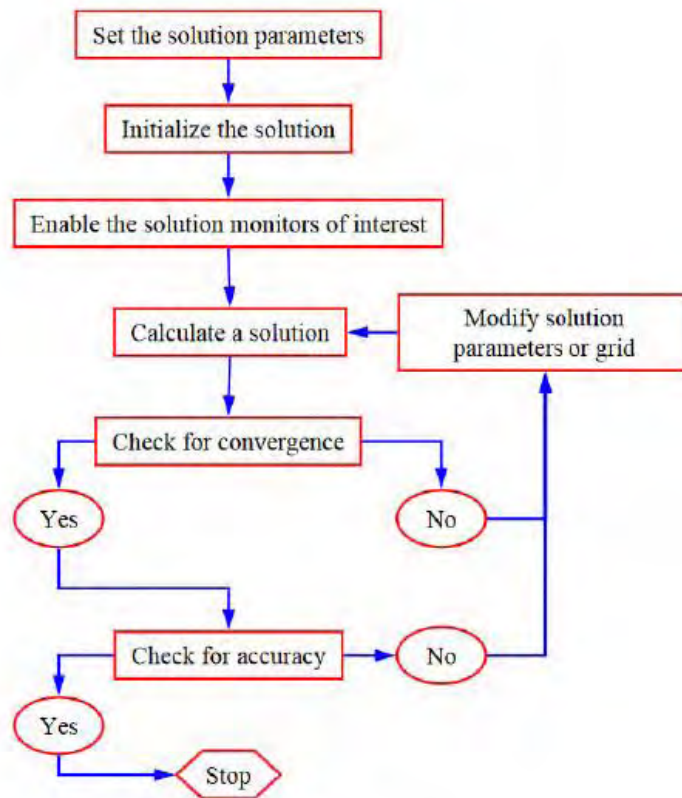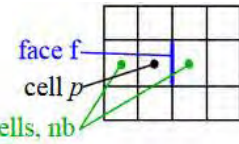
Figure 4-15: Solution process

Fluent solvers are based on the finite volume method where the Fluid Domain is discretized into a finite set of control volumes or cells. The general transport equation (*3.1*) for mass, momentum, energy, etc. is applied to each cell and discretized and all equations are solved in or der to render the flow field.

$$\underbrace{\frac{\partial}{\partial t}\int_V \rho\phi\,dV}_{\text{Unsteady}} + \underbrace{\oint_A \rho\phi\mathbf{V}\cdot d\mathbf{A}}_{\text{Convection}} = \underbrace{\oint_A \Gamma\nabla\phi\cdot d\mathbf{A}}_{\text{Diffusion}} + \underbrace{\int_V S_\phi\,dV}_{\text{Generation}}$$

Each transport equation is discretized into algebraic form. For a given cell, P:

$$\frac{\left(\rho\phi_p\right)^{t+\Delta t}-\left(\rho\phi_p\right)^{t}}{\Delta t}\Delta V + \sum_{faces}\rho_f\,\phi_f\,V_f\,A_f = \sum_{faces}\Gamma_f\left(\nabla\phi\right)_{\perp,f}A_f + S_\phi\,\Delta V$$

Discretized equations require information at both cell centers and faces. Field data (*material properties, velocities, etc.*) are stored at cell centers. Face values are interpolated in terms of local and adjacent cell values while the discretization accuracy depends on the "*stencil*" size. The discretized scalar transport equation contains the unknown scalar variable at the cell center as well as the unknown values in surrounding neighbor cells. This equation will, in general, be nonlinear with respect to these variables. The discretized equation (*3.3*) can be expressed simply as:

$$a_P\phi = \sum_{nb}a_{nb}\phi_{nb} + b$$

where the subscript *nb* refers to neighbor cells, and $\alpha_{p\ and\ \alpha nb}$ are the linearized coefficients for φ and φ_{nb}. The above equation is written for every control volume in the domain resulting in equation sets which are solved iteratively. Coefficients $\alpha_{p\ and\ \alpha nb}$ are typically functions of solution variables (*nonlinear and coupled*), they are written to use values of solution variables from the previous iteration and they are updated with each outer iteration.

The *Pressure-Based* solver is selected by default on the Solver Type field and is used for all models. In this case, the coefficients $\alpha_{p\ and\ \alpha nb}$ are scalar values. This type of solver employs an algorithm which belongs to a general class of methods called the projection method. In the projection method, wherein the constraint of mass conservation (*continuity*) of the velocity field is achieved by solving a pressure (*or pressure correction*) equation. The pressure equation is derived from the continuity and the momentum equations in such a way that the velocity field, corrected by the pressure, satisfies the continuity. Since the governing equations are nonlinear and coupled to one another, the solution process involves iterations wherein the entire set of governing equations is solved repeatedly until the solution

converges. The *Pressure-Based* solver takes momentum and pressure as the primary variables while pressure-velocity coupling algorithms are derived by reformatting the continuity equation. The *Pressure-Based* solver is applicable for a wide range of flow regimes from low speed incompressible flow to high-speed compressible flow and usually requires less memory (*storage*). It allows also flexibility in the solution procedure while the *Pressure-Based* coupled solver (*PBCS*) that is used, is applicable for most single-phase flows. Finally, all CFD simulations are done as *Steady* cases, at one moment without any timestep being used on the Time field.

Since the airflow around a glider is turbulent, a model needs to be selected for simulation of the turbulent flow. There appears to be four major turbulence models that are used in the avionics industries: *k-ε, k-ω, Lattice-Boltzmann* and *Large Eddy Simulation (LES)*. Of these models the k-ε and k-ω are most widely used with the k-ε said to be the most stable. The fidelity of CFD predictions for turbulent flow is highly dependent upon the quality of the turbulence modeling. This is even more important for the flow around aerial vehicles, whose salient flow features include three-dimensional boundary layers with strong streamline curvature, separation and strong vortices. These features require turbulence models that can properly account for *Non-Equilibrium* effects and anisotropy.

On the viscous model card that appears k-epsilon model is selected, which specifies turbulent flow to be calculated using one of three *k-epsilon* models bellow. For all the cases, *Realizable k-epsilon* model is used. Industrial applications of this model show that it is possible to achieve good results in terms of integral values (e.g., drag coefficient), which are within *2-5%*. Due to its implementation, it is very stable and fast converging. Therefore, it is perfectly suited for automated calculation processes, allowing a huge number of calculations in a relatively small time frame. The *Realizable k-ε* model is a relatively recent development and differs from the standard *k-ε* model in two important ways. The realizable *k-ε* model contains a new formulation for the turbulent viscosity and a new transport equation for the dissipation rate, *ε* has been derived from an exact equation for the transport of the mean-square vorticity fluctuation. The term "*Realizable*'' means that the model satisfies certain mathematical constraints on the Reynolds stresses, consistent with the physics of turbulent flows. Neither the standard *k-ε* model nor the RNG k-*ε* model is realizable.

An immediate benefit of the realizable k-*ε* model is that it more accurately predicts the spreading rate of both planar and round jets. It is also likely to provide superior performance

for flows involving rotation, boundary layers under strong adverse pressure gradients, separation, and recirculation. Both the *Realizable* and *RNG k-ε* models have shown substantial improvements over the standard *k-ε* model where the flow features include strong streamline curvature, vortices, and rotation. Since the model is still relatively new, it is not clear in exactly which instances the *Realizable k-ε* model consistently outperforms the *RNG* model. However, initial studies have shown that the realizable model provides the best performance of all the *k-ε* model versions for several validations of separated flows and flows with complex secondary flow features. One of the weaknesses of the *Standard k-ε* model or other traditional k-ε models lies with the modeled equation for the dissipation rate (*ε*) limitation of the *Realizable k-ε* model is that it produces non-physical turbulent viscosities in situations when the computational domain contains both rotating and stationary fluid zone. This is due to the fact that the *Realizable k-ε* model includes the effects of mean rotation in the definition of the turbulent viscosity. This extra rotation effect has been tested on single rotating reference frame systems and showed superior behavior over the S*tandard k-ε* model. However, due to the nature of this modification, its application to multiple reference frame systems should be taken with some caution.

To understand the mathematics behind the *Realizable k-epsilon* model, consider combining the *Boussinesq* relationship *(3.4)* and the *Eddy Viscosity (μ$_t$)* definition *(3.5)* to obtain the following expression (3.6) for the normal *Reynolds Stress* in an incompressible strained mean flow:

$$-\rho\overline{u_i'u_j'}=\mu_t\left(\frac{\partial u_i}{\partial x_j}+\frac{\partial u_j}{\partial x_i}\right)-\frac{2}{3}\left(\rho k+\mu_t\frac{\partial u_k}{\partial x_k}\right)\delta_{ij}$$

$$\mu_t=\rho C_\mu\frac{k^2}{\varepsilon}$$

$$\overline{u^2}=\frac{2}{3}k-2v_t\frac{\partial U}{\partial x}$$

Using *3.5* equation for $v_t = \mu_t \rho$, one obtains the result that the normal stress $\bar{u_z}$, which by definition is a positive quantity, becomes negative, that is, "*non-Realizable*", when the strain is large enough to satisfy *3.7* equation.

$$\frac{k}{\varepsilon} \frac{\partial U}{\partial x} > \frac{1}{3C_\mu} \approx 3.7$$

The modeled transport equations for *k* and *ε* in the realizable k-*ε* model are:

$$\frac{\partial}{\partial t}(\rho k) + \frac{\partial}{\partial x_j}(\rho k u_j) = \frac{\partial}{\partial x_j}\left[\left(\mu + \frac{\mu_t}{\sigma_k}\right)\frac{\partial k}{\partial x_j}\right] + G_k + G_b - \rho\varepsilon - Y_M + S_k$$

$$\frac{\partial}{\partial t}(\rho\varepsilon) + \frac{\partial}{\partial x_j}(\rho\varepsilon u_j) = \frac{\partial}{\partial x_j}\left[\left(\mu + \frac{\mu_t}{\sigma_\varepsilon}\right)\frac{\partial\varepsilon}{\partial x_j}\right] + \rho C_1 S\varepsilon - \rho C_2 \frac{\varepsilon^2}{k+\sqrt{v\varepsilon}} + C_{1\varepsilon}\frac{\varepsilon}{k}C_{3\varepsilon}G_b + S_\varepsilon$$

$$C_1 = \max\left[0.43, \frac{\eta}{\eta+5}\right] , \eta = S\frac{k}{\varepsilon} , S = \sqrt{2S_{ij}S_{ij}}$$

The model constants C_2, σ_k *and* σ_ε have been established to ensure that the model performs well for certain canonical flows. The model constants are:

$$C_{1\varepsilon} = 1.44, \ C_2 = 1.9, \ \sigma_k = 1.0, \ \sigma_\varepsilon = 1.2$$

The next field to be filled is the *Near-Wall Treatment,* which specifies the near-wall treatment to be used for modeling turbulence. *Non-Equilibrium Wall Functions* is used

for all the CFD cases. The key elements in the *Non-Equilibrium Wall Functions* are the Launder and Spalding's log-law for mean velocity is sensitized to pressure-gradient effects and the two-layer-based concept which is adopted to compute the budget of turbulence kinetic energy ($G_{\overline{k}}$,) in the wall-neighboring cells. The log-law for mean velocity sensitized to the pressure gradients is:

$$\frac{\tilde{U} C_\mu^{1/4} k^{1/2}}{\tau_w / \rho} = \frac{1}{\kappa} \ln \left(E \frac{\rho C_\mu^{1/4} k^{1/2} y}{\mu} \right)$$

$$\tilde{U} = U - \frac{1}{2} \frac{dp}{dx} \left[\frac{y_v}{\rho \kappa \sqrt{k}} \ln \left(\frac{y}{y_v} \right) + \frac{y - y_v}{\rho \kappa \sqrt{k}} + \frac{y_v^2}{\mu} \right]$$

The non-equilibrium wall function employs the two-layer concept in computing the budget of turbulence kinetic energy at the wall-adjacent cells, which is needed to solve the k equation at the wall-neighboring cells. The wall-neighboring cells are assumed to consist of a viscous sublayer and a fully turbulent layer. The following profile assumptions for turbulence quantities are made:

$$\tau_t = \begin{cases} 0, & y < y_v \\ \tau_w, & y > y_v \end{cases} \quad k = \begin{cases} \left(\frac{y}{y_v} \right)^2 k_P, & y < y_v \\ k_P, & y > y_v \end{cases} \quad \varepsilon = \begin{cases} \frac{2 v k}{y^2}, & y < y_v \\ \frac{k^{3/2}}{C_l^* y}, & y > y_v \end{cases}$$

Using these profiles, the cell-averaged production of k, $G_{\overline{k}}$, and the cell-averaged dissipation rate $\overline{\varepsilon}$, can be computed from the volume average of and of the wall-adjacent cells. For quadrilateral and hexahedral cells for which the volume average can be approximated with a depth-average:

$$\overline{G_k} \equiv \frac{1}{y_n} \int_0^{y_n} \tau_t \frac{\partial U}{\partial y} dy = \frac{1}{\kappa y_n} \frac{\tau_w^2}{\rho C_\mu^{1/4} k_P^{1/2}} \ln \left(\frac{y_n}{y_v} \right)$$

$$\bar{\varepsilon} \equiv \frac{1}{y_n} \int_0^{y_n} \varepsilon \, dy = \frac{1}{y_n} \left[\frac{2v}{y_v} + \frac{k_P^{1/2}}{C_l^*} \ln\left(\frac{y_n}{y_v}\right) \right] k_P$$

The next step in the simulation process is to define the boundary conditions around the domain. Altering the boundary condition alters the whole domain solution and choosing the proper once is an issue of vital importance for the integrity and the rightness of the results. Besides the kind of the surface that we need to define and give some values to the speed and the pressure on them we also need to define the turbulence intensity I in the inlet and in the pressure outlet.

$$I = \frac{u'}{U'}$$

Where u' is the root-mean-square of the turbulent velocity fluctuations and U is the mean velocity. If the turbulent energy k is known u' can be computed as:

$$u' = \sqrt{\frac{1}{3}(u'^2_x + u'^2_y + u'^2_z)} = \sqrt{\frac{2}{3}k}$$

Turbulence intensity varies based on the kind of problem. Consulted by the fluent physics manuals the free stream intensity is around 1% while for cases like turbofans turbos and propellers peaks at around 5%. Since in this simulation the propeller and its rotation will not be included we have no reason to increase the intensity beyond 2% both on inlet and on outlet.

The boundary conditions that the user directly applies to the problem are of two types. The so called Dirichlet boundary condition which is a first-type and it defines the value of a function in a specific along the chosen boundary of the domain. This boundary condition is met in the inlet where the velocity is specified and at the outlet where the pressure is defined to match the altitude pressure of the flight. The second one is the Neumann or second type boundary condition and it is used to describe the rate of change or in more

⏻ inlet (velocity-inlet, id=6)
⏻ interior-solid (interior, id=1)
⏻ outelt (pressure-outlet, id...
⏻ symmetry (symmetry, id=5)
⏻ wing (wall, id=8)

Figure 4-16: Boundary conditions used

mathematical terms the derivative or the gradient of the function in a boundary. This condition is applied to all the symmetrical planes where the derivative is set to zero.

In the inlet boundary condition tab, the user can choose either to give the specified value and the normal of the plane that the velocity vector is parallel to or to either give the components of the velocity on each direction respectively. In the 2D simulation stage in Ansys a commonly used technique is to create a circular inlet curve and that way the user can save time by creating only once the mesh and then change the velocity compounds in order to achieve the desired angle of attack in the airfoil as shown below.
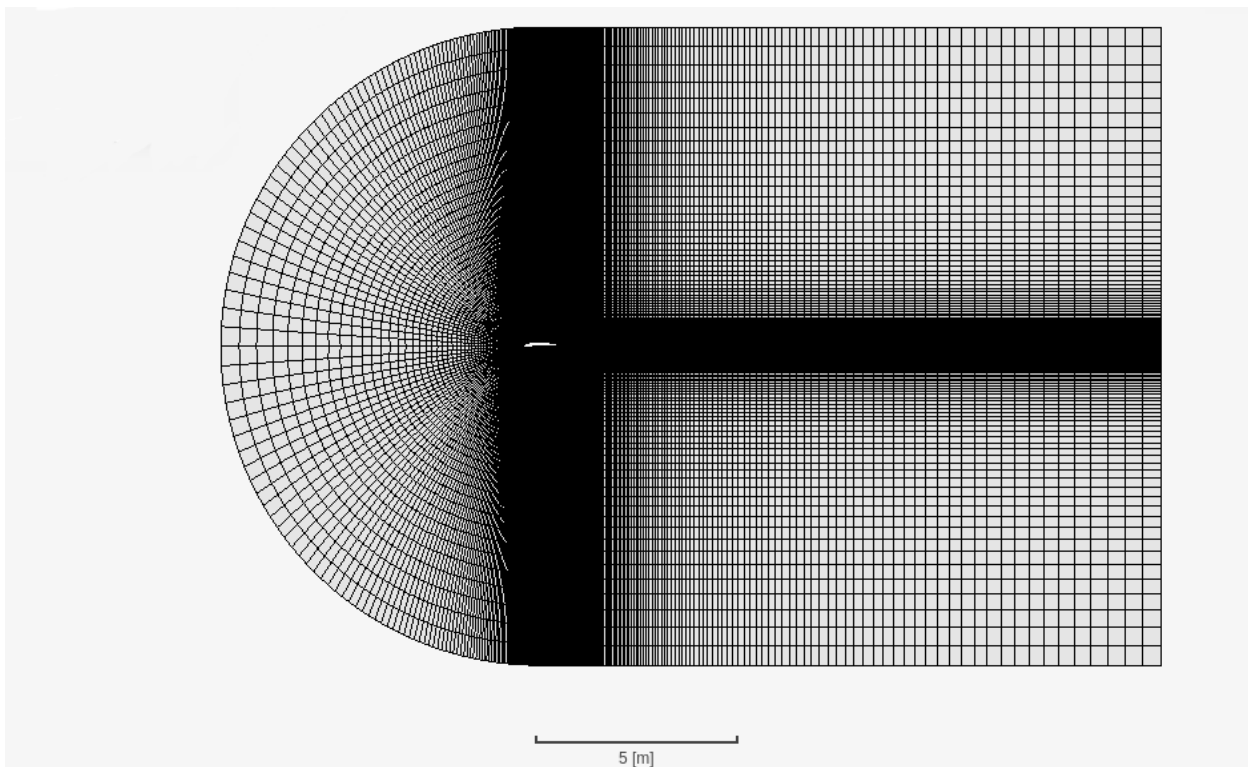
Figure 4-17 Curved Control Volume Inlet

But in our case since each model case will run in a different geometry and the mesh has to be generated from the beginning the control volume has a uniform shape and to define the inlet velocity we just need to define the amplitude of it and the normal vector to the inlet plane will define the direction of the velocity. As mentioned above the inlet boundary

clearance has to be large enough so that the flow field in front of the object has space to evolve and thus the stagnation points will calculate the pressure with greater precision.
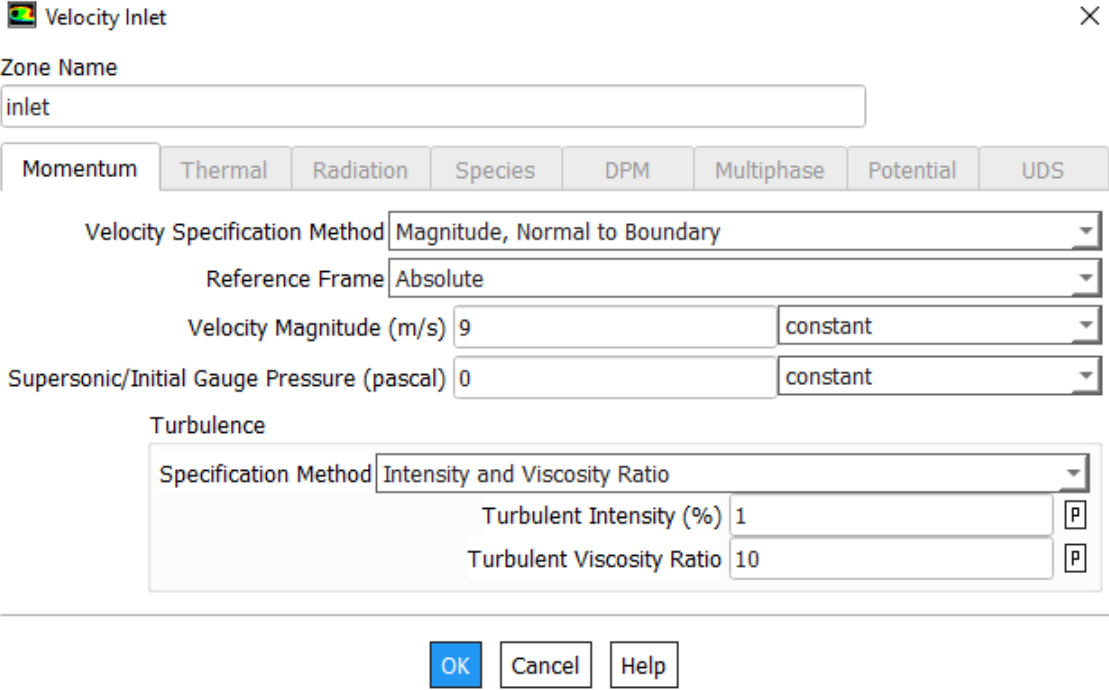
Figure 4-18: Inlet boundary condition tab

The pressure outlet boundary defines the absolute static pressure that initially is applied in all the cells of the computational grid before the iterative solution process begins. In our case taking into consideration that the flight can occur at altitudes around 2000 meters the density of the air at that height is equal to 1 and the atmospheric pressure is around 79.000 Pa. Both here and in the inlet section the turbulent intensity was set to 1 due to the low Reynolds number and due to the fact that in the most area of the UAV the flow remains undisturbed and not great mix phenomena occur.

During the pre-procession chapter, we referred that using only the half of the model for the simulation will save us computational time and memory storage space. This symmetry plane is defined by using the symmetry boundary condition which mathematically can be described as

$$\frac{\partial \Phi}{\partial x} = 0 \ @ \ B_u$$

Where the term Φ corresponds to each variable that is calculated in the boundary (pressure, velocity, density, temperature, etc), and B_u is the boundaries where the symmetry condition is applied.

And the final boundary condition for our external aerodynamics case is the one that can be separated into two different conditions. This boundary condition kind is called wall and there are a lot of different problems where it can be applied. It can either describe a stationary wall there the no slip condition is applied or even a moving wall where the velocity of the fluid right above the wall is equal to the translating speed of the wall. If someone has data about the slip of the fluid, then he can also define a specific shear on that wall. In our case and generally in airfoil study the condition is described as shown below:

$$\vec{u} \cdot \vec{n} = 0$$

Where u is the velocity above the airfoil and $\vec{n}$ is the normal vector to the surface. The component on a direction perpendicular to the surface has to be zero also known as no penetration condition and implies that the fluid particles cannot penetrate our geometry otherwise our geometry will be considered as a porous medium and the second one is the no slip condition where the fluid layer right above the geometry does not slip on it.
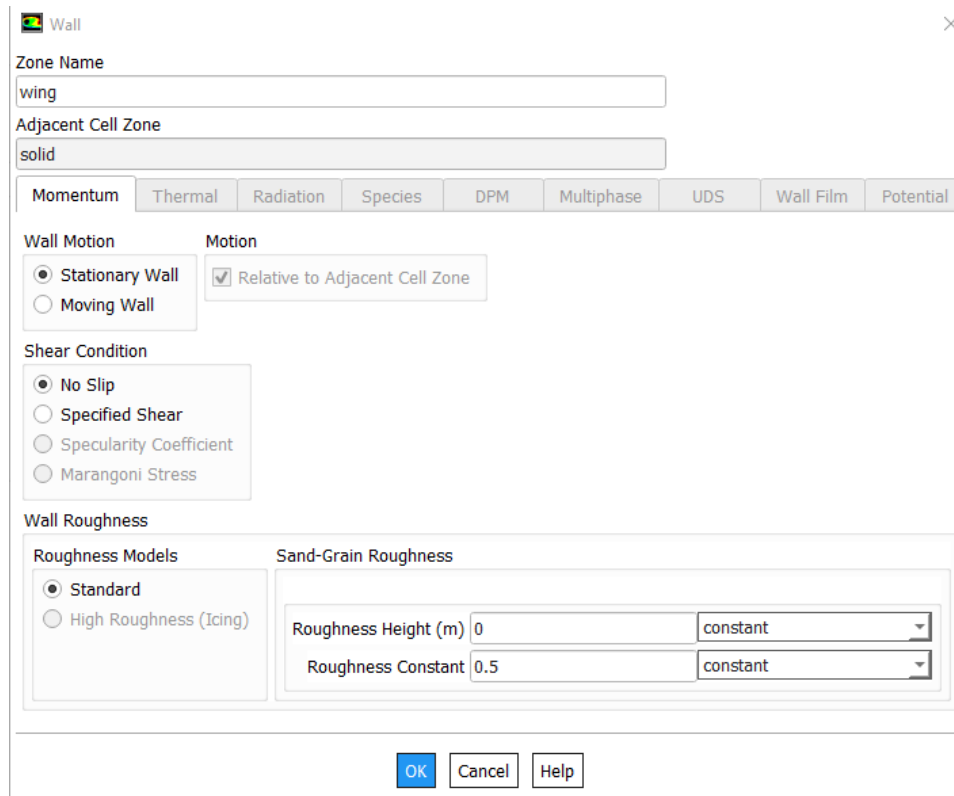
Figure 4-19:Wall boundary condition

Scheme provides a drop-down list of the available pressure-velocity coupling schemes while as previously mentioned, the *Pressure-Based* solver allows to solve flow problems in either a *Segregated* or *Coupled* manner. The *Coupled* algorithm is selected because it obtains a robust and efficient single phase implementation for steady-state flows, with superior performance compared to the *segregated* solution schemes. The Pressure-Based Segregated algorithm solves the momentum equation and pressure correction equations separately, but this semi-implicit solution method results in slow convergence. The Coupled algorithm on the other hand, solves the momentum and pressure-based continuity equations together. However, the memory requirement increases by 1.5 - 2 times that of the segregated algorithm since the discrete system of all momentum and pressure-based continuity equations must be stored in the memory when solving for the velocity and pressure fields (rather than just a

single equation, as is the case with the segregated algorithm). The full implicit coupling is achieved through an implicit discretization of pressure gradient terms in the momentum equations, and an implicit discretization of the face mass flux, including the Rhie-Chow pressure dissipation terms.

In the momentum equations, the pressure gradient for component k is of the form:

$$\sum_f p_f A_k = -\sum_j a^{u_k p} p_j$$

Where $a^{u_k p}$ is the coefficient derived from the Gauss divergence theorem and coefficients of the pressure interpolation schemes. Finally, for any i^{th} cell, the discretized form of the momentum equation for component u_k is defined as:

$$\sum_j a_{ij}^{u_k u_k} u_{kj} + \sum_j a_{ij}^{u_k p} p_j = b_i^{u_k}$$

As a result, the overall system of equations (*3.18*) and (*3.19*), after being transformed to the *δ-form*, is presented as:

$$\sum_j [A]_{ij} \vec{X}_j = \vec{B}_i$$

where the influence of a cell i on a cell j has the form:

$$A_{ij} = \begin{bmatrix} a_{ij}^{pp} & a_{ij}^{pu} & a_{ij}^{pv} & a_{ij}^{pw} \\ a_{ij}^{up} & a_{ij}^{uu} & a_{ij}^{uv} & a_{ij}^{uw} \\ a_{ij}^{vp} & a_{ij}^{vu} & a_{ij}^{vv} & a_{ij}^{vw} \\ a_{ij}^{wp} & a_{ij}^{wu} & a_{ij}^{wv} & a_{ij}^{ww} \end{bmatrix}$$

Spatial Discretization contains settings that control the spatial discretization of the convection terms in the solution equations. *Gradient* contains a drop-down list of the options for setting the method of computing the gradient. Gradients are needed not only for constructing values of a scalar at the cell faces, but also for computing secondary diffusion terms and velocity derivatives. The gradient $\nabla \varphi$ of a given variable φ is used to discretize the convection and diffusion terms in the flow conservation equations. The *Least Squares Cell-Based* gradient method t is selected and used for all the CFD models. In this method, the solution is assumed to vary linearly. In Cell Centroid Evaluation, the change in cell values

between cell c_0 and c_i along the vector r_i from the centroid of cell c_0 to cell c_i, can be expressed as:

$$\left(\nabla\phi\right)_{c0}\cdot\Delta r_i=\left(\phi_{ci}-\phi_{c0}\right)$$

If similar equations are used for each cell surrounding the cell c_0 and assuming that J is the coefficient matrix that is purely a function of geometry, the following system is written in a compact form as:

$$[J]\left(\nabla\phi\right)_{c0}=\Delta\phi$$

The objective here is to determine the cell gradient ($\nabla\varphi_0$) by solving the minimization problem for the system of the non-square coefficient matrix in a least-squares sense. The above linear-system of equation is over-determined and can be solved by decomposing the coefficient matrix using the Gram-Schmidt process. This decomposition yields a matrix of weights ($W_{i0x,0y}$, W_{i0z}) for each cell. Thus, for our cell-centered scheme this means that the three components of the weights () are produced for each of the faces of cell c_0. Therefore, the gradient at the cell center can then be computed by multiplying the weight factors by the difference vector $\Delta\varphi=(\varphi_{c1}-\varphi_{c0})$ as:

$$\left(\phi_x\right)_{c0} = \sum_{i=1}^{n}W^x_{i0}\cdot\left(\phi_{ci}-\phi_{c0}\right)$$

$$\left(\phi_y\right)_{c0} = \sum_{i=1}^{n}W^y_{i0}\cdot\left(\phi_{ci}-\phi_{c0}\right)$$

$$\left(\phi_z\right)_{c0} = \sum_{i=1}^{n}W^z_{i0}\cdot\left(\phi_{ci}-\phi_{c0}\right)$$

After the initialization of every case that we run the spatial discretization technique that we did use was the first order upwind for the pressure and momentum and after 100 iterations we chose the second order one. The above technique was used during our experience with the FSAE aerodynamics team and it was observed to give faster convergence.

4.1.4. Mesh Dependency

While using finite differences or finite volume or finite element methods someone can tell that the denser the computational grid the more accurate our solution and our simulation prediction will be. At some point though our solution will converge to a certain value and further increasing the number of our elements will have no practical meaning to our solution we need to find a point where our solution is no longer mesh depended. This will help us keep the calculation time low and will save us a lot of time. Our mesh independency plan started by using the default mesh as a starting point with no size boxes placed in the geometry domain. The next step was to place some size boxes around our wing and decrease both locally and globally the average volume element size as well as the surface element size on the wing. During this process the number of the boundary layer elements was constant and the mesh densing strategy is shown in the table and diagrams below. For all the simulations we used the PSU airfoil placed in 6 degrees angle of attack and at 10m/s flying speed.

case	Max size	Min Size	Element size	Body Sizing	Face sizing	curvature angle	cells	faces	nodes
					Mesh Criteria				
default	636	3.181	318.1	-	-	18			
1	300	1.5	150	100	100	12	3143345	6721416	802656
2	150	1	100	80	80	12	3235300	6910643	821009
3	150	1	100	40	40	12	3699260	7840624	900148
4	150	1	100	40	20	12	8401496	17420789	1843661
5	150	1	100	40	10	12	8699073	18055803	1921450
6	100	1	100	40	10	12	8735693	18129194	2102126

Figure 4-20: Meshing refinement process

We can see that the mesh refinement procedure took into consideration both the volume element size and the face element size. Both of them have impact on the solution since greater number of face elements means that we have a more precise expression of the pressure field above the wing the when the surface integration happens we have more

information about the distribution and thus the result represents the drag and the lift components more precisely. The volume mesh on the other way do play an important role since the pressure right above the wing is affected by the pressure of the field around it in a more indirect way. The above table along with the following diagrams can ensure us that the face sizing plays a greater impact in the precision of the results. The huge jump in the diagrams happened when the face size was halved during the 4rth refining stage. Further decrease in the size of both face and volume elements there was no impactful change in the values of the lift drag and their relative errors and therefore we can assume that our solution is considered mesh independent. Both of the drag and lift diagrams and their errors have the same behavior while increasing the number of the cells. The peak value indicates again that the face element size decrease has the greatest impact. Since we had no exact solution for the problem and no experimental data to compare, the relative error was calculated by the next formula:

$$e_i = \frac{F_i - F_{i-1}}{F_i},$$

Where F_i corresponds to each function (lift, drag, x_p, etc) of the current simulation and the F_{i-1} term of the previous one.
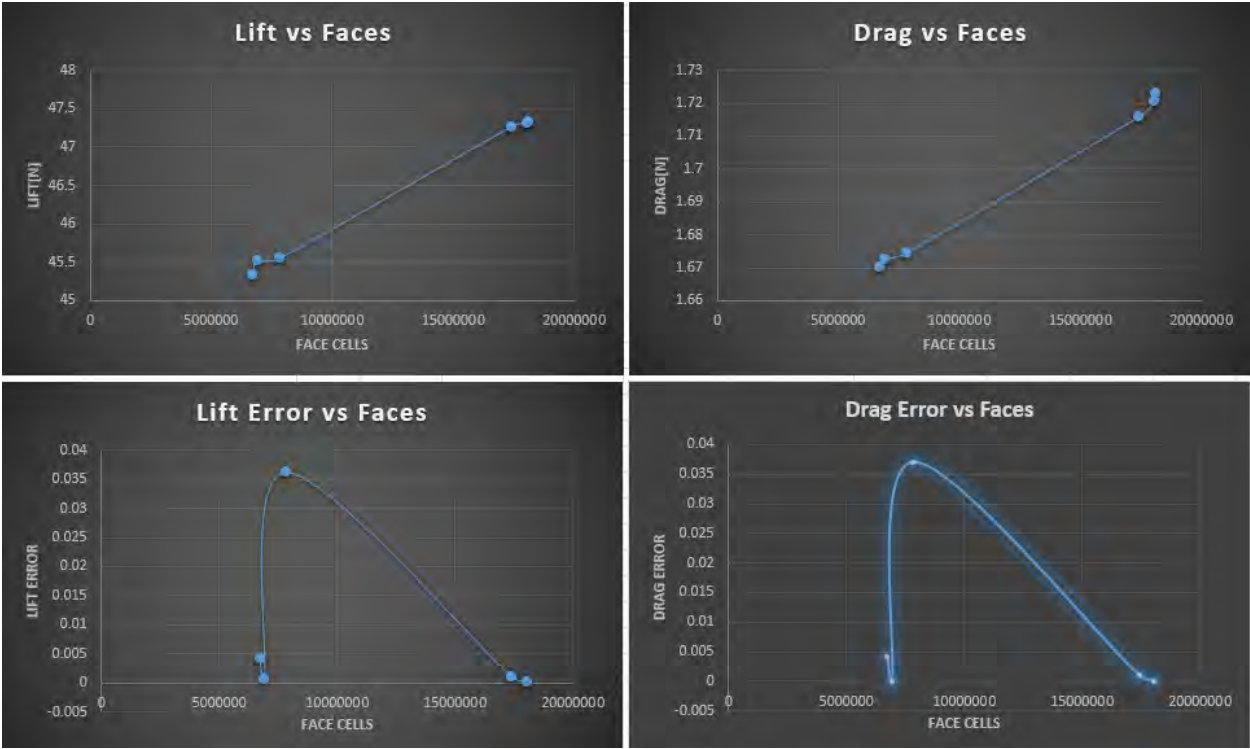
Figure 4-21: Lift and Drag vs Volume and Face Cells Size

When plotting the relative error of a function having the exact solution using a stable scheme we can observe that the function follows a constant increase or decrease path towards zero (for the relative error) even if the error fluctuates around the path. This is a healthy way of reducing the relative error without convergence issues. In our case though the relative error is calculated based on the current value of the function and therefore we can observe this huge peak in the diagrams. On the other hand, the lift and drag diagrams have no such issue since the greater the mesh resolution the closer we get to the mesh independent solution and in a very linear way.
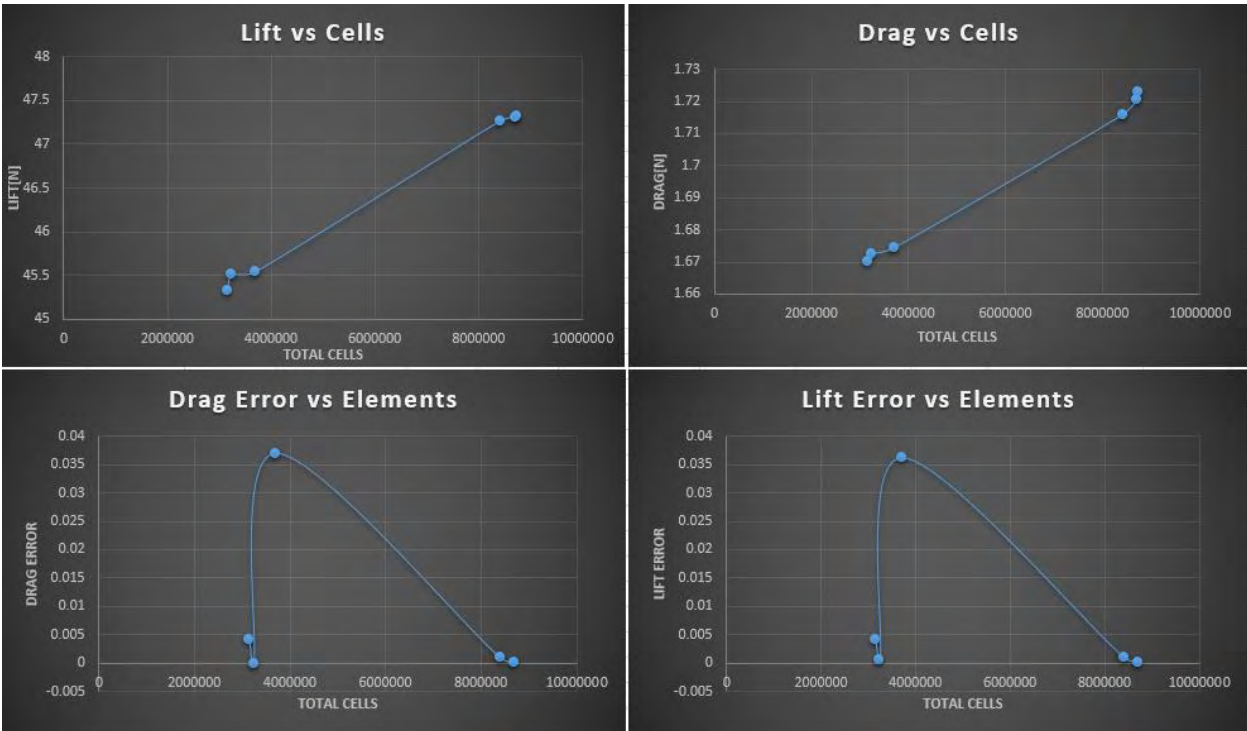
Figure 4-22: Lift and Drag vs Volume and Volume Cells Size

4.1.5. Results

After calculating the effect of the mesh cell and face size we can chose our mesh characteristics having in mind that the solutions that will be acquired will have the desired, for our project, precision and further more we will reduce the overall calculation time that is need in order to get the aero data for the PSU wing that can later on be used in dynamic simulation analysis. The mesh characteristics are the ones of the 4rth setup as can be seen in the figures 21 and 22 respectively. The same setup will also be used for any simulation including the whole uav model.

case	Max size	Min Size	Element size	Mesh Criteria			cells	faces	nodes
				Body Sizing	Face sizing	curvature angle			
4	150	1	100	40	20	12	8401496	17420789	1843661

Figure 4-23: Final mesh characteristics

The simulation process includes the calculation of the aerodynamic behavior of the PSU wing with Chord Length C=30cm and Span b=6meters for angle of attack that ranges from 3 degrees up to 11 degrees and for 4 different velocities 10,12,14 and 16 meters per second. Our scope is to find the optimal setup for the longest flight range. The XFLR5 simulations predispose us the range of those angles of attack and the different velocity inputs. It is obvious that it is not recommended to do arbitrary calculations without having a plan in mind. The aerodynamic criteria that were set in order to find the optimal within our flight range setup indicate that we need to calculate some variables that they indicate the aerodynamic efficiency of the wing and by extension the efficiency of the airplane as well. Of course the flow around the fuselage and the wing do intervene but this will be taken into consideration during the fuselage design stage. By intuition we can feel that increasing the angle of attack and decreasing the flying speed we can achieve the same lift along with a slight increase in the drag. But how do we decide what angle shall we place our wings in order to maximize endurance? In most bibliography and papers there is a trend to use the $\frac{Cd}{Cl^{\frac{3}{2}}}$ ratio because as we did proved this minimizes the power losses. We decided to follow a more direct criterion which is the total drag power that is consumed from the uav.

The drag power can be calculated as follows:

$$Drag\ Power = (Drag\ Force) \times (Velocity)$$

$$D_P = \frac{1}{2}C_D\rho A u^2 \times u = \frac{1}{2}C_D\rho A u^3$$

To begin with the typical diagrams for an arbitrary airfoil or a wing will have three sections. The constant slope section the peak section where the stall occurs and the post stall section as was mentioned in the beginning of the chapter. The polar diagram is a diagram where the lift coefficient is expressed as a function of the drag coefficient. The plot in first sight might be confusing but more plots in the same diagram give us a comparison between the given airfoils or wings. For example, if we translate the plot upwards then for the same Cd we get the same Cl which represents a better flow manipulation of our geometry for the same Cd coefficient. While on the other hand transforming the plot towards the x axis the Cd increases while the Cl stays constant which means poorer manipulation of the flow around our object. We can also extract some values like the highest Cl to Cd ratio and the zero lift angle of attack from the diagram. The zero lift angle of attack point is where the diagram meets the x axis while to get the maximum Cl to Cl ratio we have to calculate the slope of the line that passes from the origin and is tangential in the polar. All this information can be shown below.
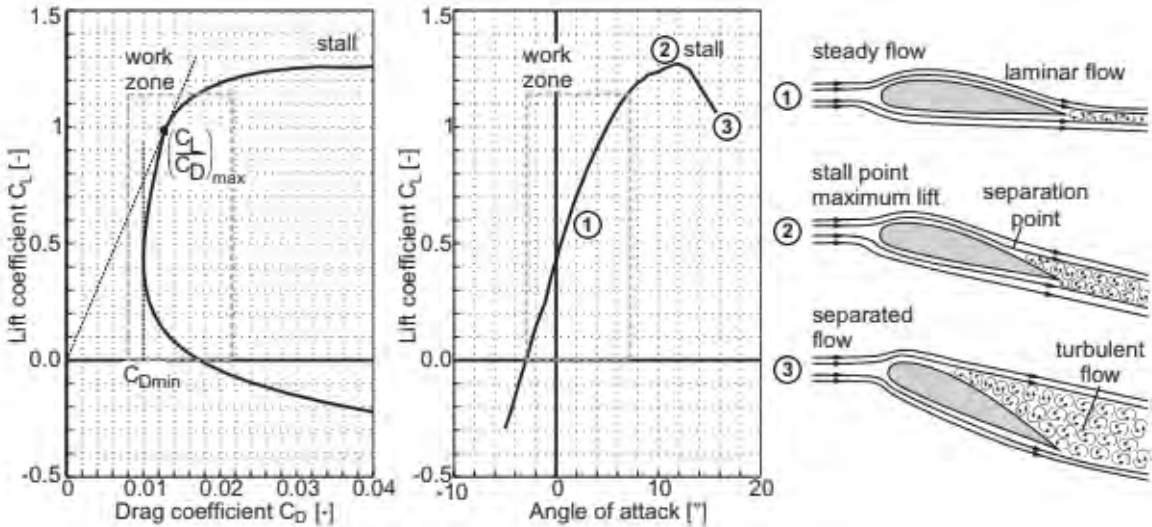
Figure 4-24: Indicated polar diagram with flow type

All the graphs that follow can describe the aerodynamic behavior of our wing within the velocity and angle range that was given during the simulation process. One can also calculate the aerodynamic coefficients or the lift and drag forces of the wing by interpolating the values that are already calculated and get the desired values.
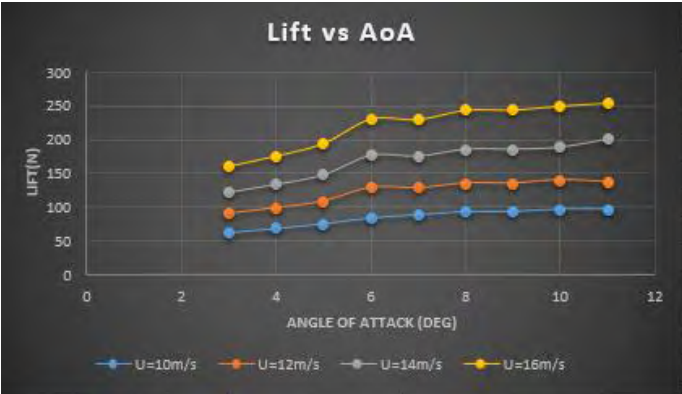
Figure 4-25: PSU Lift vs AoA for different speed values
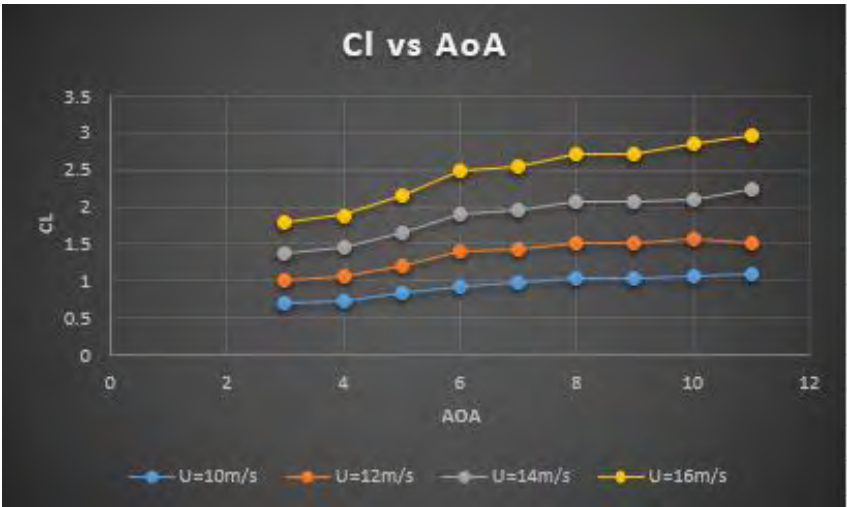
Figure 4-26: PSU Lift vs AoA for different speed values

When the speed and by extension the Reynolds number increases we can expect an increase in the lift coefficient value since the circulation will increase and thus the flow transition point from laminar to turbulent will delay to appear on the airfoil and thus increasing the total lift that can be generated. This can also be achieved by increasing the thickness of the airfoil. Greater thickness will increase the u⁺ (the velocity on the upper wing section) and thus again the transition point will be aft the previous one. One more important aspect of the PSU choice is the linear section of the lift and as shown below drag amplitude in the area of 3-5 degrees. This will not alter neither the total amount of power that is consumed for small angle of attack fluctuations nor its lift that is produced decreasing the oscillations while midair.
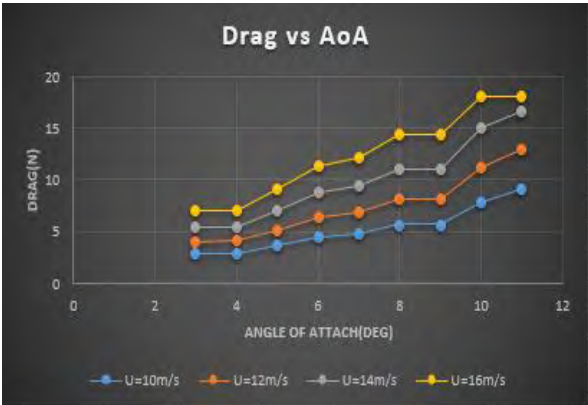
Figure 4-27: PSU Drag vs Angle of attack
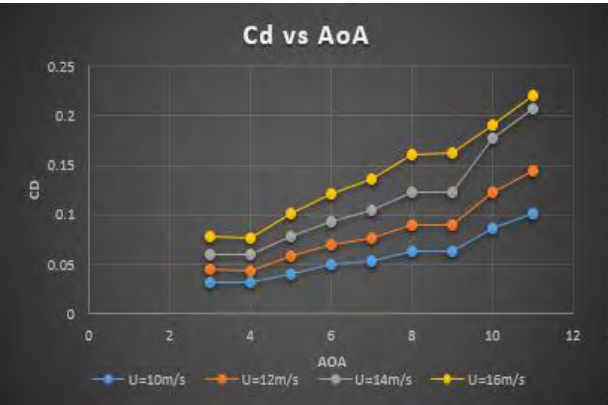
Figure 4-28 :PSU Cd vs Angle of attack

Efficiency is the most desirable aspect of our geometry especially for a MALE (medium altitude long endurance) uav. The two variables that describe the efficiency of an object that is moving inside a fluid are the:

$$\frac{C_l}{C_d}$$

And the term:

$$\frac{C_d}{C_l^{\frac{3}{2}}}$$

The second term is not something that can be intuitively understood but was extracted by minimum power consumption criterion in chapter 3.2
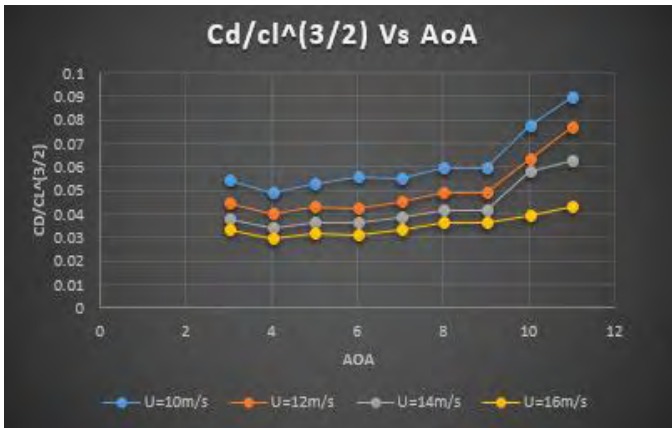
Figure 4-30 PSU minimum power efficiency factor
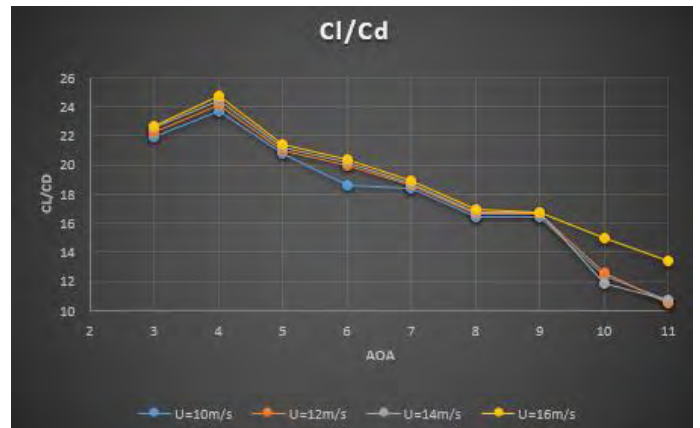
Figure 4-29 PSU Cl to Cd ratio

Finally, the most direct endurance criterion of an object is the power consumption itself. It was calculated based on the drag force and the velocity of the flight and lets no space for misunderstanding and misleading on what is the optimal setup of the geometrical variables that we need to be defined. It can also be used as an optimization criterion.
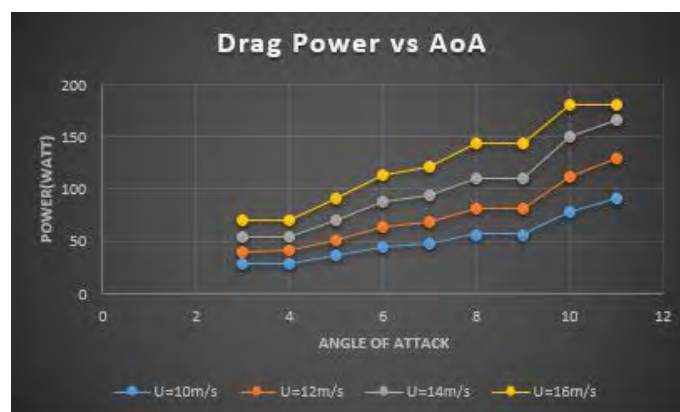
Figure 4-31: Drag Power vs AoA

It is obvious that increasing the angle of attack of a wing then the drag increases since the vector of the total force is pointing more backwards and thus the component of the drag is greater, what we are interested in this graph is the behavior of the power consumption at a given speed for a range of angles like previously. The more constant the power consumption then the more accurate predictions we can make for the average consumption of the wing since it does not have a constant angle of attack but it fluctuated throughout the flight. But the selection of the desired u_{flight} which is the speed that the glider will fly and the angle of attack of the main wing can be done by looking the next graph.
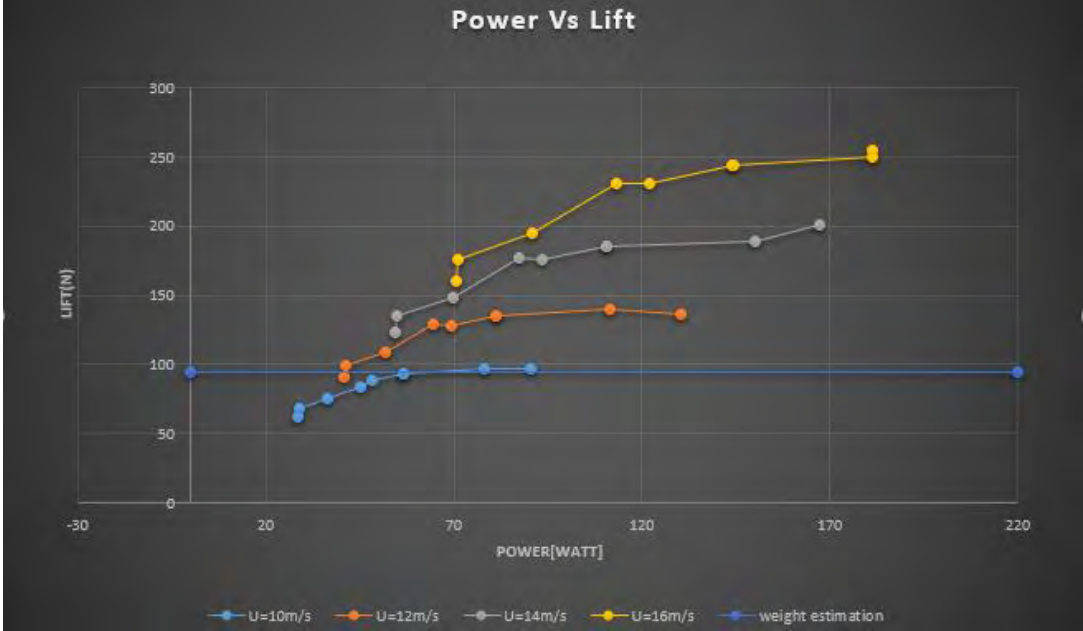
Figure 4-32: PSU drag power consumption

The horizontal axis of the graph indicates the power consumption while on the y axis we can see the total amount of lift that can be produced while we spent the equivalent x axis power. The blue horizontal line indicates the estimated weight that was calculated during the weight estimation process. Thus all the points that are above the line are points where the lift produced can lift the weight of the plane and thus the plane flies or accelerates while the points below the line represent the points where the lift is less than the weight and the uav starts to decelerate and decent. We want to pick the point that is borderline above the weight estimation line and has the fewest consumption of drag power. The point of minimum power that can produce adequate lift is the 2nd point of the orange curve. Which is at 3.5 degrees

angle of attack and 12 m/s flying speed. Thus, this will be the target flying speed and the angle that the wing placement angle.

4.2. 3D Wing Design

In the introduction in this chapter there was a short representation of the most wing geometrical parameters and values that define its geometry. Now the whole simulation process was done only by altering the velocity and the angle of attack of the given PSU wing and no alter in its shape took place. The factors that can alter its geometry are the taper ratio, the twist of the wing, the dihedral angle, the swept ratio and the placement or not of winglets in the ends of the wings. Of course, the changes that we will make have no arbitrary character but the purpose of them is to ensure that the flow around the wing is the closest to the optimal.

4.2.1. Elliptic Distribution

As can be seen the figure 33 shows the distribution of section lift coefficients, C_l, along the span of some arbitrary wing planform. The figure shows the frontal view of a cantilevered wing (the left wing is shown, looking toward the leading-edge). The plane of symmetry (left) is where the wing root would be located and the right side is the left wingtip. The figure 34 shows two kinds of distribution of C_l. The first can be considered an ideal span wise distribution, which would be achieved if the laws of physics didn't require the lift to gradually go to zero at the wingtip. This distribution would result in each span wise station contributing uniformly to the total lift coefficient. As a consequence, it would require the least amount of AoA at any given airspeed to maintain altitude. And the less the AoA, the less is the generation of lift-induced drag.
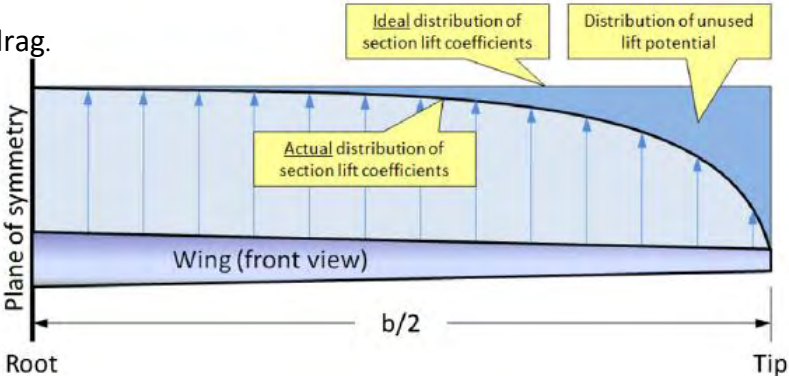
Figure 4-33 : Elliptical vs Rectangular Cl distribution
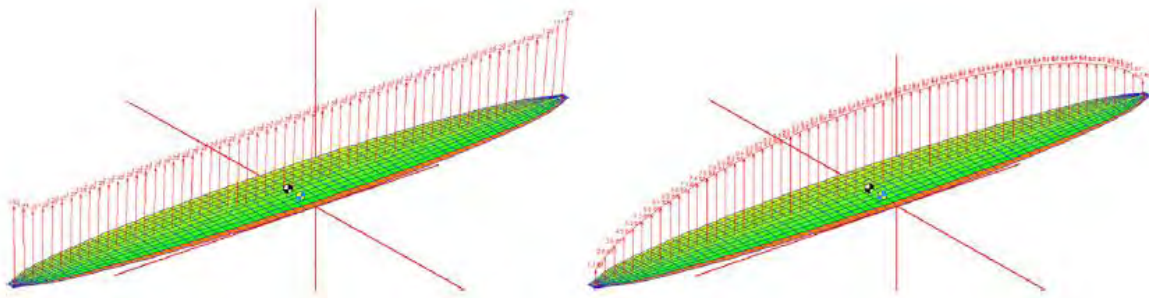
Figure 4-34: Elliptical vs Uniform Lift Distribution

4.2.2. Wing Parameters

A way to achieve the elliptical wing distribution is to create a wing with an elliptical span wise chord distribution. Another way of achieving this distribution is by altering the shape even the profile of the airfoil when reaching the wingtip. In order for the wing to generate the same amount of lift we can place the profile of the airfoil closer to the fuselage in a higher angle of attack. That way we change the lift distribution and we reduce some lift from the tip of the wing, and we add it closer to the fuselage. One drawback of this is that the stall will start to occur closer to the fuselage since the airfoil there will be placed in higher angle of attack. But it is the only way as long as the wing must retain its chord for two rows of solar panels to be fitted.

The analysis began with the initial orthogonal shaped wing. The wing has been designed in the XFLR5, putting the parameters such as (0.3m) chord, (6m) span and zero sweep, dihedral and wing twist, as seen below.
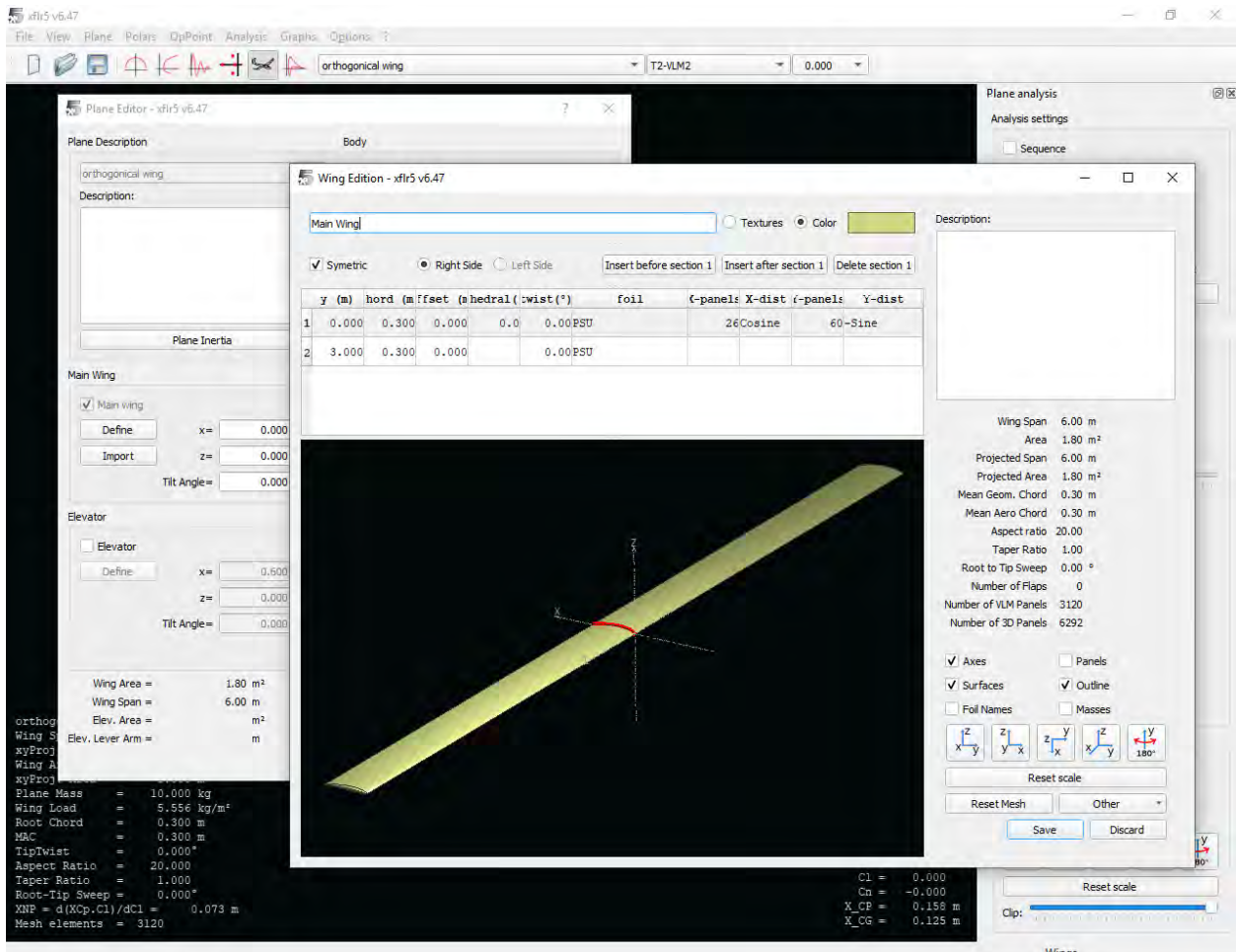
Figure 4-35: Wing Design

After designing the wing, the first step is to select the polar type of the analysis. By selecting Fixed Lift analysis, the code calculates the speed and the other aerodynamic coefficients for a fixed value of lift, making it easy for the comparison after a change in geometry through the optimal solution. The Vortice Lattice Method (VLM2) has been used as it is the most accurate method and the only one that considers viscous forces. The mass of the airplane was inputted 10 kilograms, as it initially calculated.
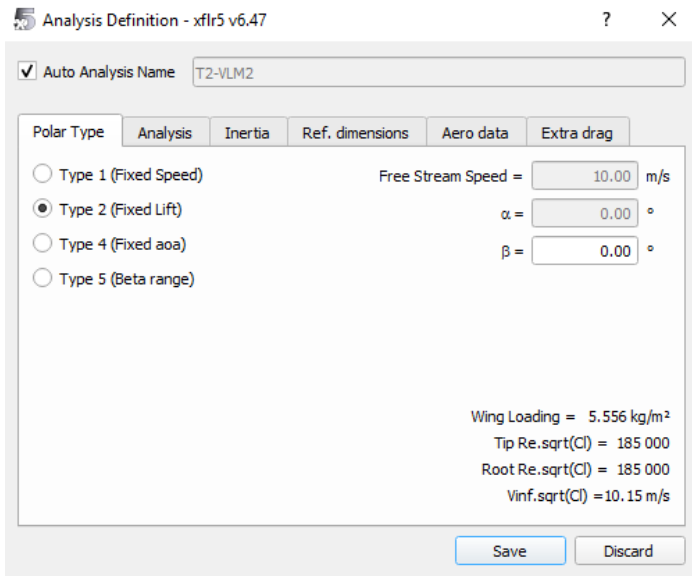
Figure 4-36: Polar type
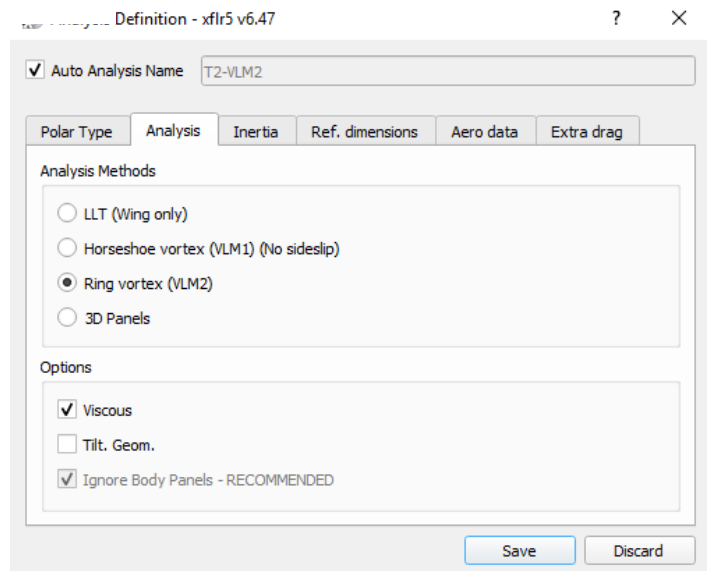
Figure 4-37: Analysis method
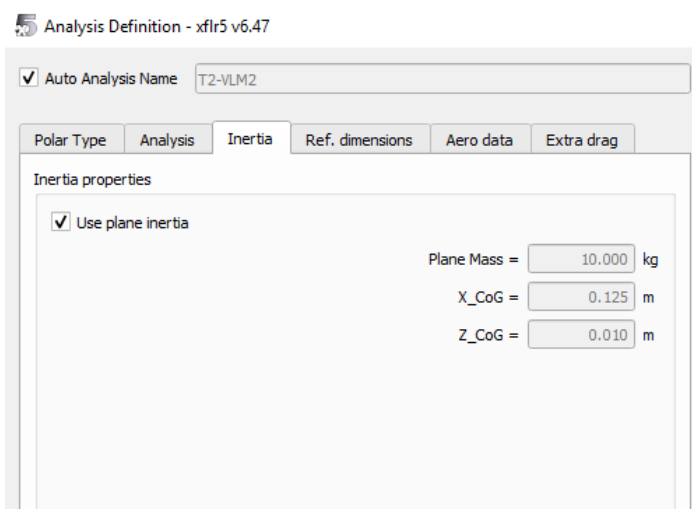
Figure 4-39: Mass selection of the airplane

The span wise lift distribution of the orthogonal shaped wing, as seen below, was far from an elliptical distribution, so we tried reducing lift from the tips of the wing by putting a symmetric airfoil as the last section of the wing, in zero angle of attack.
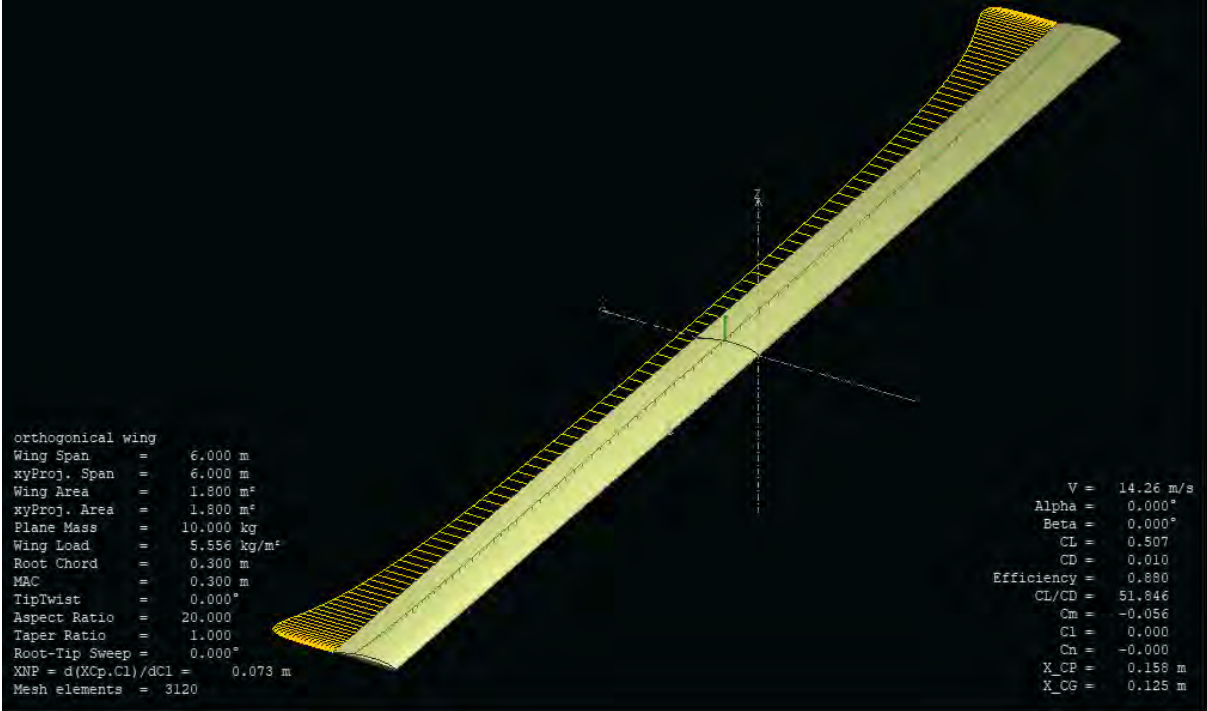
Figure 4-40: Orthogonal Shaped Wing & Induced Drag Distribution
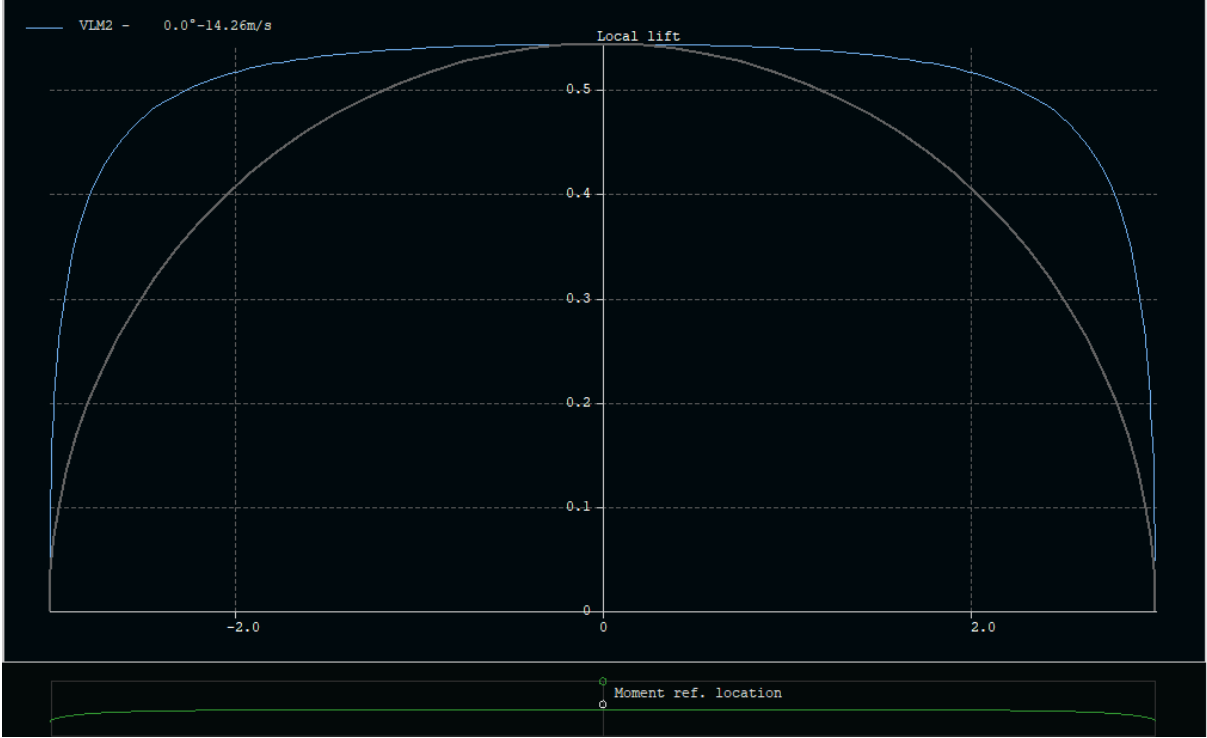
Figure 4-41: Orthogonal Wing, Lift Distribution

The outcome of the next run is better and the induced drag is reduced due to reducing of wing tip vortices. The procedure that was followed afterwards was a sequence of changing the twist of the wing in the points that the lift needed reduction, until the target curve is achieved.
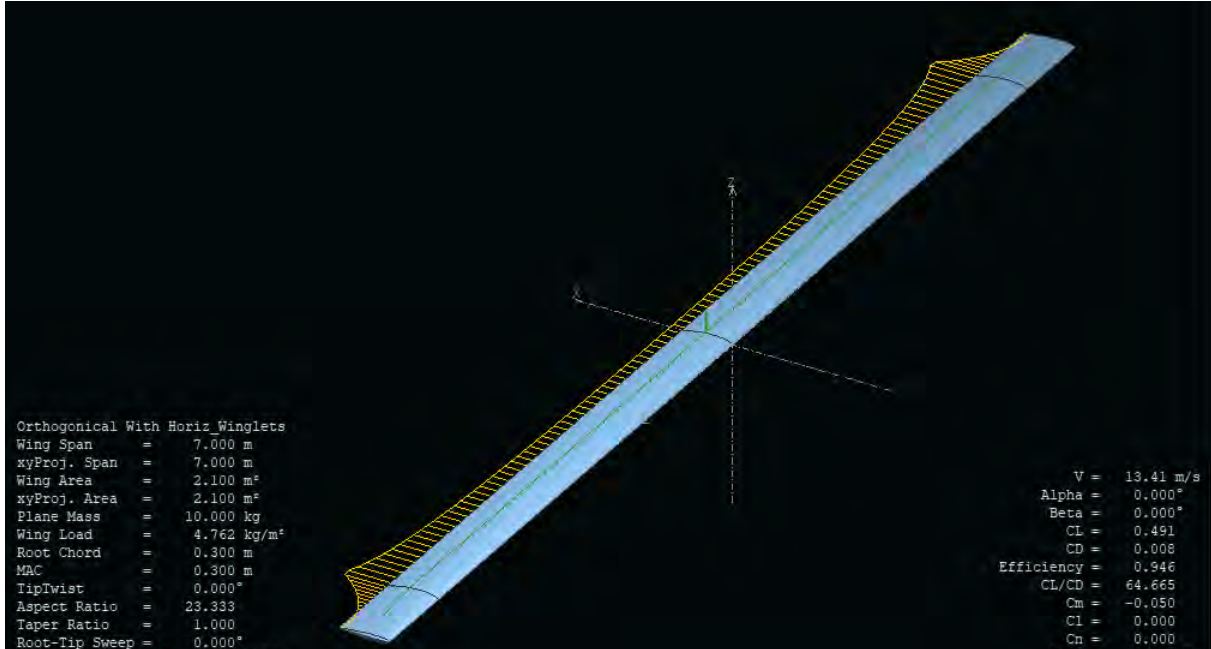
Figure 4-43: Orthogonal Wing With Horizontal Winglets
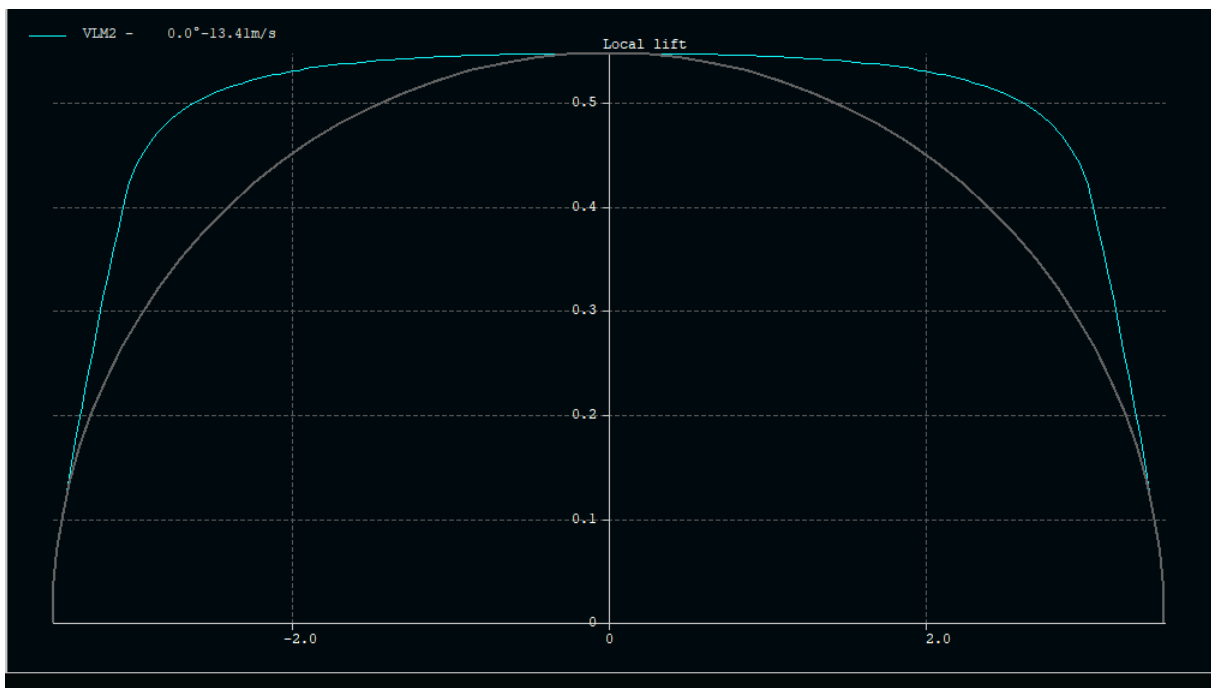
Figure 4-42: Orthogonal Wing With Horizontal Winglets, Lift Distribution
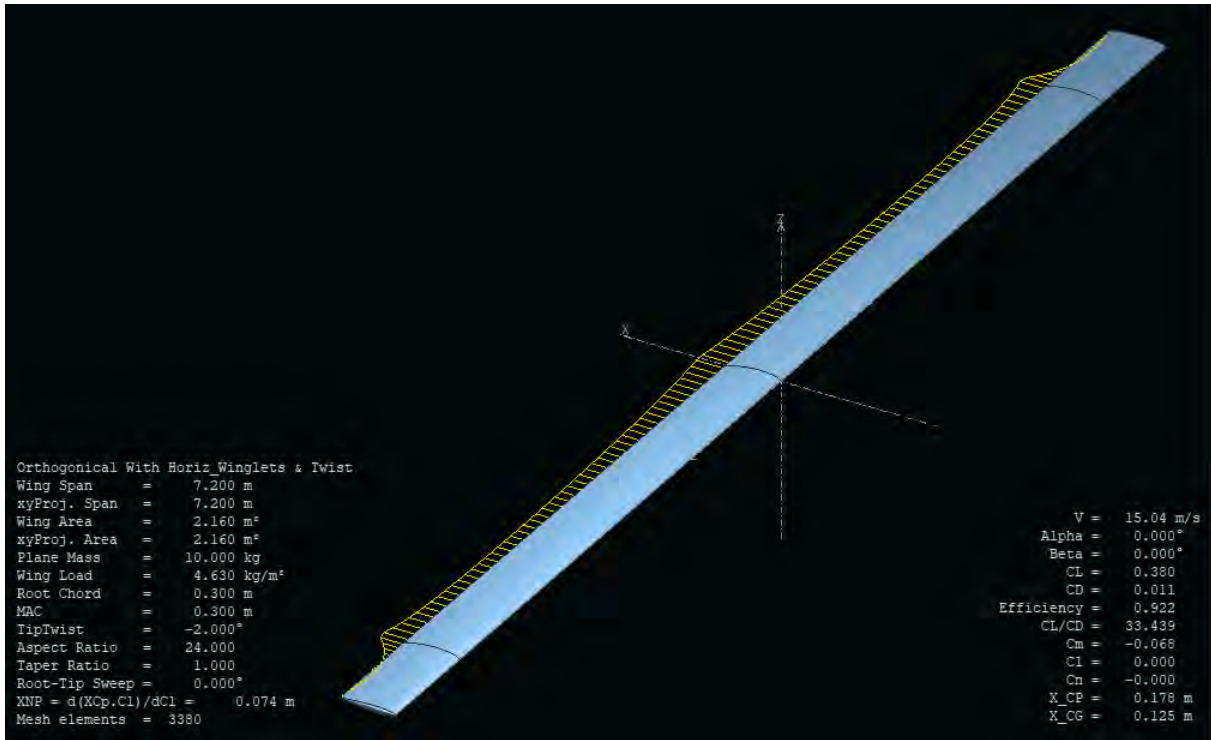
Figure 4-45: Orthogonal Wing With Horizontal Winglets & Twist
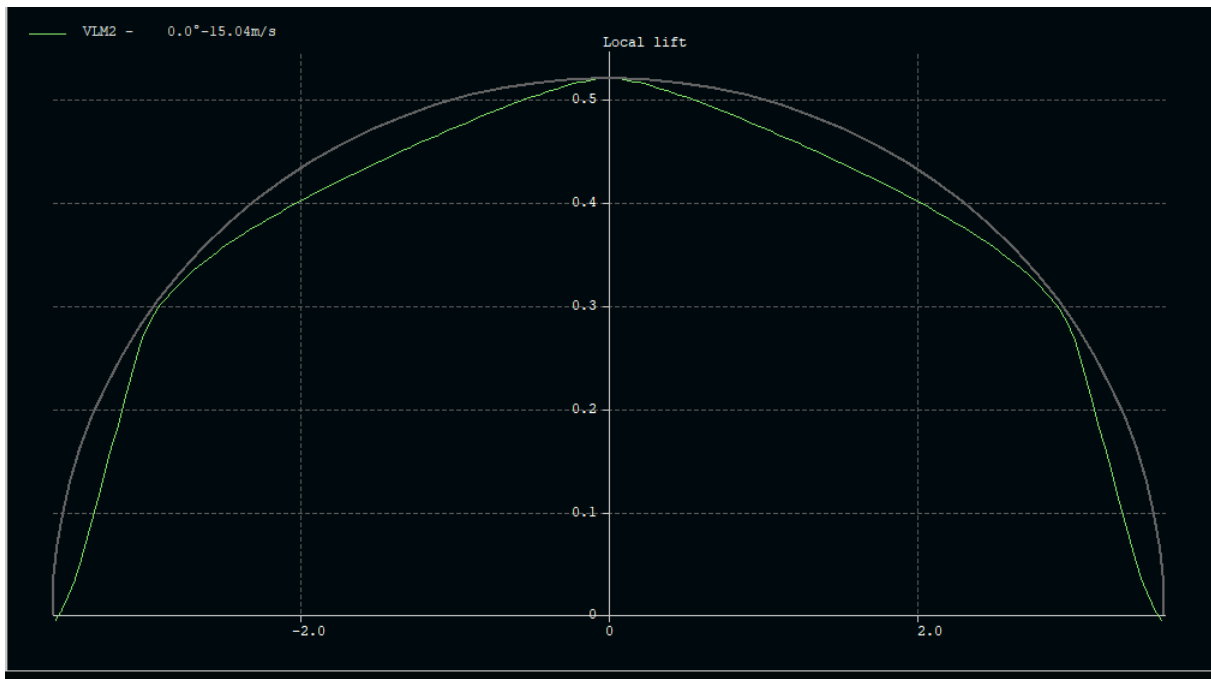
Figure 4-44: Orthogonal Wing With Horizontal Winglets & Twist, Lift Distribution
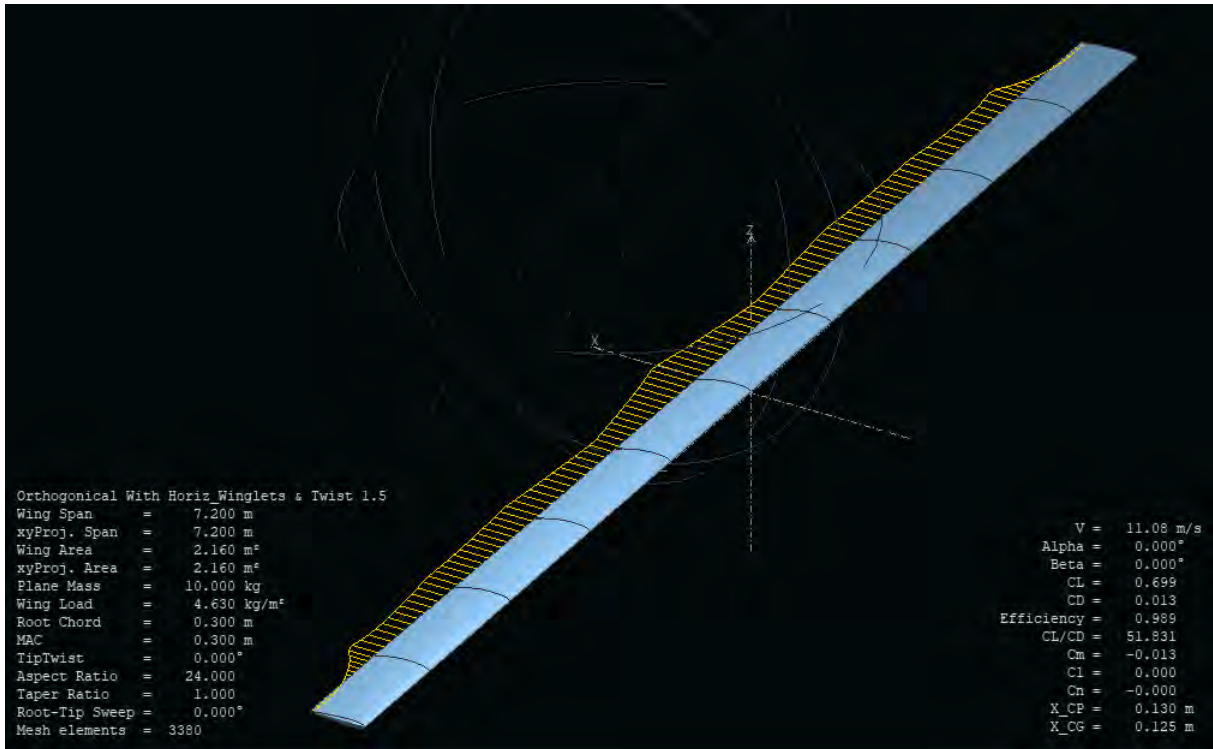
Figure 4-46: Orthogonal Wing With Horizontal Winglets & Twist, version II
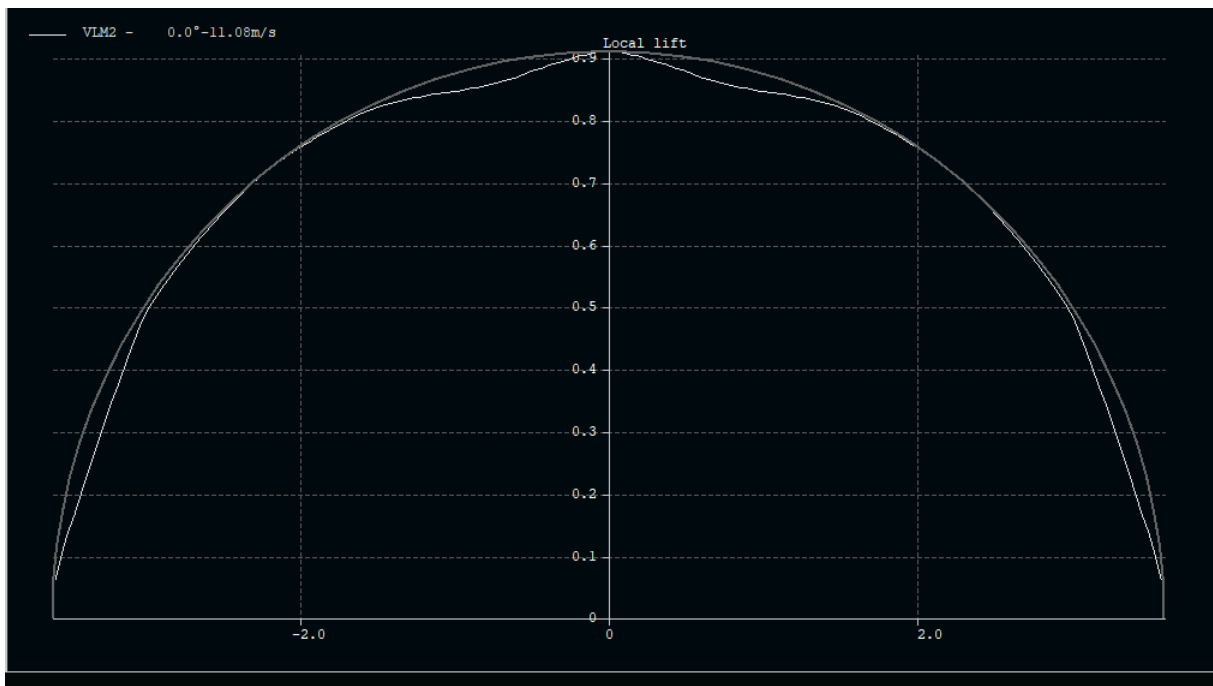
Figure 4-47: Orthogonal Wing With Horizontal Winglets & Twist, version II, Lift Distribution

```
Orthogonical With Horiz_Winglets & Twist 1.5.3
Wing Span       =     7.000 m
xyProj. Span    =     7.000 m
Wing Area       =     2.100 m²
xyProj. Area    =     2.100 m²
Plane Mass      =    10.000 kg
Wing Load       =     4.762 kg/m²
Root Chord      =     0.300 m
MAC             =     0.300 m
TipTwist        =     0.000°
Aspect Ratio    =    23.333
Taper Ratio     =     1.000
Root-Tip Sweep  =     0.000°
Mesh elements   =     8112
```

```
V          =   10.97 m/s
Alpha      =    0.000°
Beta       =    0.000°
CL         =    0.734
CD         =    0.015
Efficiency =    0.999
CL/CD      =   49.204
Cm         =   -0.006
Cl         =    0.000
Cn         =   -0.000
X_CP       =    0.127 m
X_CG       =    0.125 m
```

Figure 4-48: Orthogonal Wing With Horizontal Winglets & Twist, version III
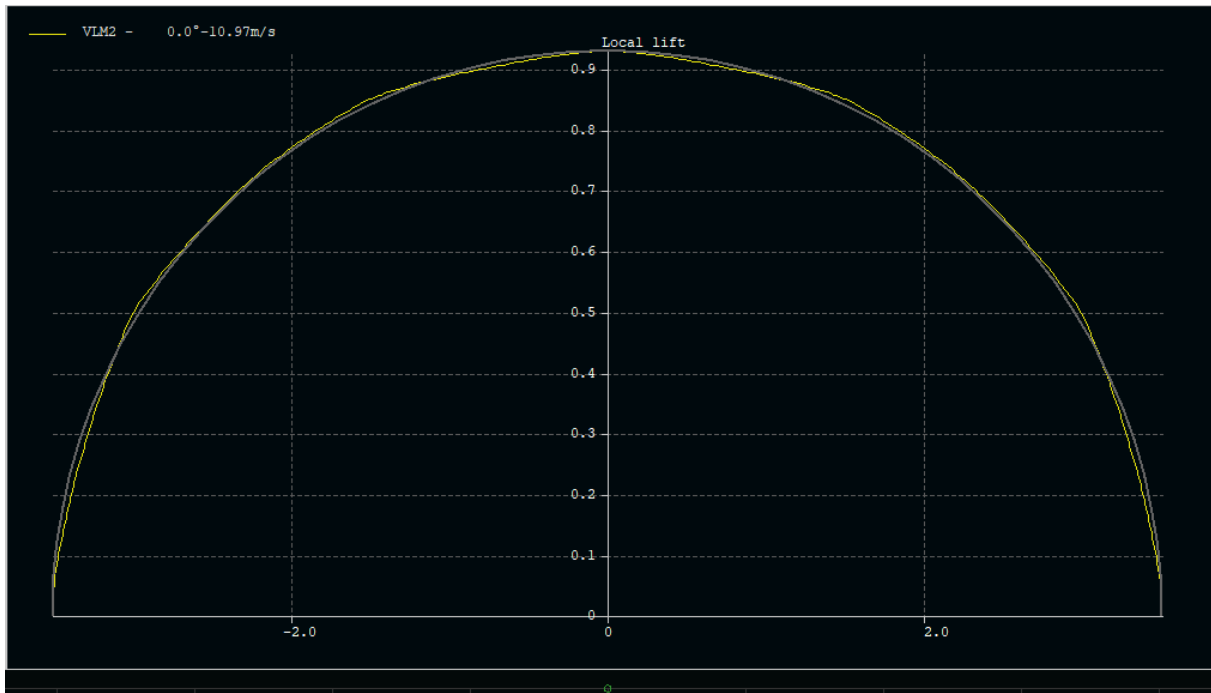
Figure 4-49: Orthogonal Wing With Horizontal Winglets & Twist, version III, Lift Distribution

Chapter5: Fuselage

Fuselage is the central portion of the body of an airplane, designed to accommodate the crew, passengers, and cargo. It varies greatly in design and size according to the function of the aircraft. In a jet fighter the fuselage consists of a cockpit large enough only for the controls and pilot, but in a jet airliner it includes a much larger cockpit as well as a cabin that has separate decks for passengers and cargo. The fuselage also serves to position control and stabilization surfaces in specific relationships to lifting surfaces, which is required for aircraft stability and manoeuvrability.

Once having decided the airfoil profile as well as the parameters of the wing we obtained the lift generating device. So one of the major fuselage purpose use is to provide adequate rigidity so that it can withstand the static and dynamic loads during the flight and in our case to house all the electrical components needed in order for the UAV to flight in a controllable manner. Before analysing the geometry and the type of the fuselage we have to take into consideration some aspects and features that our plane requires. The major ones are:

- Fineness ratio to avoid large pressure gradients and flow separation
- Ease of removing and replacing electrical components
- Rigidity
- Streamlined design for low drag generation and moment balancing
- Proper wing placement so that COG is aft of the COP
- Do not obstruct the folding of the propeller blades

The aircraft fineness ratios are defined as length divided by diameter, which including nose fineness ratios and tail cone fineness ratios. In all of the following nose cone shape equations L is the overall length of the nose cone and R is the radius of the base of the nose cone. Y is the radius at any point x, as x varies from 0, at the tip of the nose cone, to L. The equations define the 2-dimensional profile of the nose shape. The full body of revolution of the nose cone is formed by rotating the profile around the centerline (C/L). Note that the equations describe the 'perfect' shape practical nose cones are often blunted or truncated for

manufacturing or aerodynamic reasons. The shapes are defined by the function that describes the perimeter of the cone and it is up to your imagination what kind of function you will use.
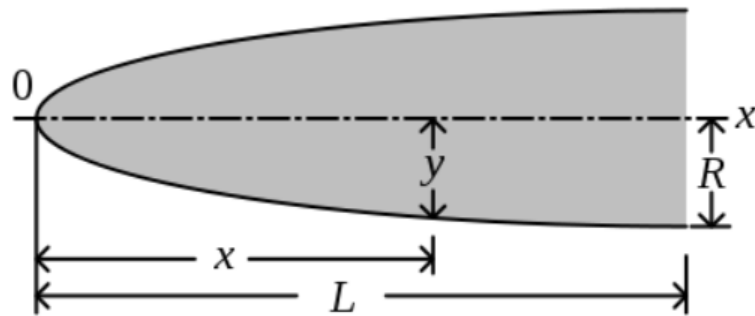
Figure 5-1: 2D fuselage section

Then the 3D part is produced by revolving the upper sketch around its symmetry axis. There are typical shapes that someone can use as an initial design like: 3/4 Power, Cone, 1/2 Power, Tangent ogive, parabolic, ellipsoid, etc. Liu Tang-hong, Tian Hong-qi and Wang Cheng-yao (2006) wrote in journal "Aerodynamic performance comparison of several kind of nose shapes" that as speed of the plane increases, the drag coefficient increase as well. Different type of fuselage shape can give different drag coefficient as well. But as shown below, at flying speeds lower than 0.5 Mach fuselage shape have zero impact in overall drag production.

5.1. Fuselage Types

5.1.1. The Frustum Fuselage

The frustum fuselage is used to describe a fuselage whose empennage is effectively shaped like a frustum or a trapezoidal prism. An example is shown in the picture below. The pros of this kind of fuselage is the inexpensive construction and the compact-small size fuselage. Although that kind of fuselage has low aerodynamic efficiency compared to the tadpole one.

Figure 5-2: Frustum fuselage type

5.1.2. The Pressure Tube Fuselage

The look of that fuselage is pretty familiar since the most of the passenger airplanes are designed like this. It consists of three parts the two capped sections in the front and the rear of the airplane and a cigar like cylinder in the middle. The circular middle section is ideal for carrying pressure loads and therefore is used in high altitude avionics. One drawback is that the huge diameter of the fuselage as well as the sloped aft (so that it does not touch the ground during take-off) is that they create turbulent wake decreasing the effectiveness of the rudder. Ways to avoid this phenomenon is to add a dorsal or vertical fin between the fuselage
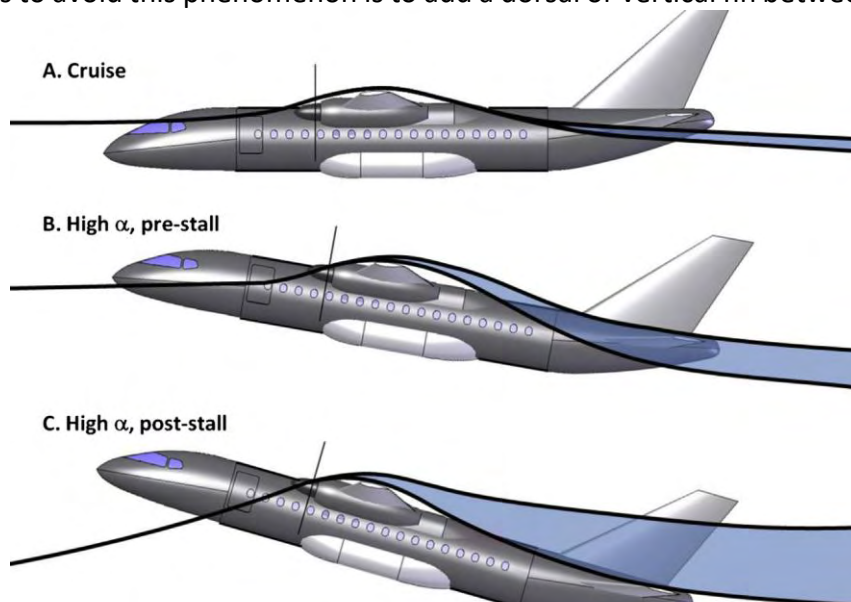
Figure 5-3: Pressure Tube Fuselage Vs Angle of Attack

and the rudder but since this type is not appropriate for our purpose no further analysis will take place.

5.1.3. Tadpole Fuselage

As the name of this fuselage implies the shape of it is similar to a tadpole. It consists of an ellipsoidal cabin in the front a lofted lever to connect the fuselage with the empennage, the wings and the empennage itself. Tadpole fuselages generate far less drag than the frustum kind for two primary reasons: (1) their forward portion is shaped to sustain laminar boundary layer and (2) their empennage shape results in as much as 30-40% less wetted area, where wetted area is the portion of the control surfaces that are affected from the turbulent wake.
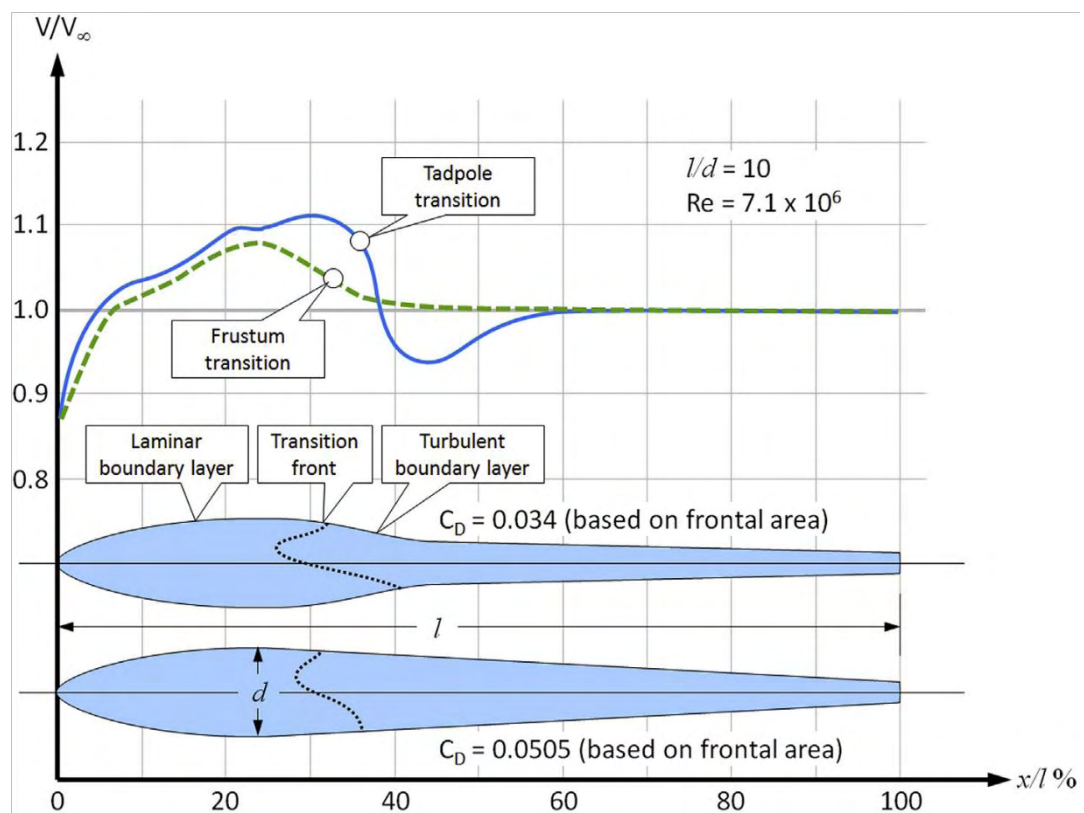
Figure 5-4: Frustum vs Tadpole Fuselage Ref. Althaus D. Motorless Flight Research

In low Reynolds numbers like in our case a big fraction of the total drag is created by the shear stresses in the fuselage circumference and the rest is created from the pressure difference between the rear and the front face of the fuselage. Another aspect of tadpole fuselage design is the downward tilt of the fuselage as shown in the next figure. This is a response to the upwash caused in the airflow ahead of the wing. A straight fuselage will be at a higher angle of incidence and this will increase its drag. To reduce this, the forward portion

of the fuselage is tilted downward to align it with the oncoming airflow, reducing its drag. Some further efficiency increase can be achieved by tilt the tail-boom down or reshape it to better match the flow behind the wing as well.
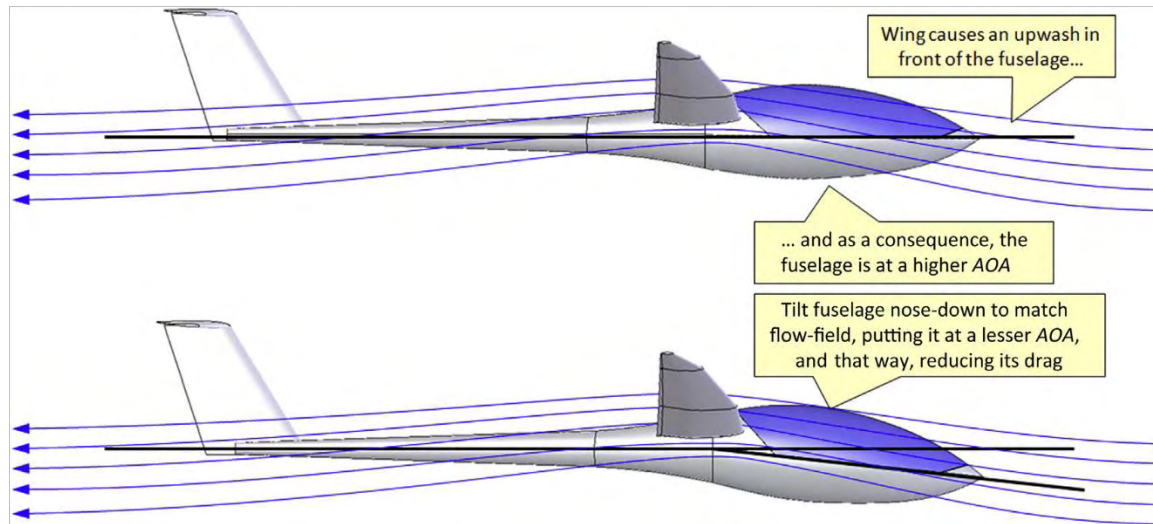
Figure 5-5: Upwash effect in the fuselage

This phenomenon occurs at relatively high velocities which are translated to lower pressure on the upper area of the wings. In our case we have to take into consideration and other aspects before we rework our model like the fact that the upper area of the wings is quite distant from the nosecone of the fuselage and at low Reynolds flights the upwash that is created has not that much of an effect in the overall drag. Furthermore, as it was said in previous chapter in low Reynolds flows a decent amount of drag is caused by the fluid friction. Thus, we can decrease the amplitude of drag by simply making a more compact with smaller surface fuselage.

One more influential aspect of the design, is the wash that the propeller can generate by creating a vortex like rotational wake that will affect the wing that lies right behind it. It is a drawback that all the propeller propulsed aerial vehicles have to deal with, and the most common way to counter its effect is to place the propeller in the rear of the fuselage. This though comes with great disadvantages like the moment that the propeller force produces, does not constitute to self-aligning torque making the whole aircraft more unstable since it not only tends to rotate the construction around the pitch axis and it also leaves dirty air for the ailerons and the ruder making the passive and active control more difficult and the control

surfaces less effective and thus increasing the amount of the energy consumption for the whole stabilization. Finally, we should also mention that in our case the landing of the vehicle will take place by friction in the lower surface of the fuselage and the empennage since the UAV will crawl to stop for some meters. So, if we tilt downward the fuselage then we will create two contact points for the crawling landing and this can become destructive after a while.

5.1.4. Blended Wing Fuselage

A blended wing body (BWB), is a fixed-wing aircraft having no clear dividing line between the wings and the main body of the craft. The aircraft has distinct wing and body structures, which are smoothly blended together with no clear dividing line. This contrasts with a flying wing, which has no distinct fuselage. A BWB design may or may not be tailless.

The main advantage of the BWB is to reduce wetted area and the accompanying form drag associated with a conventional wing-body junction. It may also be given a wide airfoil-shaped body, allowing the entire craft to generate lift and thus reducing the size and drag of the wings.

Figure 5-6: Aircrafts with Embeded Wings

5.2.   Fuselage Design

After the possible concepts were taken into consideration, the geometry of the fuselage has to be designed. The first thing is to design the electronic components assembly in that way so the Center of Gravity will be as far forward as possible and in the aircraft symmetry plane.
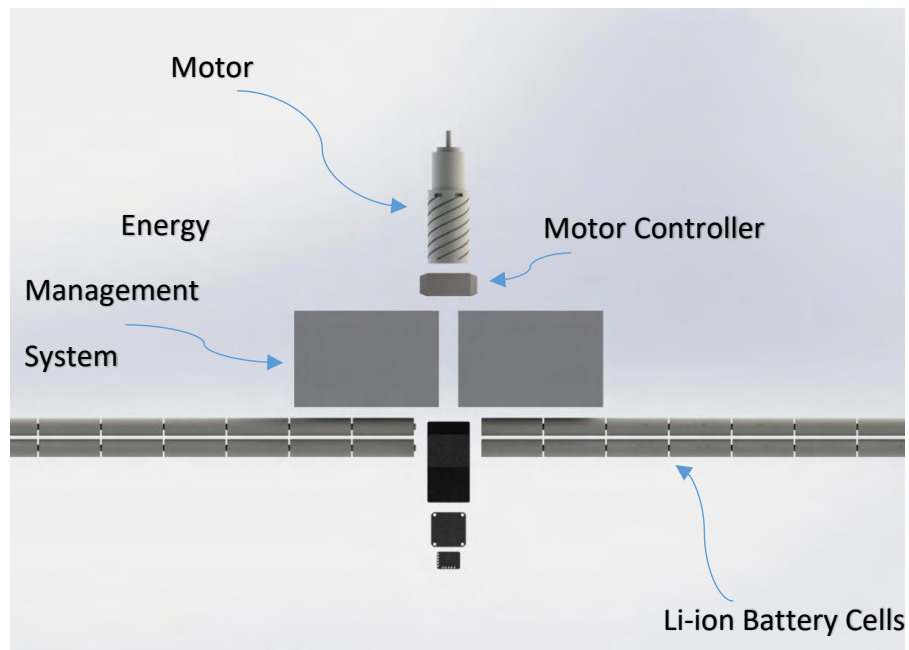
Figure 5-7: Electronics Assembly
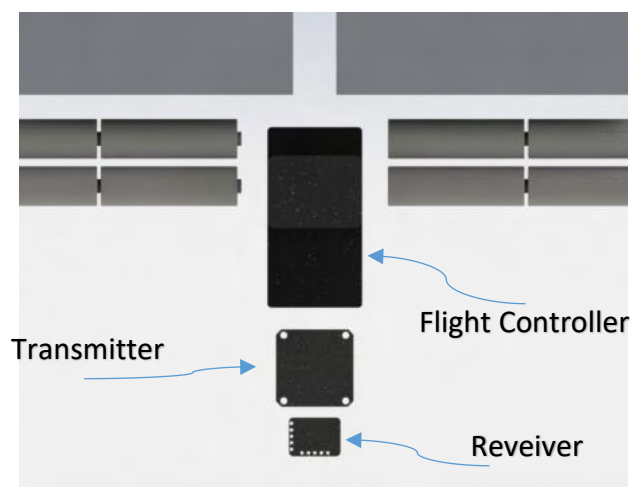
Figure 5-8: Electronics Assembly Zoomed In

So the Li-ion batteries divided in two pairs, each fitted in a wing and the other electronic components have put along the roll axis so the aircraft is balanced. The first concept to be applied is the tadpole shaped fuselage that is efficient and with minimal design since the already designed wing can be attached straight to the fuselage.

The fuselage designed around the electronic components with as less frontal area as possible for minimum aerodynamic drag. Another limitation was that the (600mm) diameter propeller has to be folded in when the motor shuts down. The design process can be shown to the figures below.
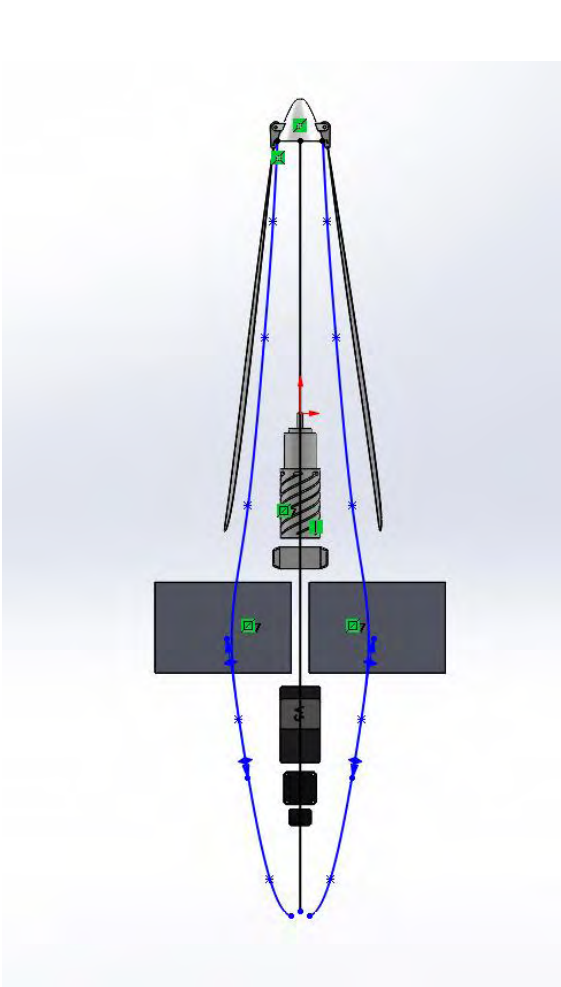
Figure 5-9: Electronics Assembly with Sketched Fuselage Around Them
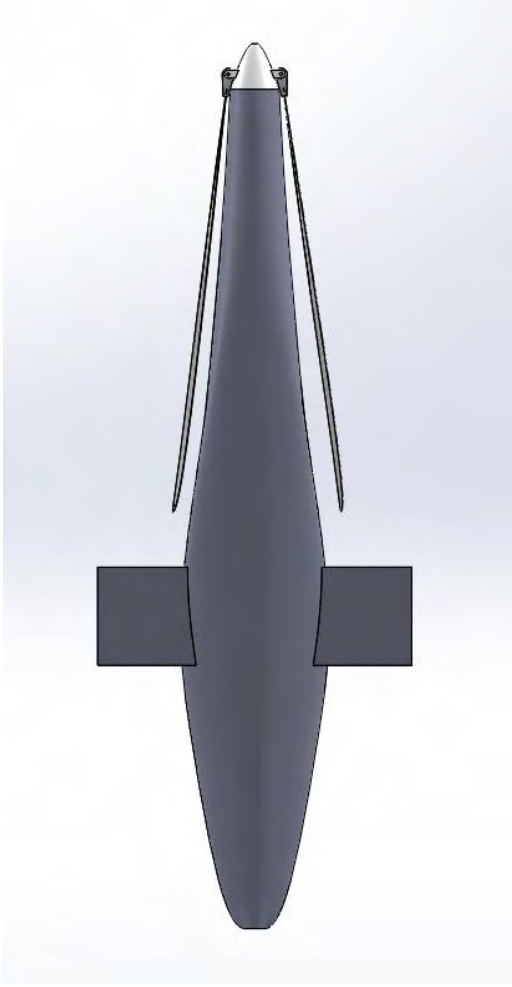
Figure 5-10: Tadpole/Cylindrical Fuselage
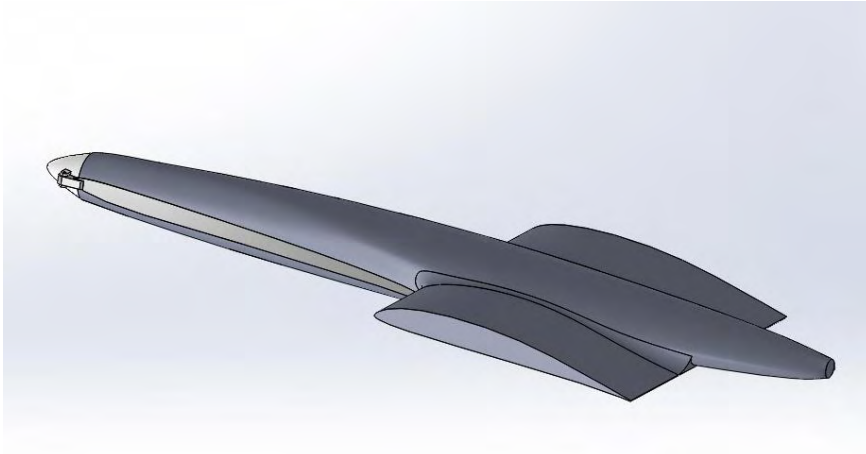
Figure 5-11: Tadpole/Cylindrical Fuselage
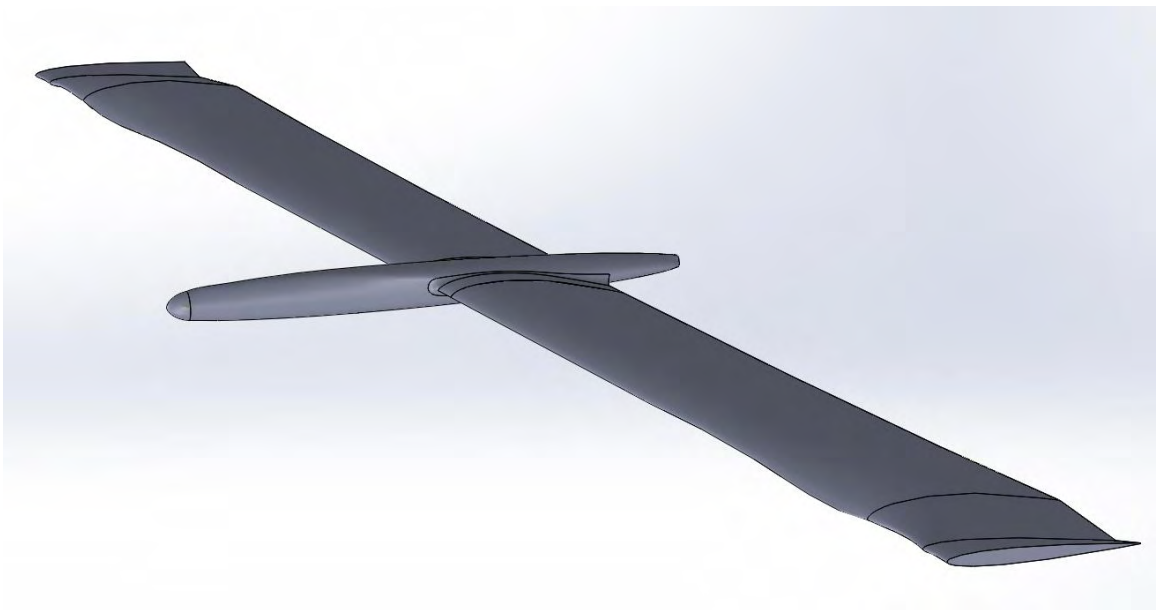
Figure 5-12: Tadpole/Cylindrical Fuselage with Wings Attached

The second concept to be evaluated is the blended wing fuselage geometry. As long as we needed the 0.3m chord for the two solar cell rows to be stacked above each wing and the electronics didn't fit in the 0.3m chord wing, the root chord had to be increased in size. The already designed rectangular shaped wing couldn't fit in our restraints, so we must design a knew one that also flies with elliptical lift distribution through the wingspan.

We started from the rectangular shaped optimized wing and started with increasing the root chord and leaving the tip chord as it was. Tried to achieve an elliptical lift distribution and the results of the procedure are cited below.
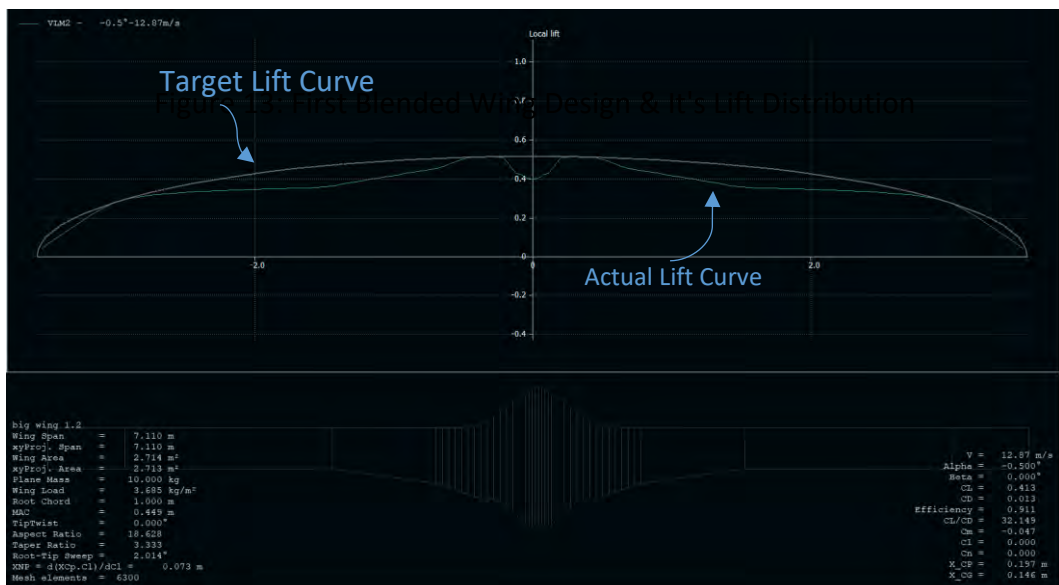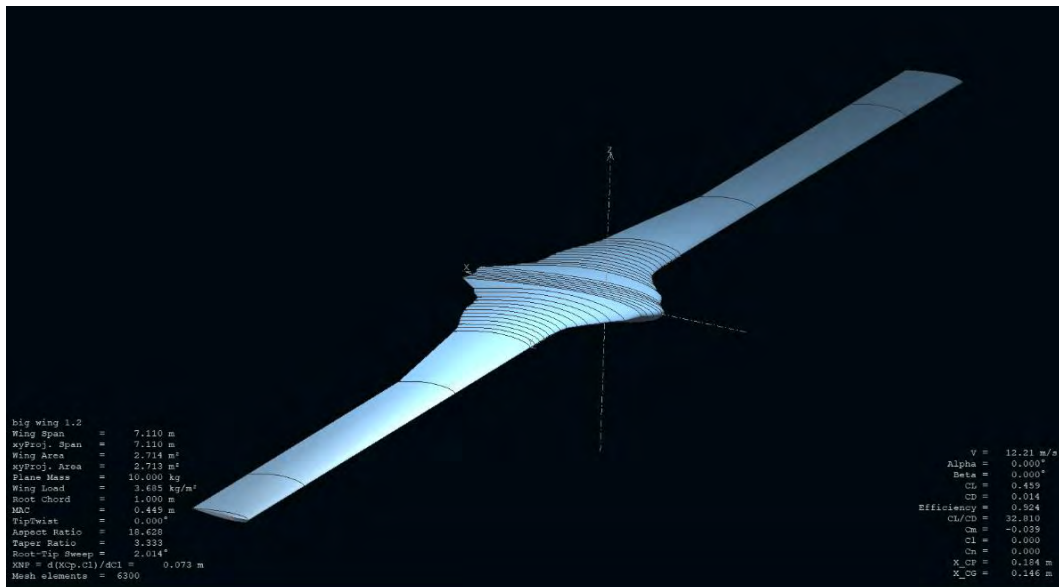
Figure 5-13: First Blended Wing Design & It's Lift Distribution
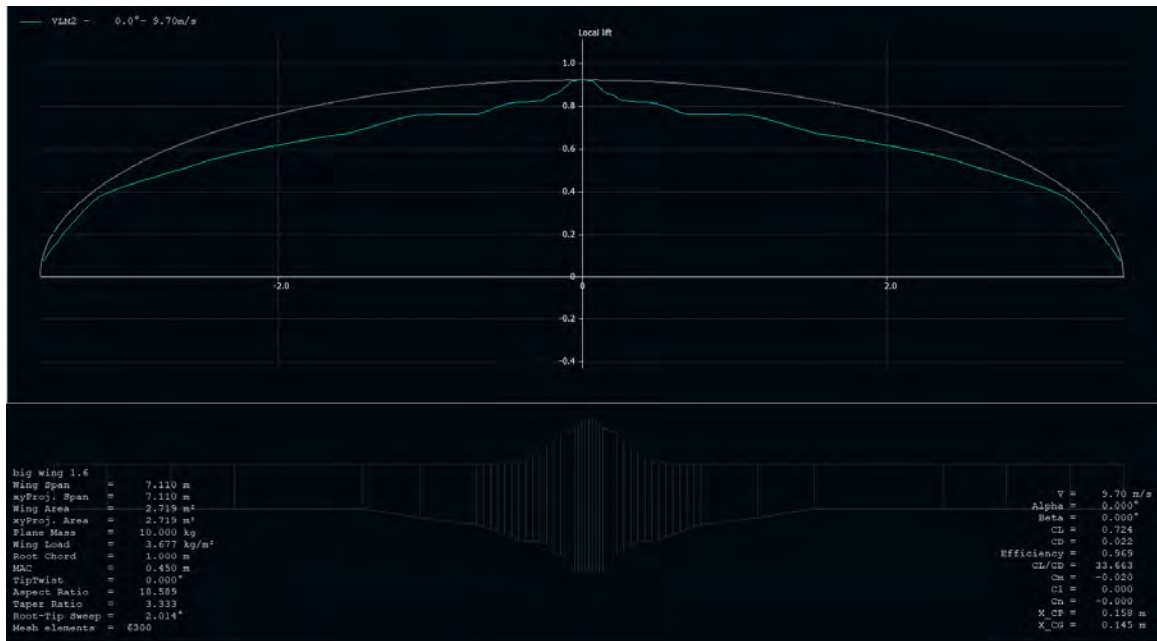
Figure 5-14: 2nd Design Lift Distribution
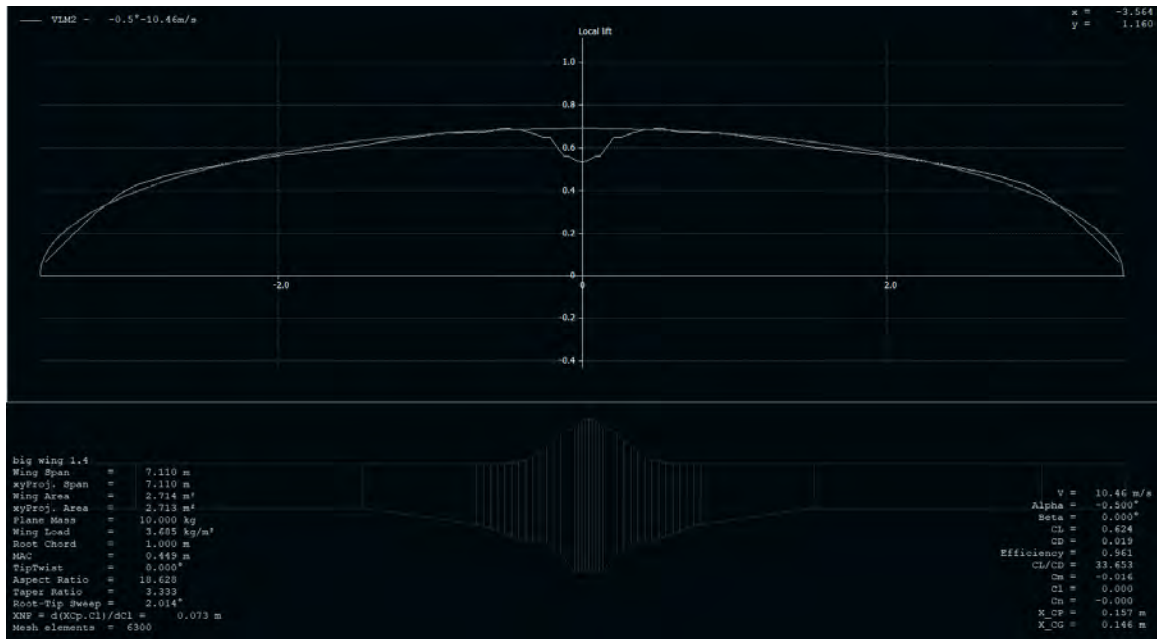
Figure 5-15: 3rd Design Lift Distribution

Figure 5-16: 4th Design Lift Distribution
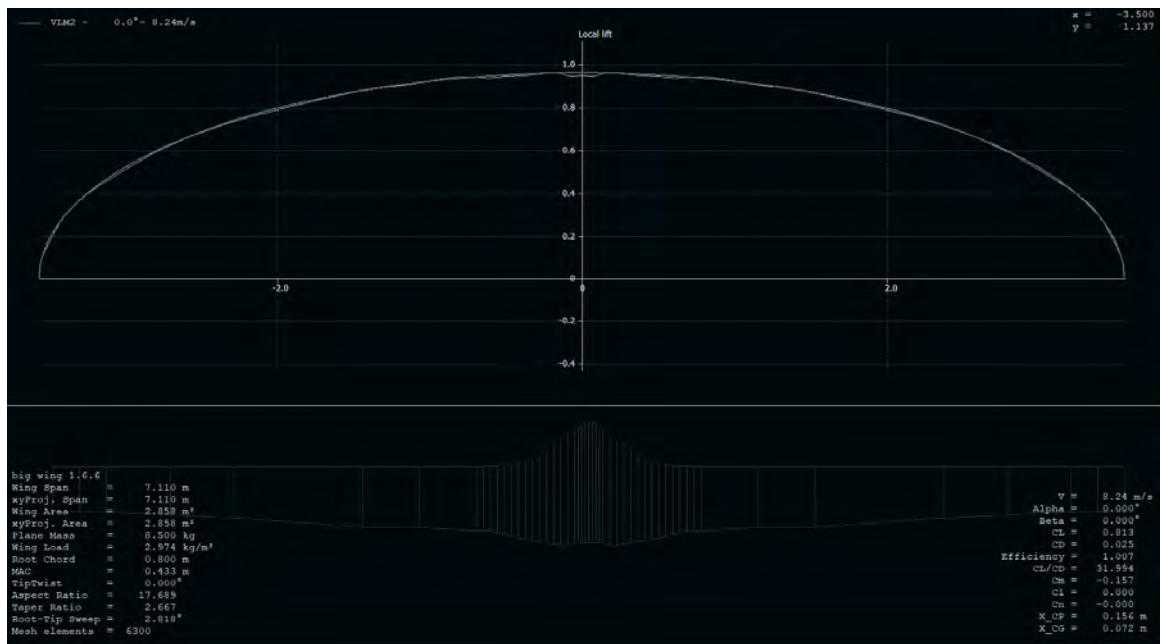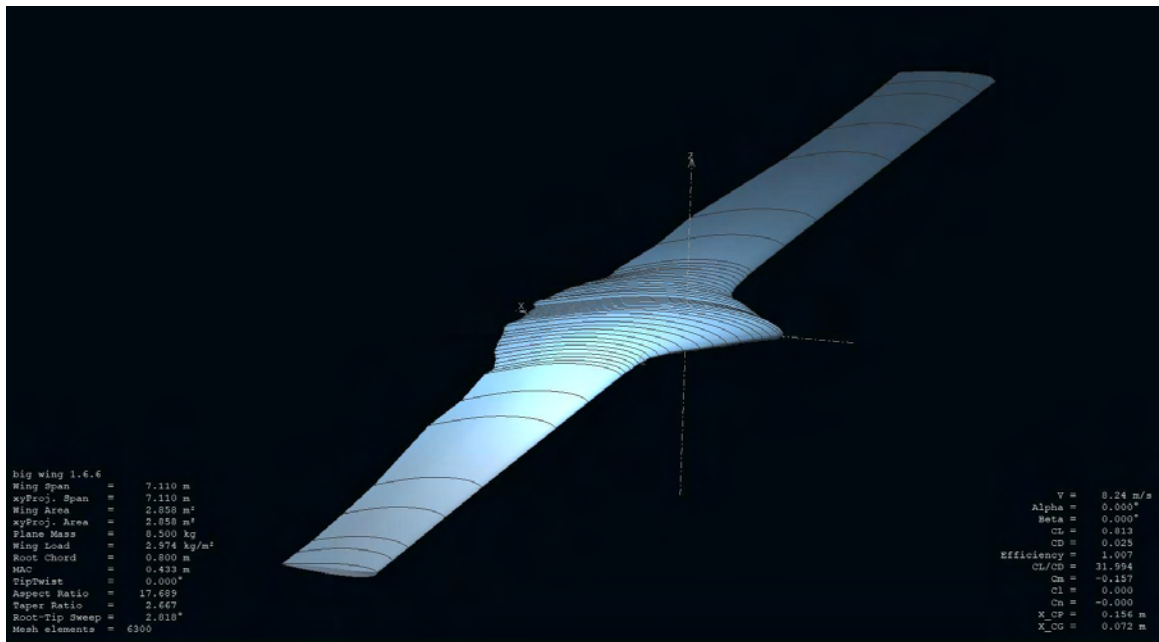
Figure 5-17: Final Design Lift Distribution

The simulation in the XFLR5 was executed for fixed "10kg" lift, and the results were the speed that the aircraft must fly, as also its aerodynamic coefficients. As soon as the elliptic lift distribution was achieved the next step was the comparison of the two optimized Wing-Fuselage concepts so that can be selected the one with the smaller drag force.
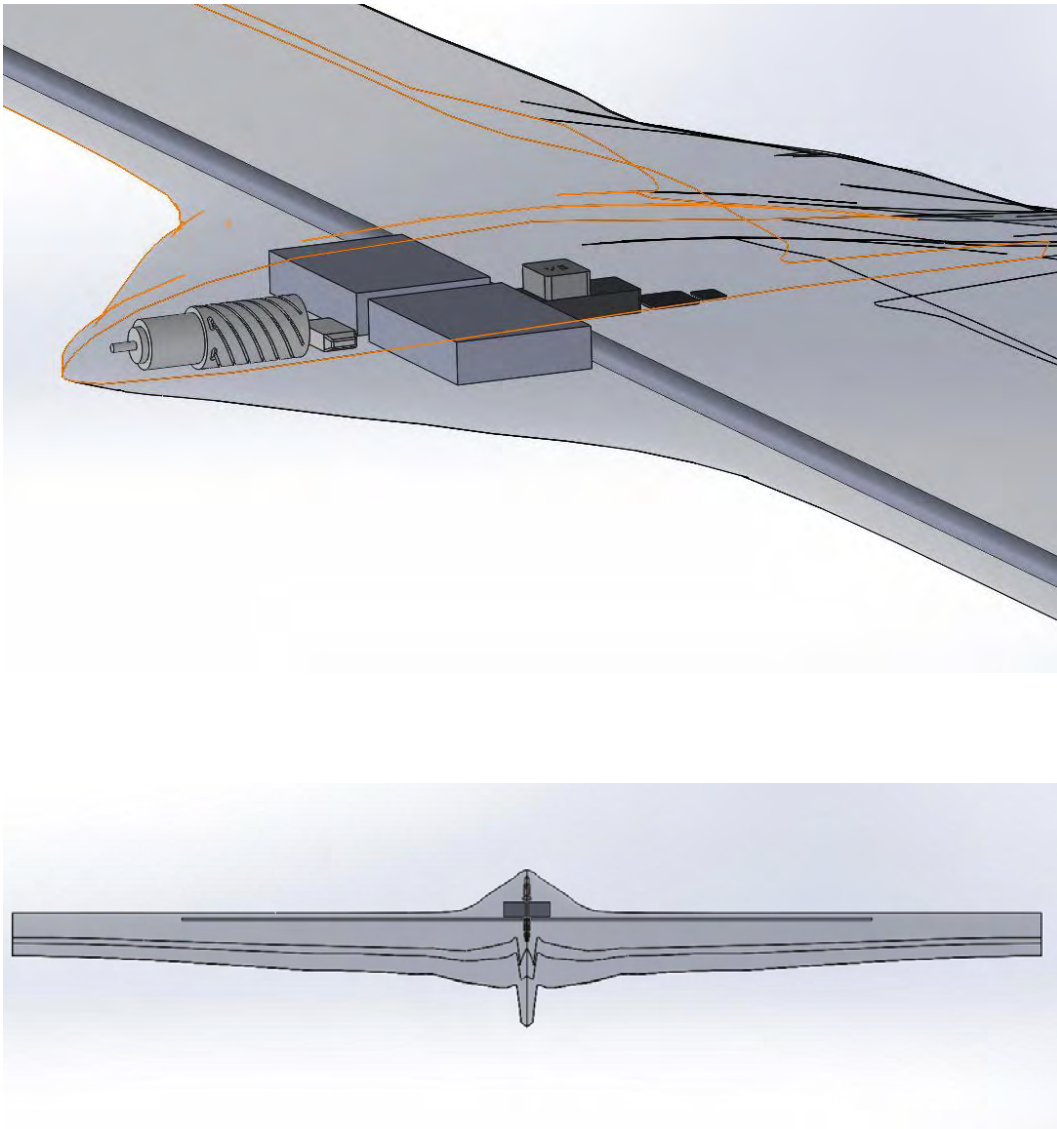
Figure 5-18: Final Assembly With Electrical Components

To accomplish that we had to run a more detailed simulation in the Ansys Fluent platform with different speed for each aircraft to produce the exact same amount of lift and the one with the smaller drag would be suitable for the project.

The input velocity for the tadpole/cylindrical fuselage concept was 12m/s and for the blended wing concept 10m/s as previously calculated with the help of XLFR5 and hand calculations. The blended wing concept had better aerodynamic efficiency, except from less drag it flies with smaller velocity, fact will help with less drag of the empennage, so is the one that has been chosen. The results are listed below.

`
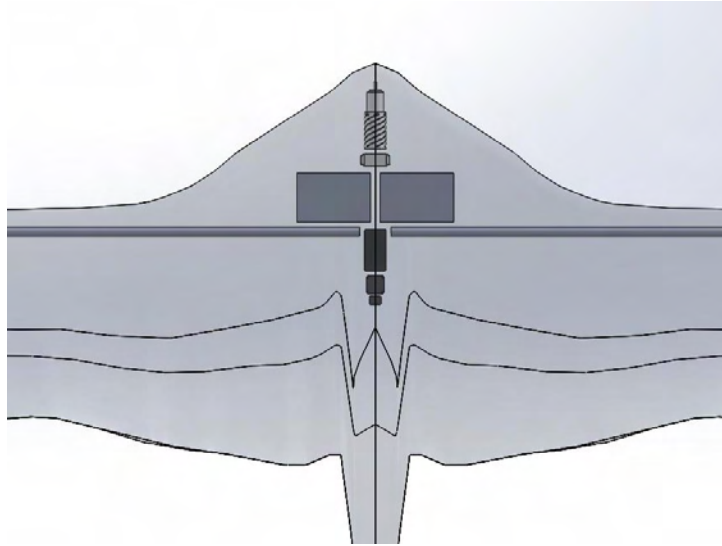
Figure 5-19: Blended Wing

	Tadpole/ Cylindrical Concept			Blended Wing Concept		
	Pressure	Viscous	Total	Pressure	Viscous	Total
DRAG[N]	1.49	2.08	3.57	1.53	1.77	3.30
LIFT[N]	101.32	0.058	101.38	98.94	0.055	98.99
POWER[W]			42.84			33
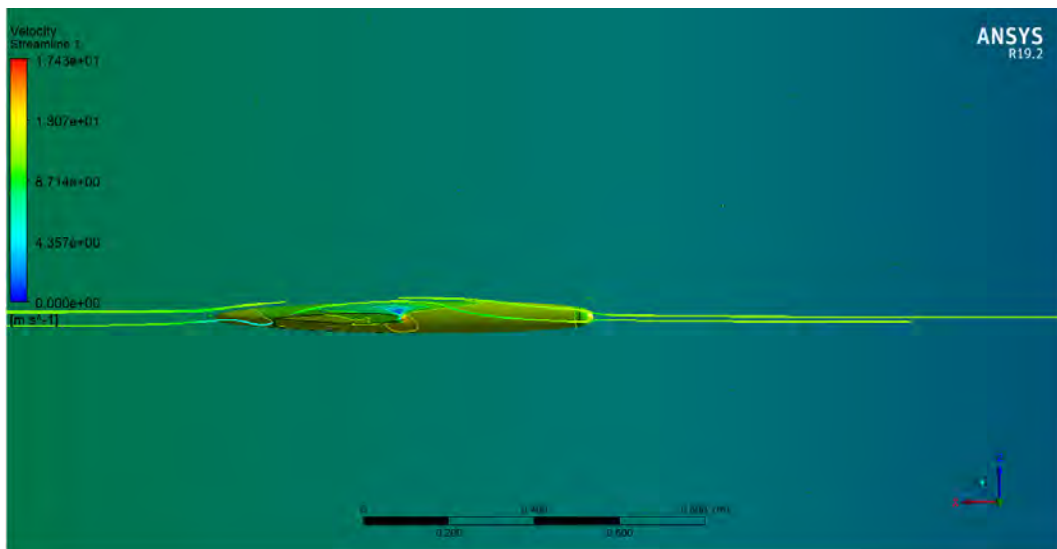
Figure 5-20: Tadpole/Cylindrical Concept
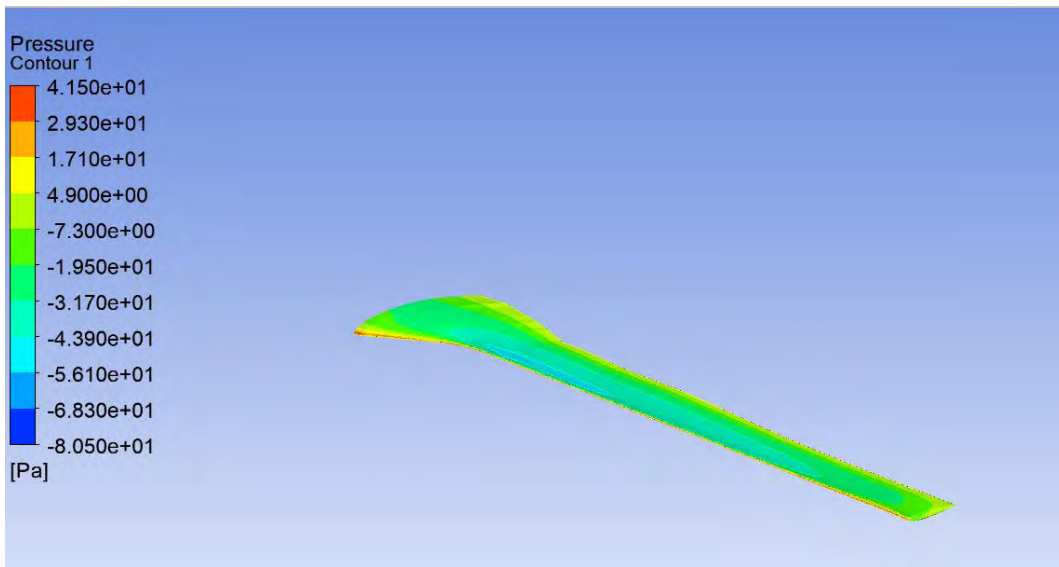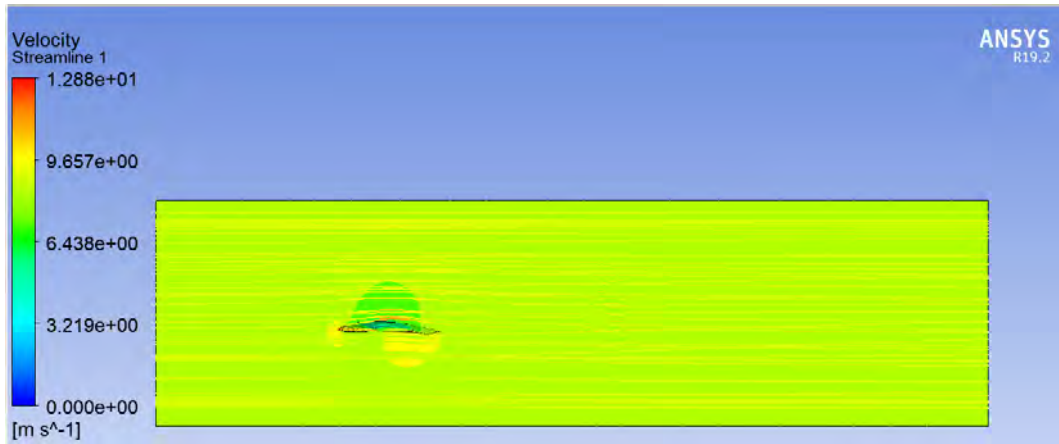
Figure 5-21: Blended Wing Fuselage Concept

Chapter6: Tail Design and Stability

6.1.   Stable Flight

Until this point we have chosen a proper airfoil for our high efficiency flight, we altered the geometry of the wing to match the elliptical lift distribution achieving minimum induced drag generation and we designed a fuselage that its purpose is to hold all the electrical components and actuators that the UAV need in order to operate. The next major step is to make the flight of our vehicle as smooth as possible. The importance of the stability analysis is vital to every vehicle and system that operates under transient conditions and is called to reject possible disturbances while trying to reach the set point that the user stations. For example, our aerial vehicle needs to stay at a certain level during its flight and damp any oscillations along the 3 axis because that way will be flying in the desired operational point which is designed to have maximum efficiency. Our stability analysis consists of three parts.

- **Load case:**   Every possible combinations of angles in each axis causes the flow over the UAV to create moments and forces around the center of mass. Acquiring these data will give us the aero map of the construction. To achieve this, we need to run simulations for each angle change on each direction and the problem is that during the simulation we cannot simplify our model by using a symmetry plane. Furthermore, the forces that act on an object that moves inside a fluid are proportional to the square of the velocity. This means that the steady state simulation will not provide us with adequate data. Therefore, a transient simulation has to be set in order to get the right moments around the 3 axis.

- **Dynamics of a UAV:**   After the data have been acquired there is further need for a dynamic simulation to take place. The environment of Simulink allows for a dynamic simulation by simulating the system with a 6 DOF block. The simulation considers that the forces acting on the body do not create moment coupling in a random axis but only around the center of mass. That way we can consider the center of mass as a fixed point for every axis.

- **Empennage:** The empennage term is used to describe the tail of the glider which can be broken in two parts the vertical one and the horizontal one. The length that they will be placed at, the area of the control surfaces and the type of the airfoil that will be used defines the response of the system at any changes. To make things simpler the whole concept is to create a greater moment around the center of mass with the smallest possible deflection of the empennage. The moment is defined as a Force that acts on a distance from the rotation axis. The force itself of the empennage is a function of its area, the rotational speed and the lever that the force is placed at relative to the center of rotation. Therefore, a compensation has to be made between the area of the control surfaces and the location of them behind the wing.

- **PID tuning:** The PID is a great field of automation study and provides the users the ability to control the response characteristics of a system. For example, we can change the behavior of the system by altering the values of the PID constants. We can make a system faster but with greater error of the set point or reduce the overshooting with compensating to the rise time which is the time that the system needs to reach the set point. The PID controllers here are not different physical objects and should not be confused with the PWM controllers of the motor. They are embedded inside the flying controller each one for the set of moving control areas. The tuning that needs to be done is to define the parameters for each set and the tuning method will not provide any information for the moving areas but it will only optimize their function on the overall stability.
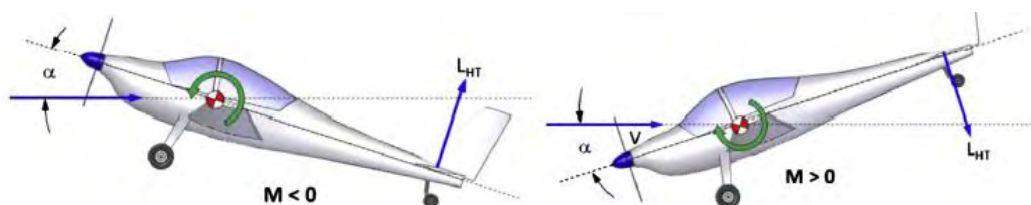
Figure 6-1: Two different scenarios at high AoA and small AoA

Requirements for Static Longitudinal Stability: Consider the airplane in the figure below. The image to the left shows it at a high AOA and the right one at a low AOA. The figure helps build an understanding of what is meant by longitudinal stability. In the left image, the horizontal tail (HT) generates a lift force, L_{HT}, which points upward and, thus, tends to reduce the AOA by lowering the nose. Using the standard stability coordinate system, the resulting moment has a negative magnitude. This means that grabbing around the y-axis with the right hand to generate this nose-down rotation requires the thumb to point in the negative y-direction. To pitch the nose up requires the thumb to point in the positive y-direction. The right image of the figure shows the opposite. Due to the low AOA, the HT is generating lift in the downward direction causing a tendency to increase the AOA. This requires the moment to have a positive value. This means that somewhere between the two extremes is an AOA for which there is no tendency for the HT to increase or decrease the AOA. This is the trim AOA. An airplane whose stabilizing surface (here the HT) generates enough lift force to force the aircraft to a specific trim AOA is called a stable aircraft. These two conditions have been plotted. The conditions consist of a > 0 and M <0 in the left image and a < 0 and M> 0 in the right image. The graph shows clearly that in order for the aircraft to be stable, the pitching moment curve must necessarily have negative slope.

This slope is denoted by the symbol Cma. Additionally, in order to be able to trim the airplane at an AOA that generates positive lift, the intersection to the y-axis (C_m-axis), denoted by Cm0, must be larger than zero. Mathematically, this is written as follows:

$$C_{m_\alpha} = \frac{\partial C_m}{\partial \alpha} < 0$$

Requirement for static trimmability:

$$C_{m_o} > 0$$

If these conditions are satisfied, then there exists an AOA > 0 for which the Cm is equal to zero. The importance of AOA > 0 is that the vehicle can generate lift in the opposite direction of the weight and simultaneously be statically stable.
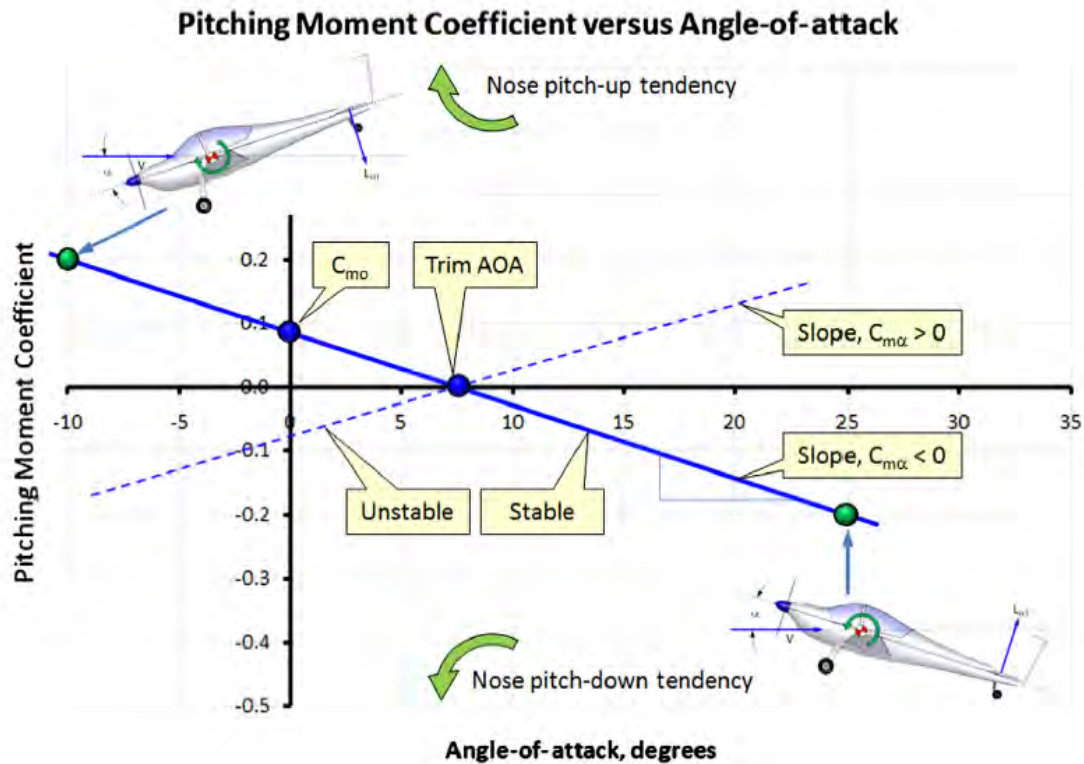
Figure 6-2: Plot of the two scenarios Cm vs AoA

The next thing that we have to check is the corresponding stability around the yaw axis (directional stability). Directional stability is the capability of the vehicle to weather vane. Imagine standing behind an actual weather vane with the wind directly in your face. If the vane is rotated so its nose points, say, right (and the tail points left) intuition tells us its tail will generate lift that points to the right, in the positive y-direction (see depiction in the upcoming figure). This, in turn, generates a moment whose tendency is to rotate the nose left and align it (and the tail) with the wind. Since the moment corrects the alignment, it is said to be restoring. If the above weather vane is yawed nose right, then, using the stability coordinate system (SCS), the angle b< 0°. This means that if looking along the centerline of the vane, the wind would strike the left cheek. The restoring moment is negative because per the right hand rule, the resulting rotation is analogous to grabbing around the z-axis with the right hand to rotate it with the right thumb pointing upward e in the negative z-direction. The opposite holds true if the weather vane is rotated nose left e a positive moment (thumb

pointing down) is then required to bring the nose right to the initial position. As we can see from the figure it shows how this establishes requirements for static directional stability. It turns out that in order for this correcting tendency to be realized, the slope of the yawing moment curve must have a positive slope. Mathematically this is written as follows:

Requirement for static directional stability:

$$C_{n_\beta} = \frac{\partial C_n}{\partial \beta} > 0 \quad \text{and} \quad C_n = 0 \quad \text{if} \quad \beta = 0$$

Next consider lateral stability (see the figure below). It differs from both longitudinal and directional stability in that it requires sideslip (or yaw), and not roll itself, to be corrected (ignoring the application of devices like ailerons). This is the aforementioned dihedral effect. The geometric features of airplanes are such that when flying asymmetrically a restoring rolling as well as directional moments are created. It is the responsibility of the designer to decide how to manipulate the geometry to make these moments restoring or convergent (and not diverging). Dihedral effect has many sources as will become evident shortly. Consider the airplane in the upper left part of the figure, whose nose points to the right of the wind direction (which is normal to the plane). For now, consider only the contribution of the wing to the rolling moment. It can be seen from the top view in the lower left corner that the left wing leads the right one. This causes asymmetric loading on the wing that generates more lift on the left wing than the right one. The difference creates a rolling moment that tends to lift the leftwing and bring it back to level. The rolling moment is positive because, according to the right-hand rule, the resulting moment vector points forward (the thumb would point forward) along the positive x-axis. The opposite holds if the nose is yawed to the left so the rightwing leads the left one; a negative moment is created. By plotting a line between those two conditions it can be seen that the rolling moment must have a negative slope in order to be stable. Mathematically:

$$C_{l_\beta} = \frac{\partial C_l}{\partial \beta} < 0 \quad \text{and} \quad C_l = 0 \quad \text{if} \quad \beta = 0$$

## 6.2.	Initial Empennage Design

For the initial layout a historical approach is used for the estimation of tail size. The effectiveness of a tail in generating a moment about the center of gravity is proportional to the force (lift) produced by the wing. Thus, it would be expected that the tail size would be in some way related to the wing size. In fact, there is a directly proportional relationship between the two. Therefore, the tail area divided by the wing area should show some consistent relationship for different aircraft if the effects of tail moment arm could be accounted for. The force due to tail lift is proportional to the tail area, Thus, the tail effectiveness is proportional to the tail area times the tail moment arm. This product has units of volume, which leads to the ''tail volume coefficient'' method for initial estimation of tail size. Rendering this parameter nondimensional requires deciding by some quantity with units of length. For a vertical tail the wing yawing moments which must be countered are most directly related to the wing span b. This leads to the ''vertical tail volume coefficient'', which is defined as:

$$c_{VT} = \frac{L_{VT}S_{VT}}{b_w S_w}$$

For a horizontal tail or canard, the pitching moments which must be countered are most directly related to the wing mean chord (C_w). This leads to the ''horizontal tail volume coefficient'', which is described by the equation bellow:

$$c_{HT} = \frac{L_{HT}S_{HT}}{C_W S_W}$$

Where the moment arm (L) is commonly approximated as the distance from the tail quarter-chord to the wing quarter-chord.

The definition of tail momenta arm is shown in the figure bellow along with the measured to the aircraft centerline, while a canard's area is commonly considered to include only the exposed area. If twin vertical tails are used, the vertical tail area is the sum of the two.
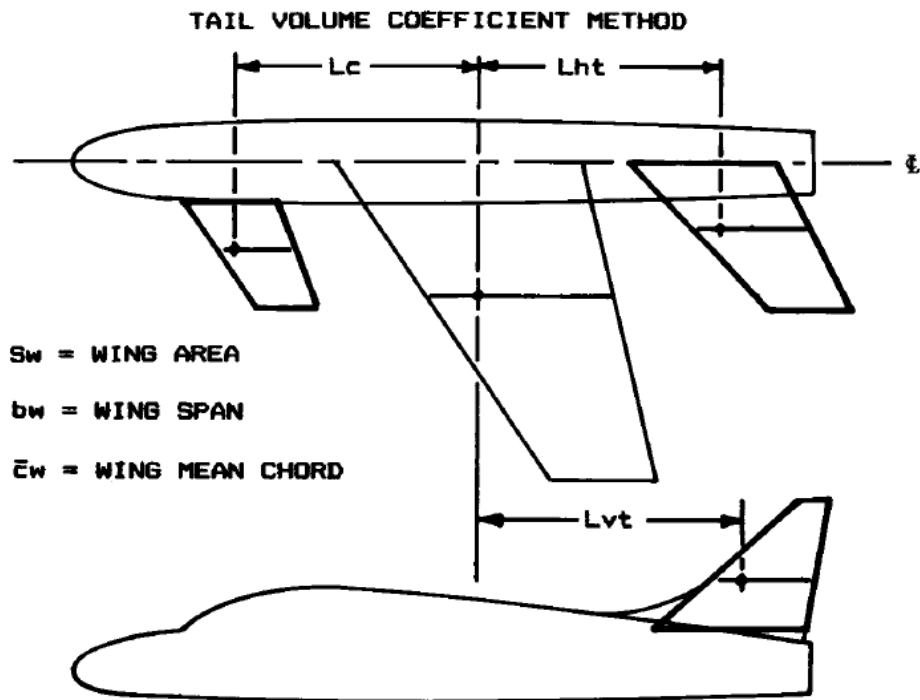
Figure 6-3: Initial empennage sizing

Statistical data provide us with typical values of the two tail volume coefficients for different classes of aircraft.

	Typical values	
	Horizontal c_{HT}	Vertical c_{VT}
Sailplane	0.50	0.02
Homebuilt	0.50	0.04
General aviation—single engine	0.70	0.04
General aviation—twin engine	0.80	0.07
Agricultural	0.50	0.04
Twin turboprop	0.90	0.08
Flying boat	0.70	0.06
Jet trainer	0.70	0.06
Jet fighter	0.40	0.07
Military cargo/bomber	1.00	0.08
Jet transport	1.00	0.09

Figure 6-4: Tail volume coefficients

$$S_{VT} = c_{VT} b_w S_w / L_{VT}$$

$$S_{HT} = C_{HT} C_W S_W / L_{HT}$$

To calculate the tail size, the moment arm must be estimated. This can be approximated at this stage of design by a percent of the fuselage length as previously estimated. For an aircraft with a front-mounted propeller, Raymer proposes, the tail arm is about 60% of the fuselage length. For an aircraft with the engines on the wings, the tail arm is about 50-55% of the fuselage length. For aft-mounted engines the tail arm is about 45-50% of the fuselage length. A sailplane has a tail movement arm of about 65% of the fuselage length. Our UAV type can be related to the sailplane and since we need steady with not great response characteristics plane the 65% is the case for us. The problem with our case is that the above methodology needs an estimation for the fuselage which is based on same methods that rely on the thrust to weight ratio that the sailplane is called to reach. With those numbers and since our UAV has a great moment of inertia around the y axis the vertical tail had to be enormous for the responses of the above methodology. The initial design is presented in the following figures.

Table 6-1: Initial empennage sizing, input parameters

INPUT			
Wing Area	Sw =	2.858	m2
Wing Span	bw =	7.11	m
Wing Mean Chord	cv =	0.402	m
Tail Volume	Cht =	0.5	
Coefficient	Cvt =	0.02	
Fuselage Length (by initial sizing)	Lf =	2.30	m

Table 6-2: Initial empennage sizing, output parameters

OUTPUT			
Lvt =	1.495	m	
Lht =	1.495	m	
Elevator Area	Sht =	0.38422	m2
Rudder Area	Svt =	0.25825	m2
Elevator Span	bht =	1.3	m
Rudder Span	bvt =	0.9	m

6.3.   Static Stability

At this point we started a simulation process to accomplish the desired flight stability. The goal was for the moment coefficient to be negative and close to zero for zero angle of attack and with negative derivative with respect to angle of attack. The initial empennage was designed but the results weren't as expected. We continued with further alteration in geometry and the desired behaviour was achieved with the following empennage parameters.
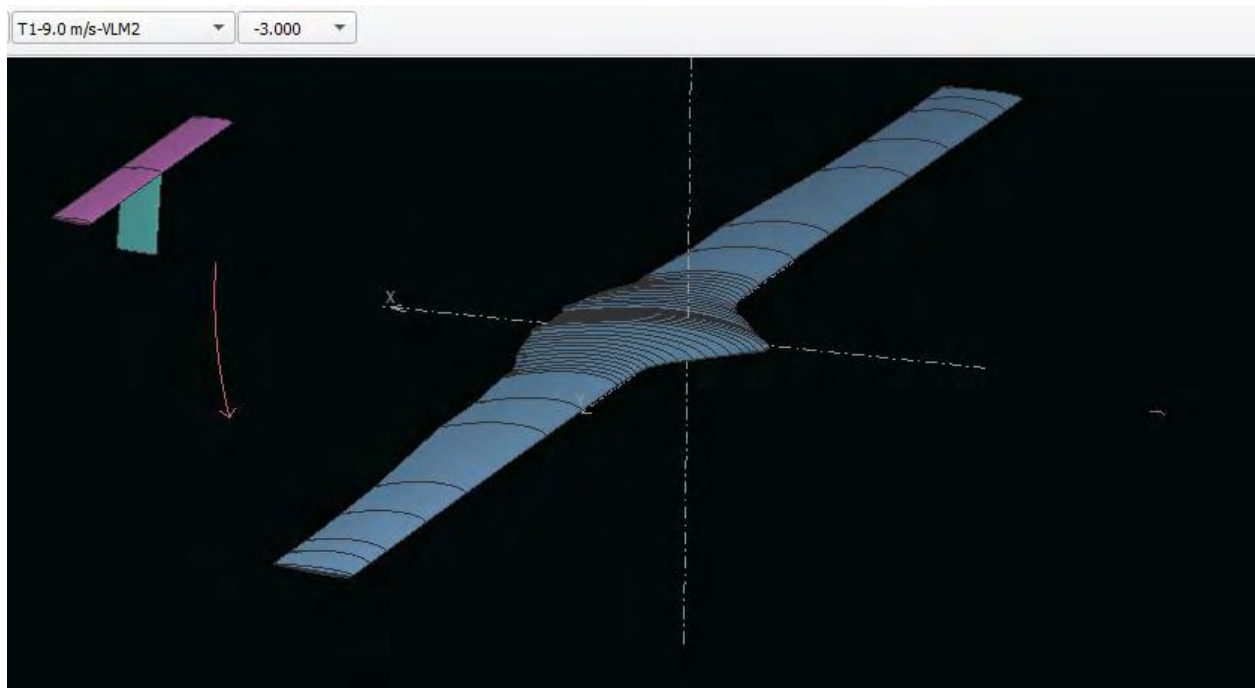
Figure 6-5: AoA = -3°

Elevator Span:	1.5m	Lvt:	2m
Elevator Chord:	0.15m	Lht:	2m
Elevator Area:	0.225m²		
Rudder Span:	0.6m		
Rudder Chord:	0.15m		
Rudder Area:	0.09m²		
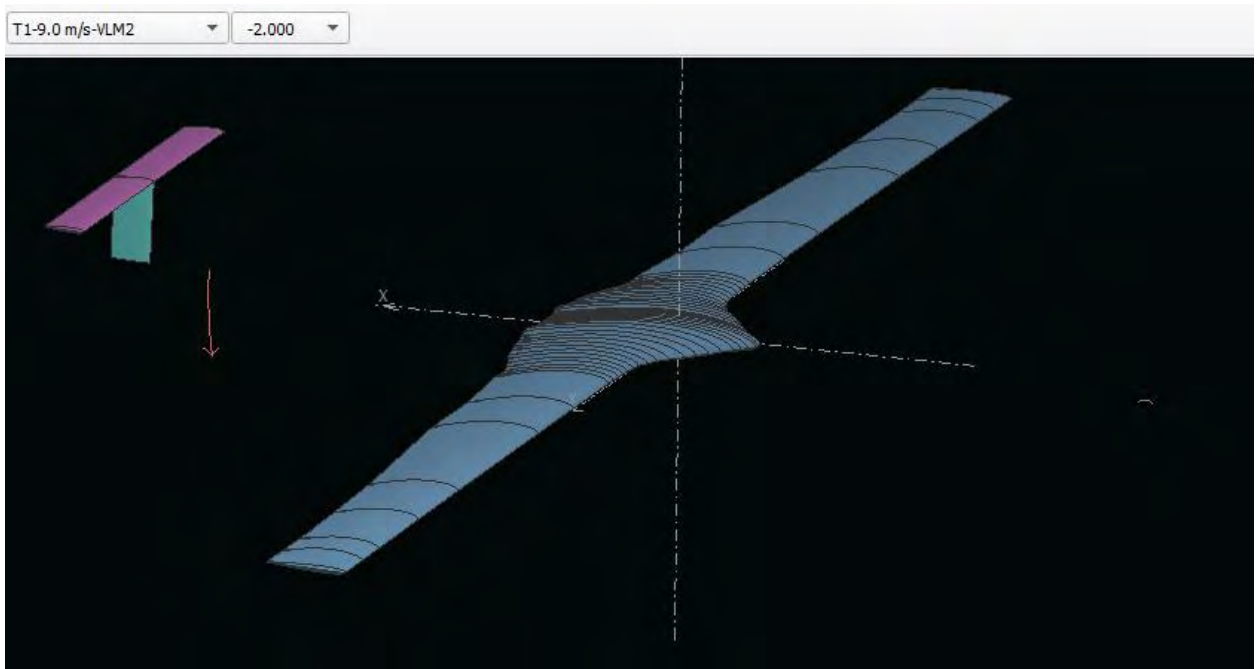
Figure 6-7: AoA = -2°
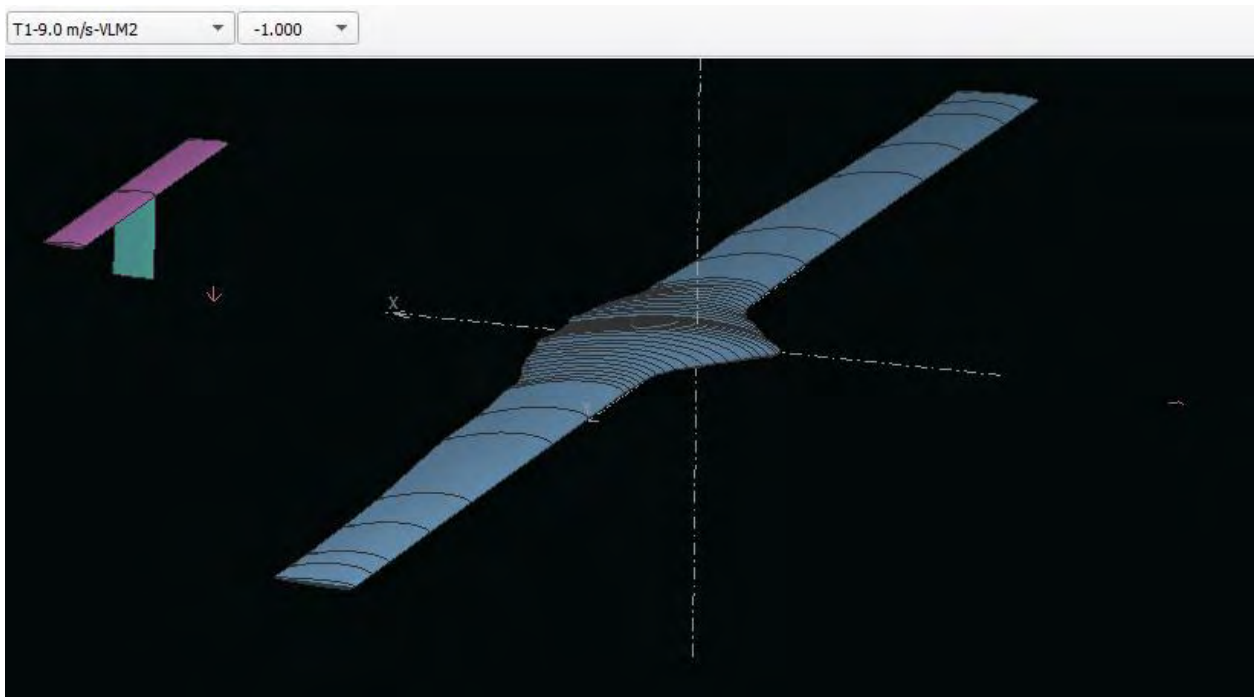
Figure 6-6: AoA = -1°
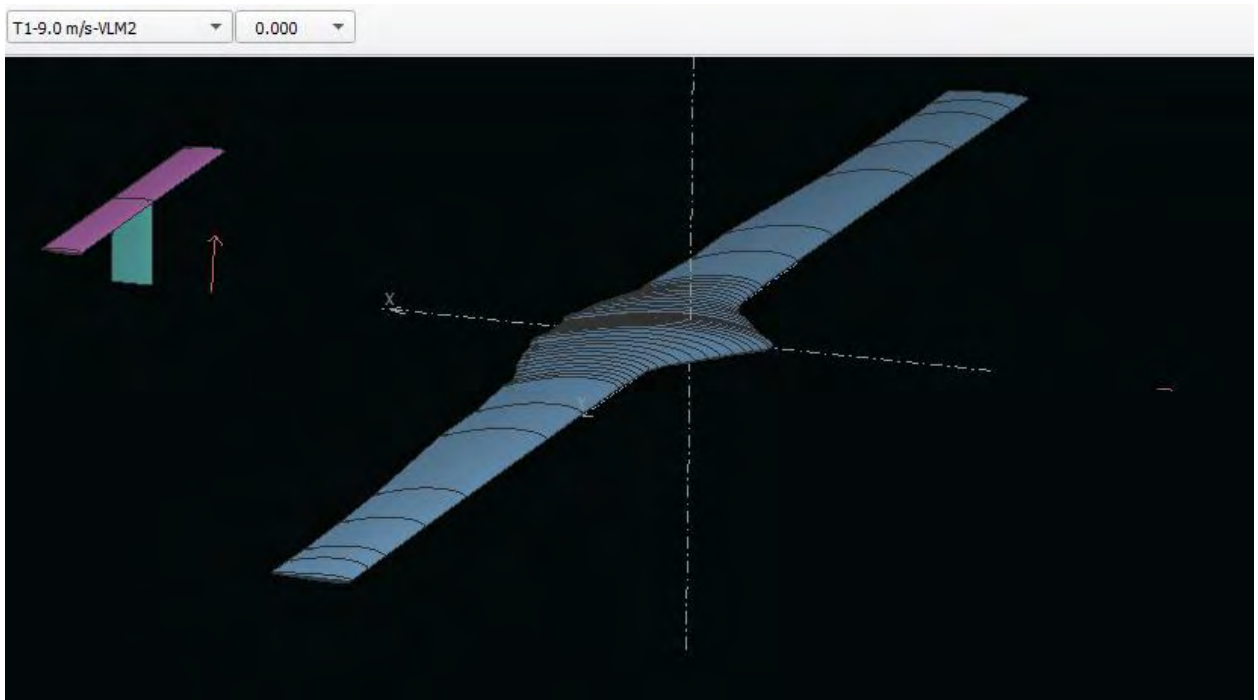
Figure 6-9: AoA=0º
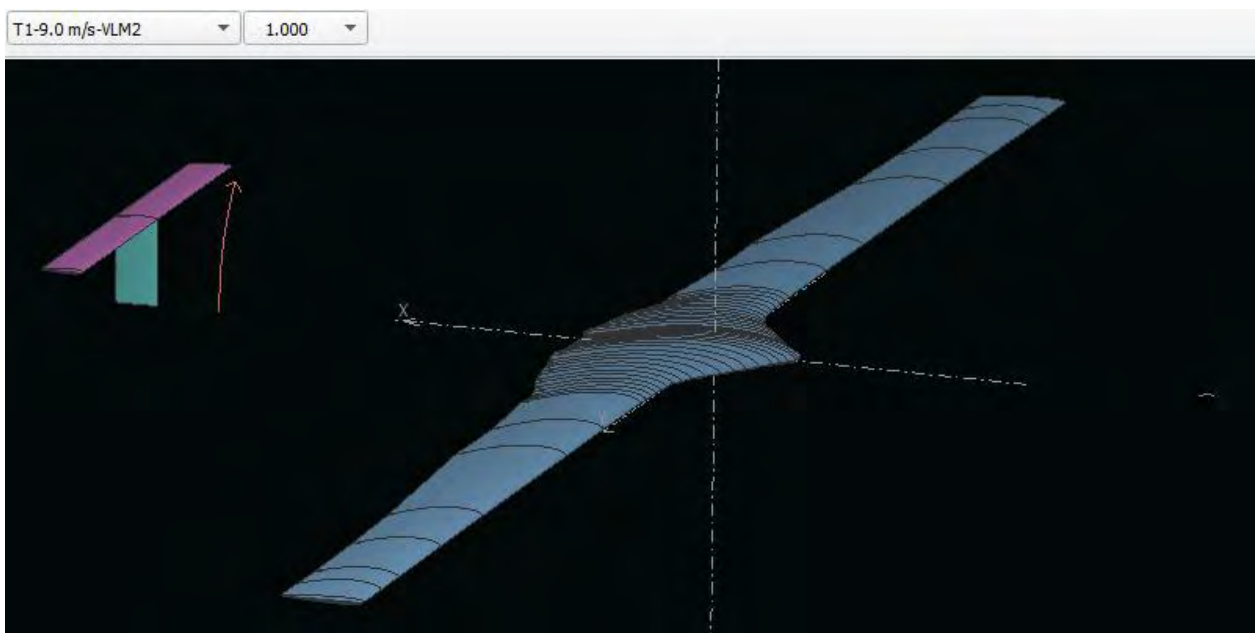
Figure 6-8: AoA = 1º
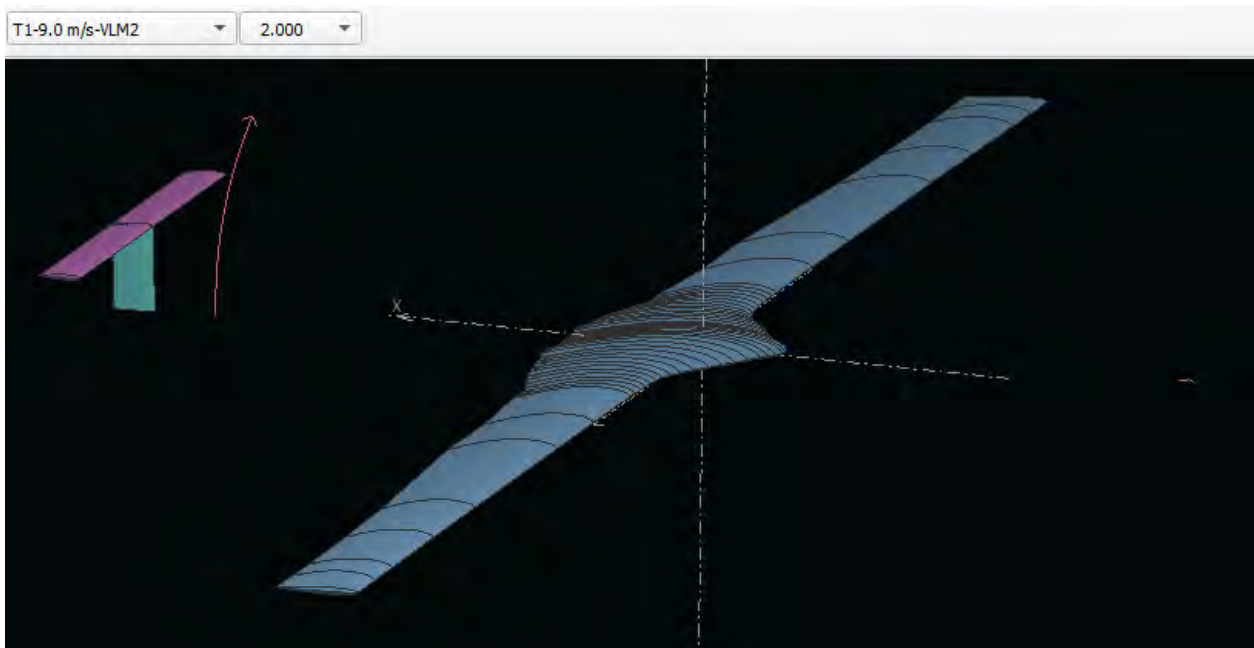
Figure 6-11: AoA = 2 °
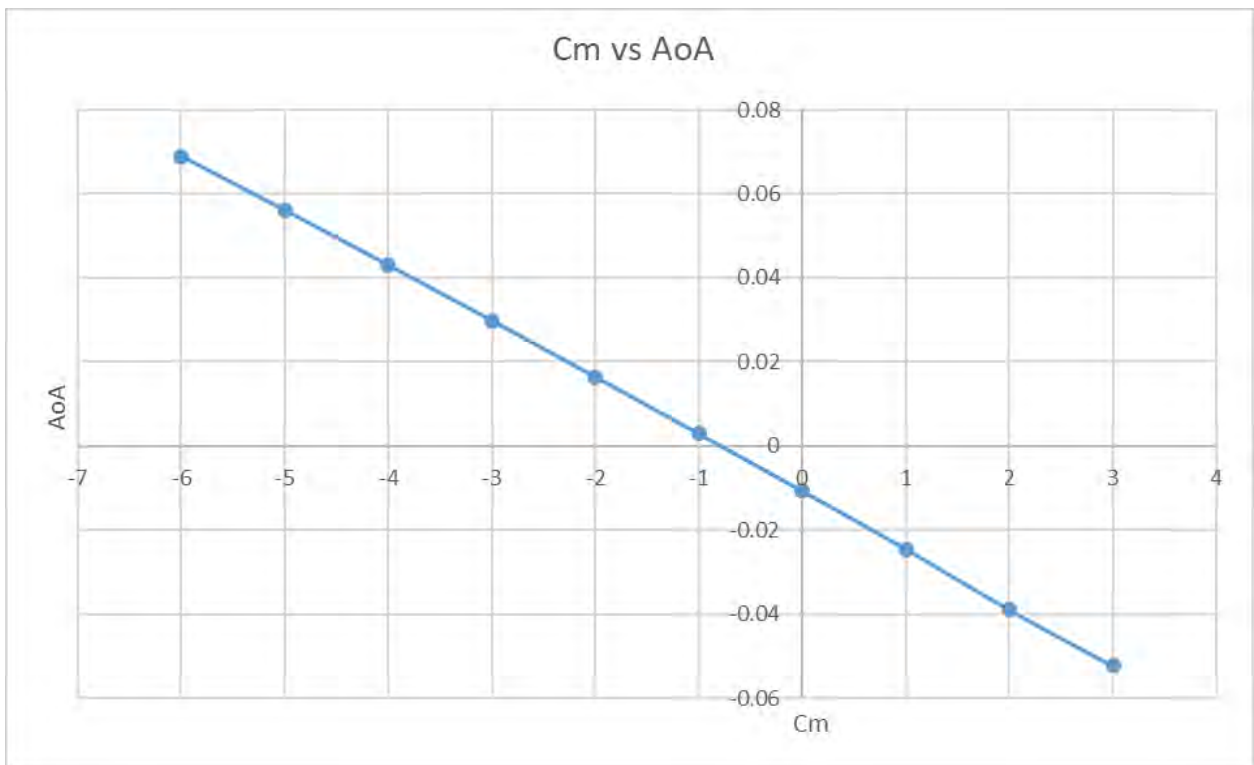
Figure 6-10: Cm vs AoA in final empennage design

6.4. Dynamic Stability

After the aircraft proven statically stable, it must be tested for dynamic stability as well. The dynamic stability analysis took place in XFLR5 and the procedure is described in the upcoming paragraphs. A well-designed aircraft has 4 natural longitudinal modes and 4 natural lateral modes.

Longitudinal	Lateral
2 symmetric phugoid modes 2 symmetric short period modes	1 spiral mode 1 roll damping mode 2 Dutch roll modes

Phugoid modes: The longer period mode, called the "phugoid mode" is the one in which there is a large-amplitude variation of air-speed, pitch angle, and altitude, but almost no angle-of-attack variation. The phugoid oscillation is a slow interchange of kinetic energy (velocity) and potential energy (height) about some equilibrium energy level as the aircraft attempts to re-establish the equilibrium level-flight condition from which it had been disturbed. The motion is so slow that the effects of inertia forces and damping forces are very low. Although the damping is very weak, the period is so long that the pilot usually corrects for this motion without being aware that the oscillation even exists. Typically, the period is 20–60 seconds. This oscillation can generally be controlled by the pilot.
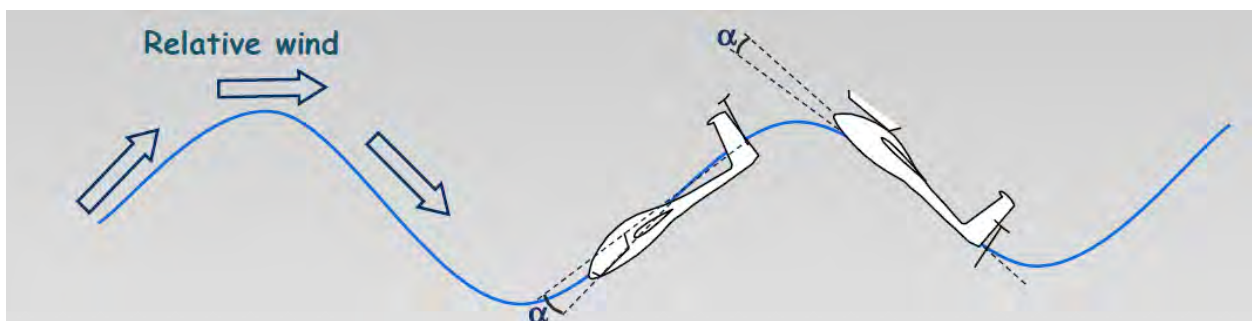
Figure 6-12: Phugoid modes

Short period modes: With no special name, the shorter period mode is called simply the "short-period mode". The short-period mode is a usually heavily damped oscillation with a period of only a few seconds. The motion is a rapid pitching of the aircraft about the center of gravity. The period is so short that the speed does not have time to change, so the oscillation is essentially an angle-of-attack variation. The time to damp the amplitude to one-half of its value is usually on the order of 1 second. Ability to quickly self-damp when the stick is briefly displaced is one of the many criteria for general aircraft certification.
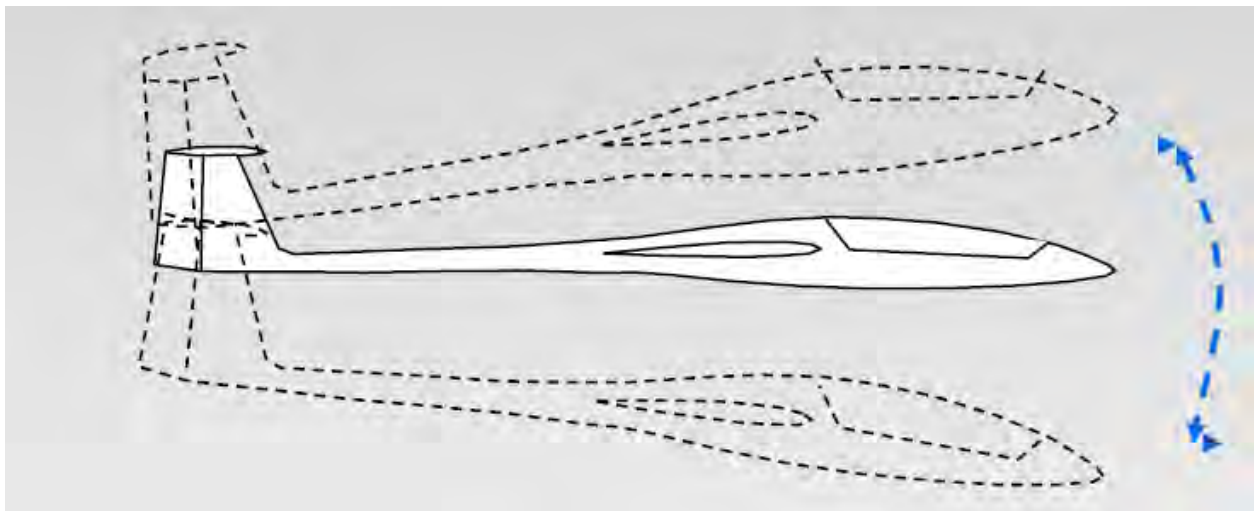
Figure 6-13: Short period modes

Spiral mode: Spiraling is inherent. Most aircraft trimmed for straight-and-level flight, if flown stick-fixed, will eventually develop a tightening spiral-dive. If a spiral dive is entered unintentionally, the result can be fatal. A spiral dive is not a spin; it starts, not with a stall or from torque but with a random, increasing roll and airspeed. Without prompt intervention by the pilot, this can lead to structural failure of the airframe, either as a result of excess aerodynamic loading or flight into terrain. The aircraft initially gives little indication that anything has changed. The pilot's "down" sensation continues to be with respect to the bottom of the airplane, although the aircraft actually has increasingly rolled off the true vertical. Under VFR conditions, the pilot corrects for this deviation from level automatically using the true horizon, while it is very small; but in IMC or dark conditions it can go unnoticed:

the roll will increase and the lift, no longer vertical, is insufficient to support the airplane. The nose drops and speed increases: the spiral dive has begun.
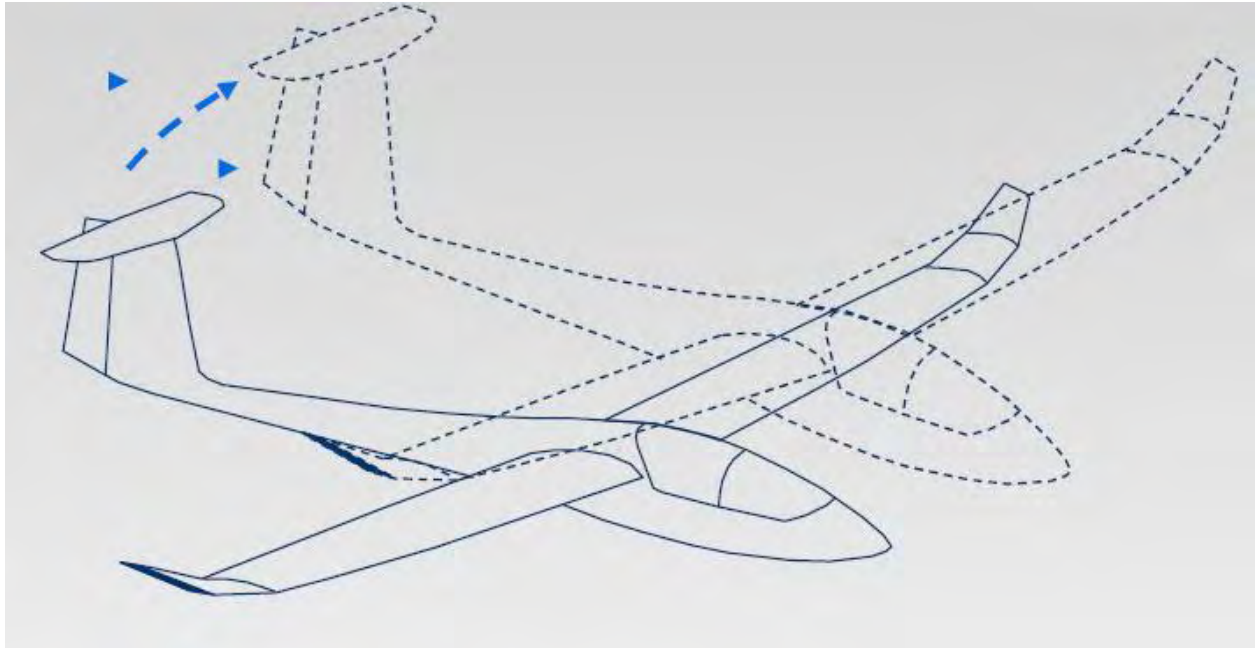
Figure 6-14: Spiral mode

Roll damping mode: Roll subsidence mode is simply the damping of rolling motion. There is no direct aerodynamic moment created tending to directly restore wings-level, i.e. there is no returning "spring force/moment" proportional to roll angle. However, there is a damping moment (proportional to roll rate) created by the slewing-about of long wings. This prevents large roll rates from building up when roll-control inputs are made or it damps the roll rate (not the angle) to zero when there are no roll-control inputs. Roll mode can be improved by dihedral effects coming from design characteristics, such as high wings, dihedral angles or sweep angles.
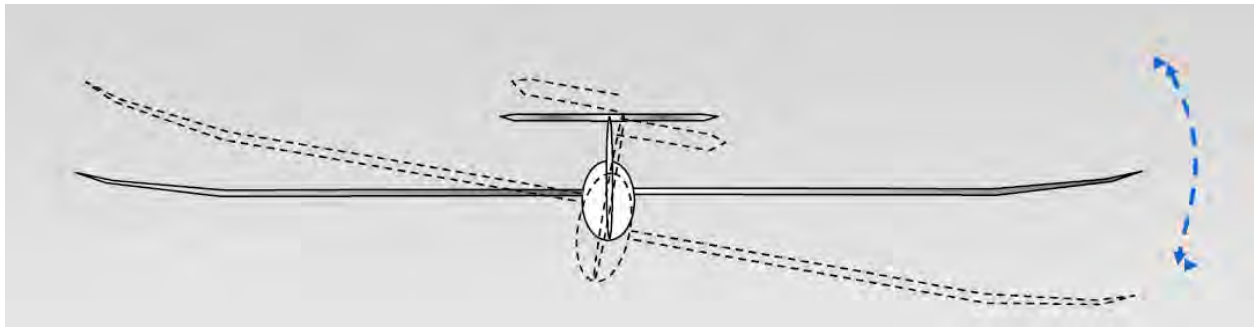
Figure 6-15: Roll damping mode

Dutch roll modes: The second lateral motion is an oscillatory combined roll and yaw motion called Dutch roll, perhaps because of its similarity to an ice-skating motion of the same name made by Dutch skaters; the origin of the name is unclear. The Dutch roll may be described as a yaw and roll to the right, followed by a recovery towards the equilibrium condition, then an overshooting of this condition and a yaw and roll to the left, then back past the equilibrium attitude, and so on. The period is usually on the order of 3–15 seconds, but it can vary from a few seconds for light aircraft to a minute or more for airliners. Damping is increased by large directional stability and small dihedral and decreased by small directional stability and large dihedral. Although usually stable in a normal aircraft, the motion may be so slightly damped that the effect is very unpleasant and undesirable. In swept-back wing aircraft, the Dutch roll is solved by installing a yaw damper, in effect a special-purpose automatic pilot that damps out any yawing oscillation by applying rudder corrections. Some swept-wing aircraft have an unstable Dutch roll. If the Dutch roll is very lightly damped or unstable, the yaw damper becomes a safety requirement, rather than a pilot and passenger convenience. Dual yaw dampers are required and a failed yaw damper is cause for limiting flight to low altitudes, and possibly lower Mach numbers, where the Dutch roll stability is improved.
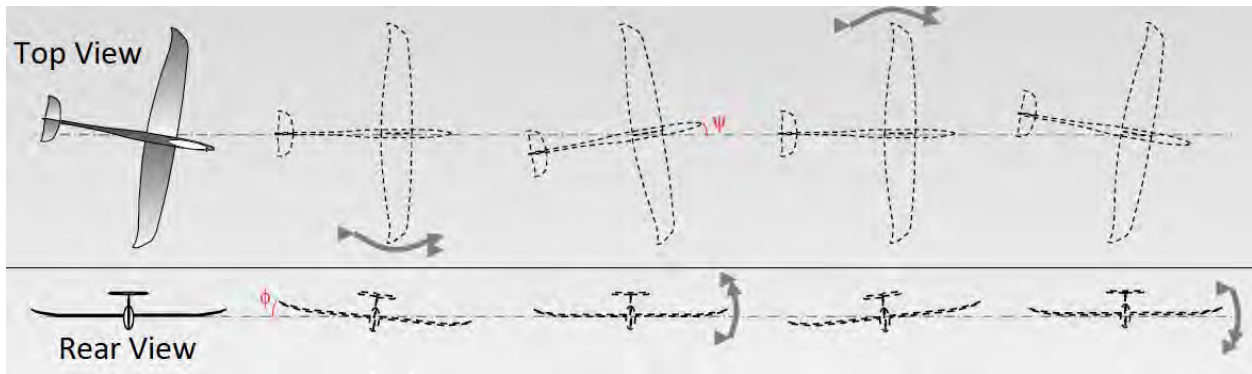
Figure 6-16: Ditch roll modes

These natural modes describe the aircraft's response on its natural frequencies, without any pilot's or flight controller's interference.

The code running in XFLR5:

- Searches the angle of attack such that Cm=0
- Calculates the trim speed to achieve a steady flight
- Evaluates the stability derivatives
- Extracts the eigenvalues

In the results we can see the time response in relevance to the variables that describe the aircraft's state at any instant. The four longitudinal variables are:

- **u** is the variation of speed along the x-axis
- **w** is the variation of speed along the z-axis
- **q** is the pitch rate, i.e. the rotation vector around the y-axis
- **θ** is the pitch angle, i.e. the angle between the stability x-axis and the horizontal flight line, the angle is positive for a nose up.

The four lateral variables are:

- **v** is the variation of speed along the w-axis
- **p** is the roll rate, i.e. the rotation vector around the x-axis
- **r** is the yaw rate, i.e. the rotation vector around the z-axis

- **φ** is the bank angle, i.e. the angle between the stability y-axis and the horizontal flight line, the angle is positive for a right wing down.
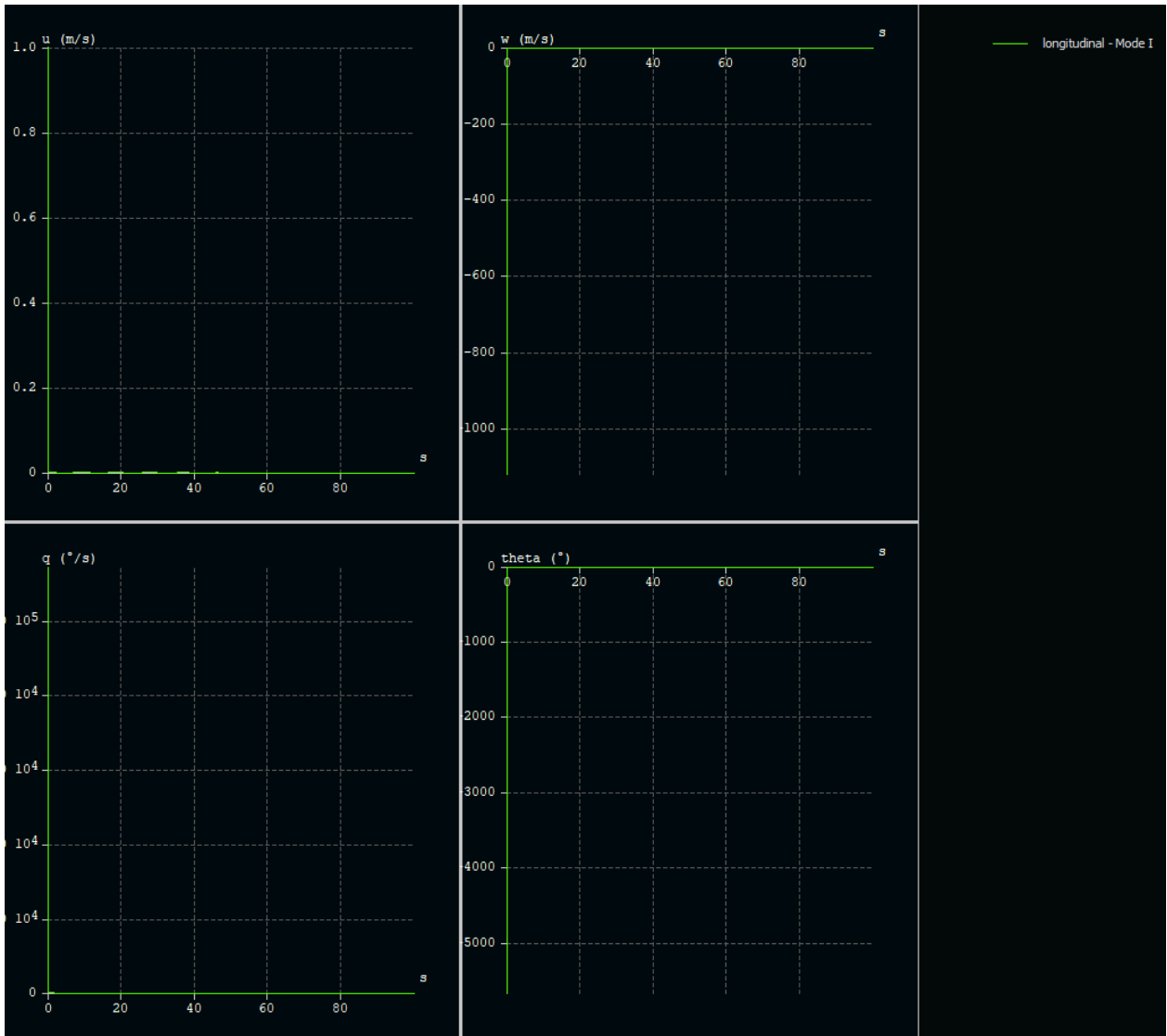
Figure 6-17: Longitudinal mode I, Short period mode
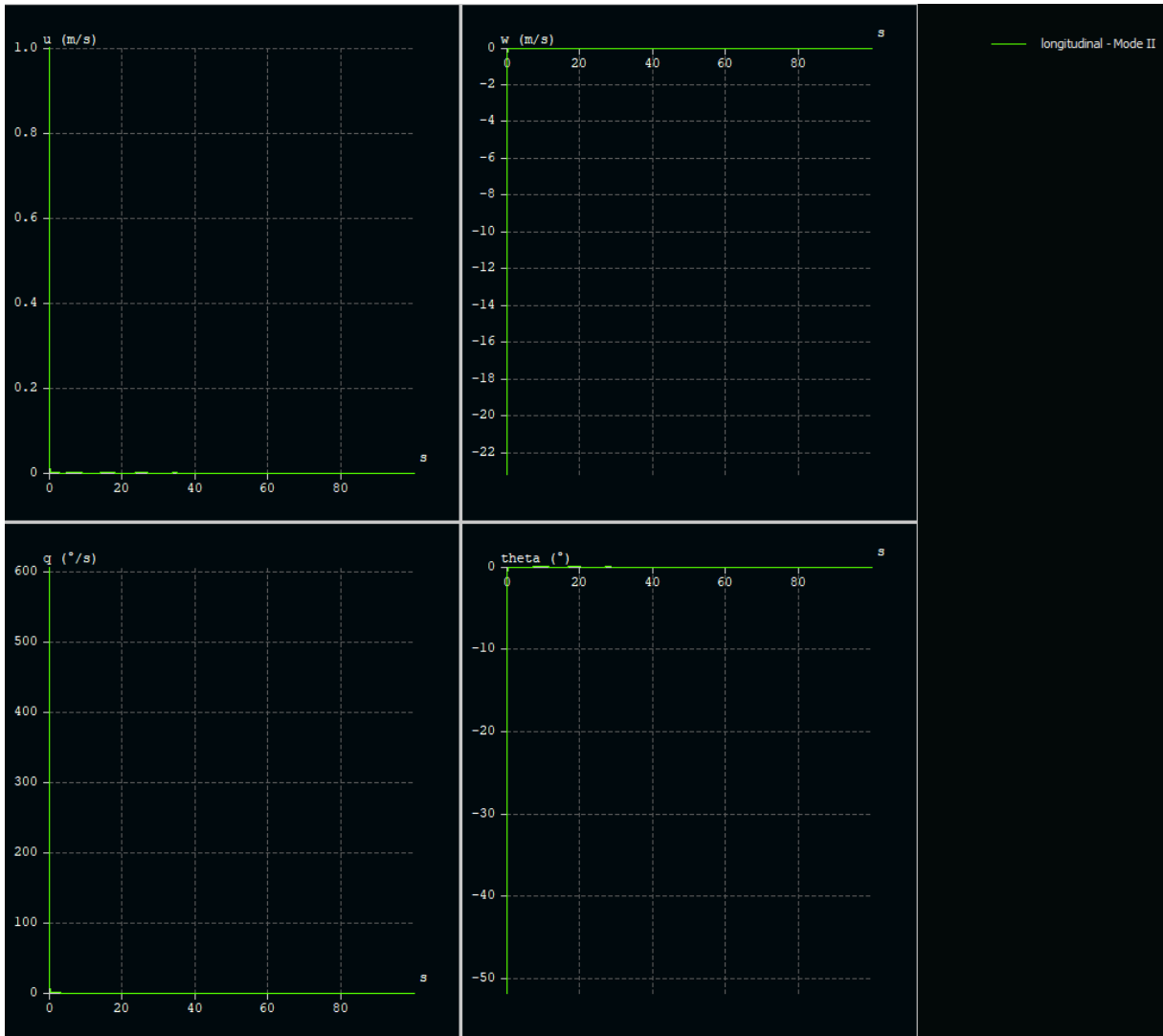
Figure 6-18:Longitudinal mode II, Short period mode

Figure 6-19:Longitudinal mode III & IV, Phugoid modes
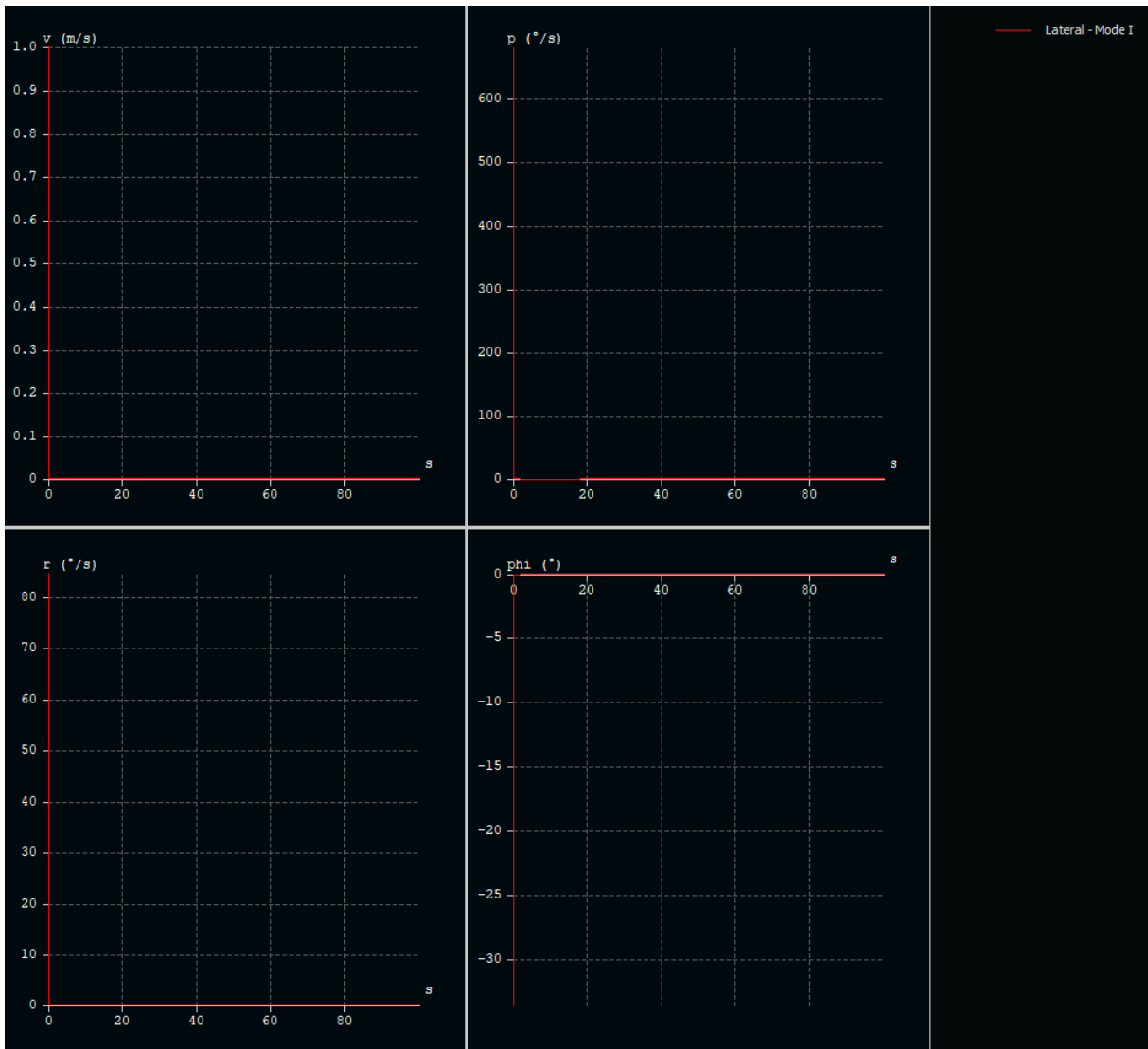
Figure 6-20:Lateral mode I, Roll damping mode
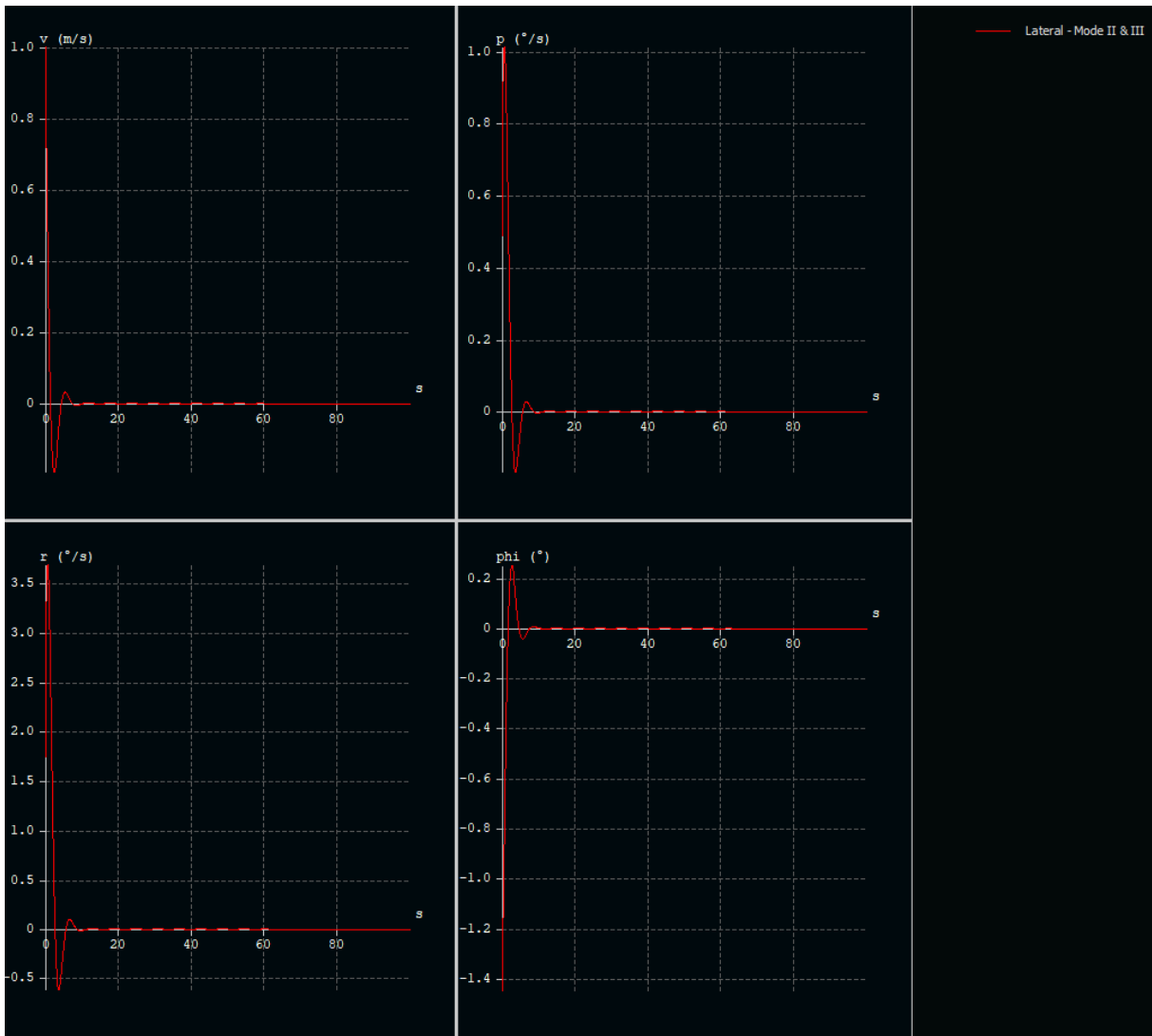
Figure 6-21:Lateral mode II & III, Dutch roll modes
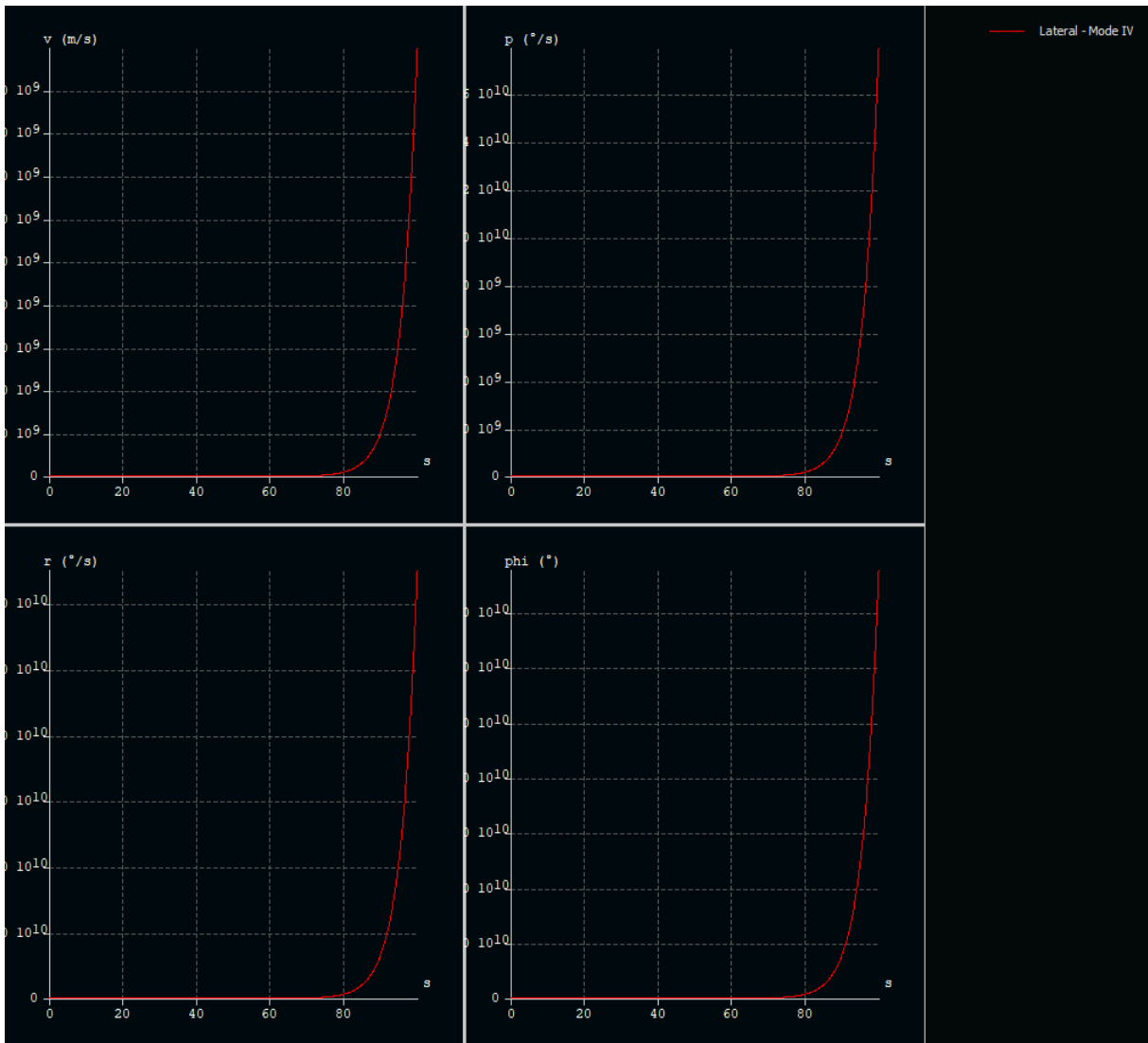
Figure 6-22:Lateral mode IV, Spiral mode
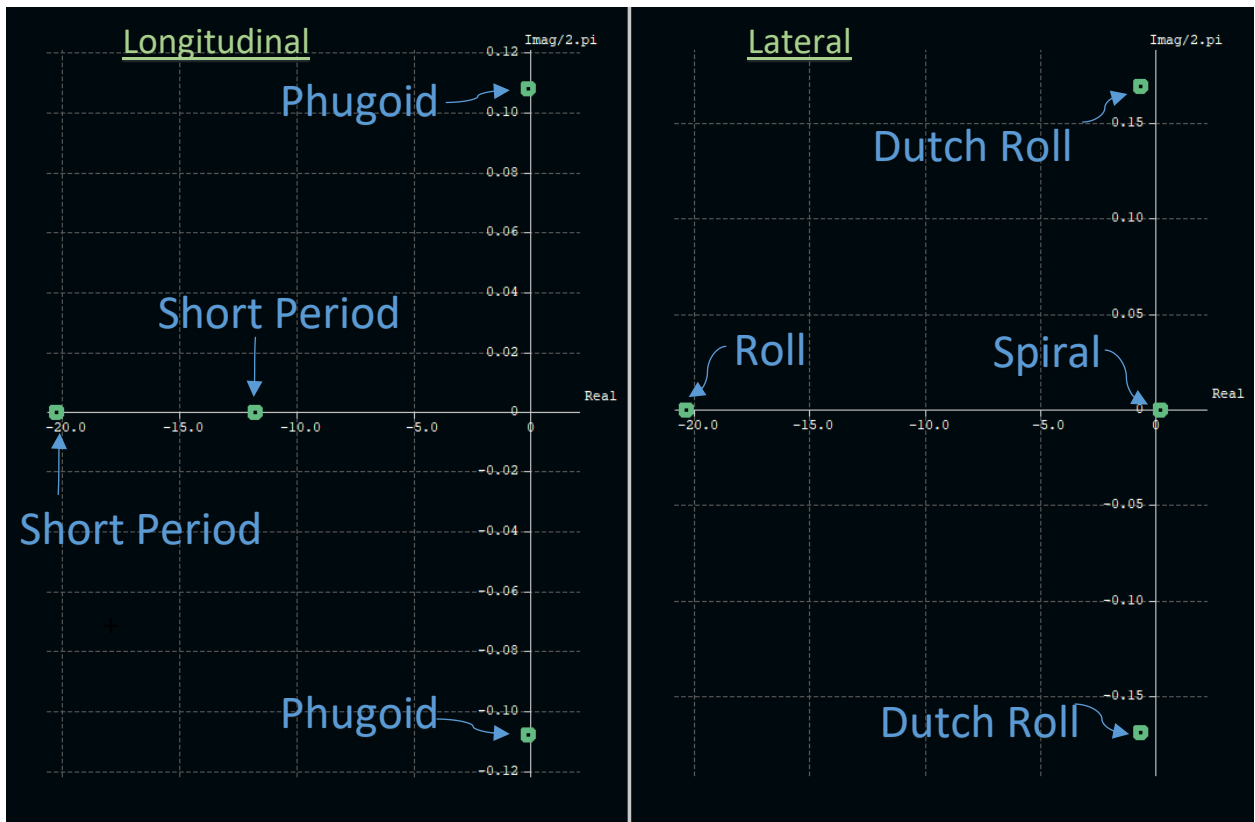
Figure 6-23: Root locus diagram for eigenvalues

All modes except spiral, lead to dynamic stability, which is the goal of this analysis. Spiral mode is a common result to come to divergence and it's up to pilot or flight controller to bring the aircraft in stability. This is a primary dynamic stability analysis that indicates a generally stable aircraft without the intervention of the controller.

Chapter7:

7.1. Conclusion

After all the simulations that took place both in aerodynamics and stability area we can tell that we achieved our goal. The embedded wings UAV can fly with a power consumption of 35.7 watt taking into consideration the drag power of the tail. Furthermore because of the embedded wing design some extra area that was not taken into consideration has come up and add 12 extra solar cells in the tail and another 18 cells on the body of the UAV. Furthermore because of the summer period that the flight will take place we have some thermal ascending air currents that will gain us altitude without the need of motor spinning. The Pixhawk flight controller has integrated thermal searching mode where the plane can only glide and absorb energy without wasting any at moving the propeller. Finally there was enough space for some extra panels both on the fuselage and the horizontal stabilizer. Thus the amount of the panels was raised in 136 and the total energy that is fed to the system is 97.75.

Solar Panels	Area m^2	Power Watt	Drag Power Watt
136	2.125	97.75	35

As we can see from the data presented in the table above the total power balance has a positive result in our system.

7.2. Future work

7.2.1. Experimental Setup

The experimental setup is a necessity for the validation process before proceeding into the manufacturing of the wing. It allows for data to be acquired and compared with the simulation once leaving no room for errors if the experiment is set properly. Due to the time limitation we did not bring the experiment into life and left as future work.

7.2.2. Dynamic Simulation with Control Area Sizing and PID Tuning

The static stability chapter was complete in all of three axis (Yaw, Pitch and Roll) and the UAV provides a decent passive stability as a construction. The further that someone needs to enrich the dynamic stability by introducing the flaps, elevators, rudders, and ailerons of the plane in order to make its response more accurate or fast. To do so a dynamic 6DOF model has to be set in Simulink. We have to refer that the Pixhawk flight controller has embedded onboard real life PID tuning and therefore only some initial values are need in order for the first ascent to take place. Then the auto tuning takes over and defines the gains of each term for the desired response characteristics. If that is not possible then some initial values can be found based on Roskam initial sizing method for the actuation areas.
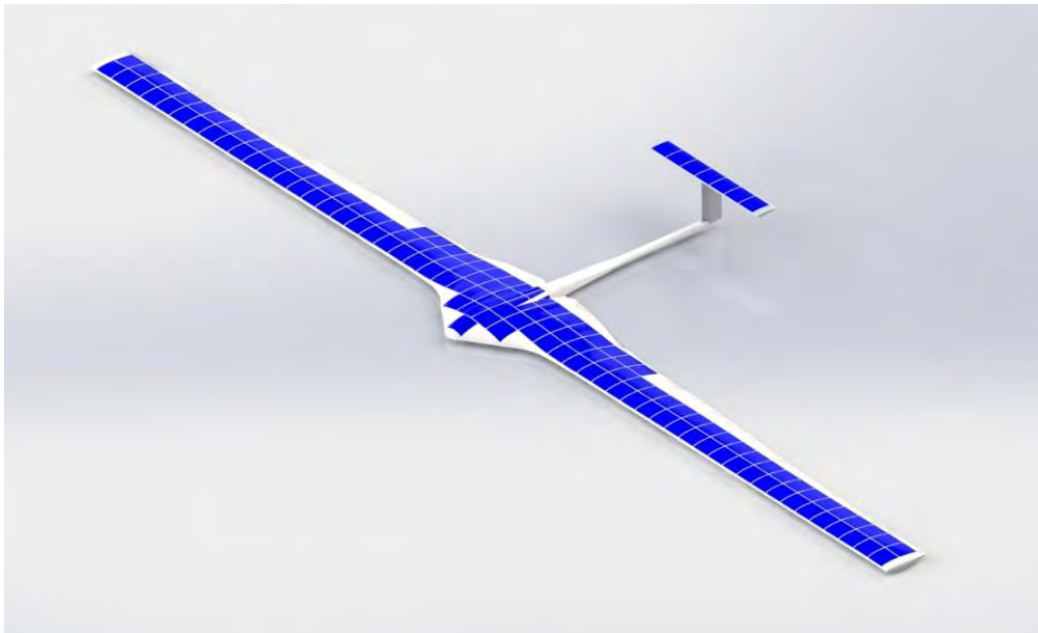
Figure 7-1: Final Model Design
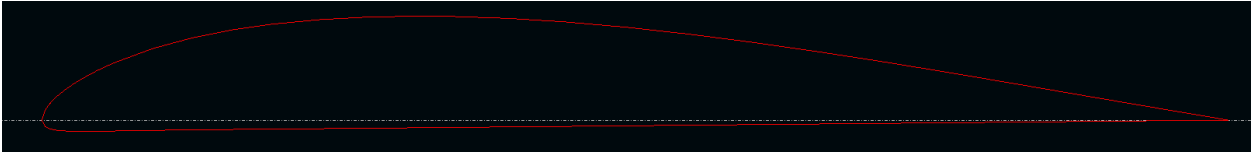
Figure 8-1:Aquila9.3
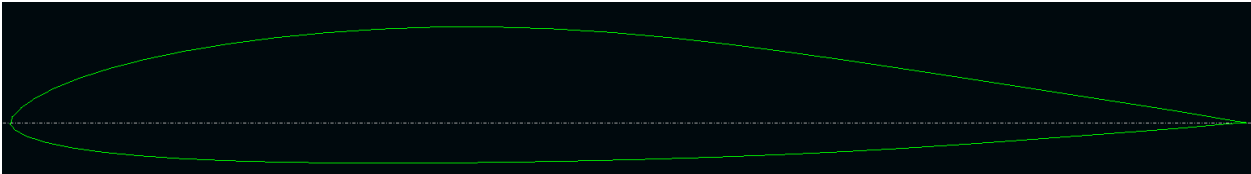
Figure 8-2:E374
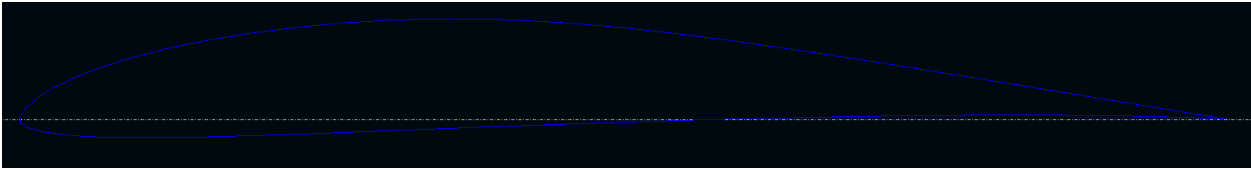
Figure 8-3:E387
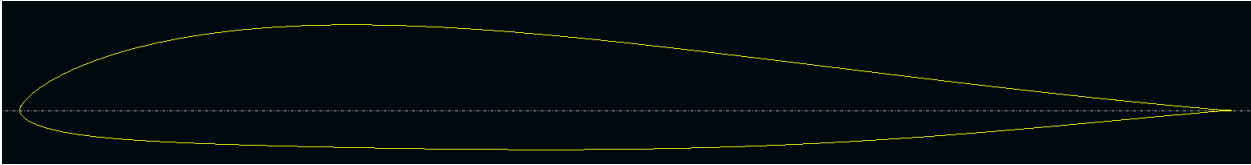
Figure 8-4:EH2_10
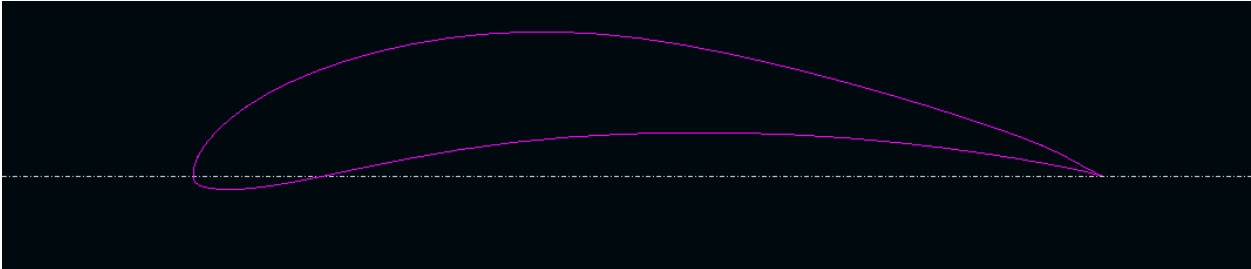
Figure 8-5:EPPLER423
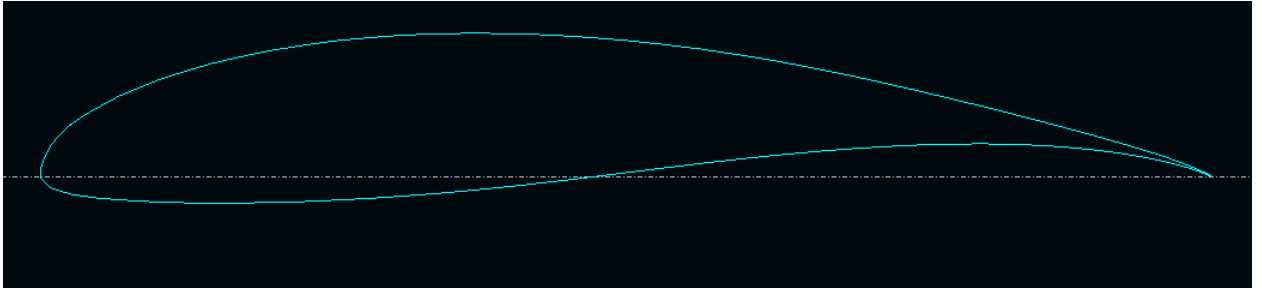
Figure 8-6:FX63137
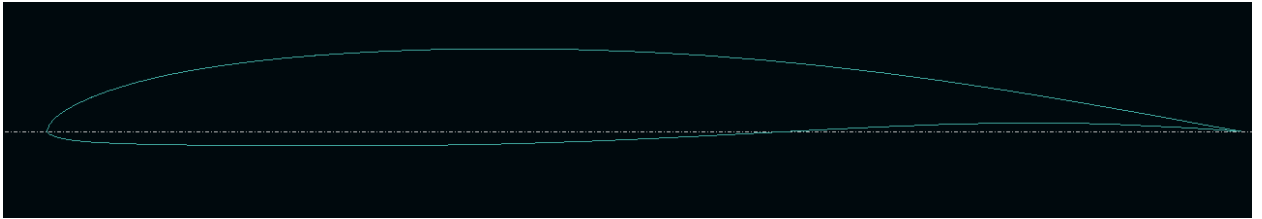
Figure 8-7:HQ3-8B
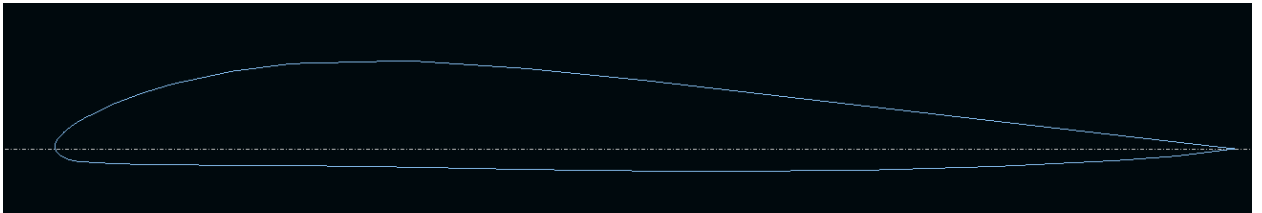
Figure 8-8:HS3_9
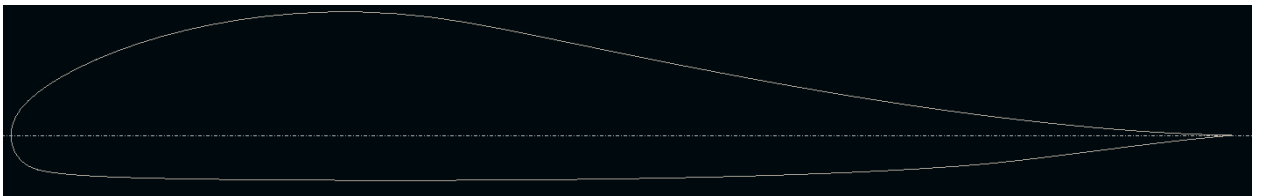
Figure 8-9:LA2573A
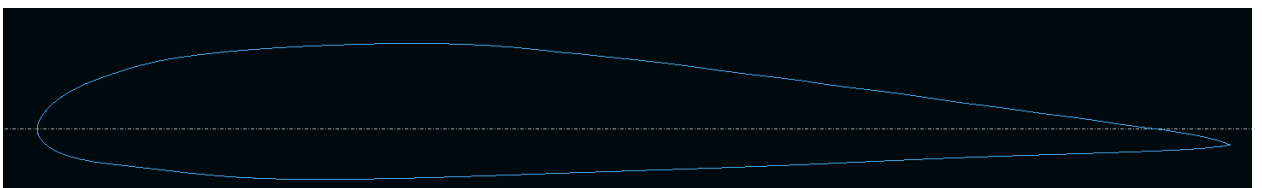
Figure 8-10:LKH2411
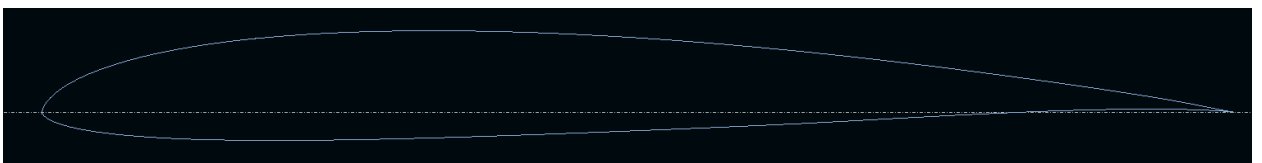
Figure 8-11:MEDIUM_S9000(9%)
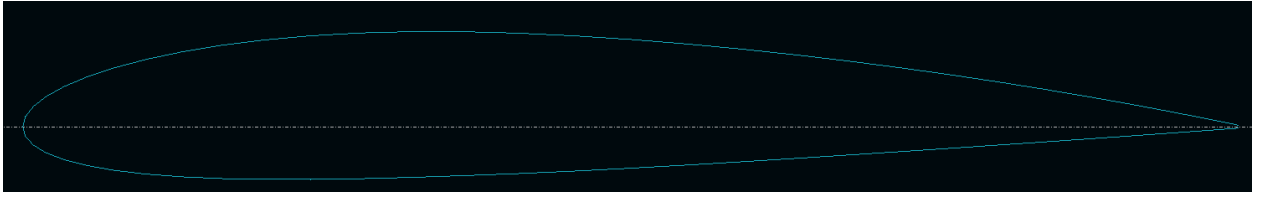
Figure 8-12: NACA2412
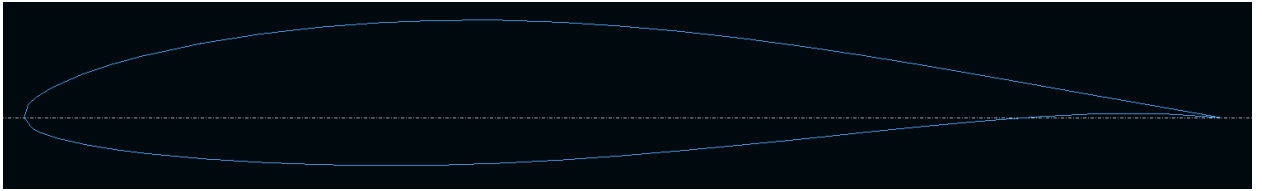
Figure 8-13:NACA63412
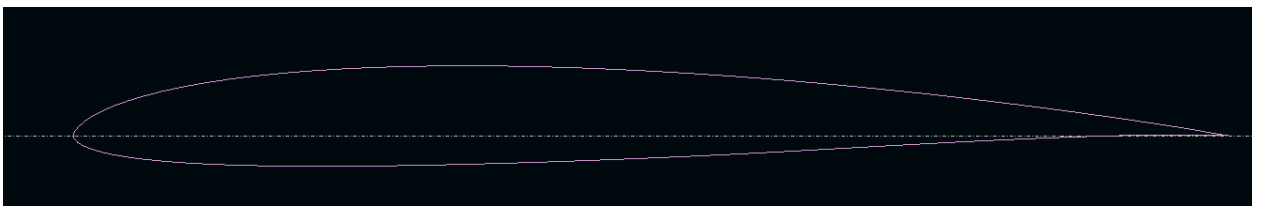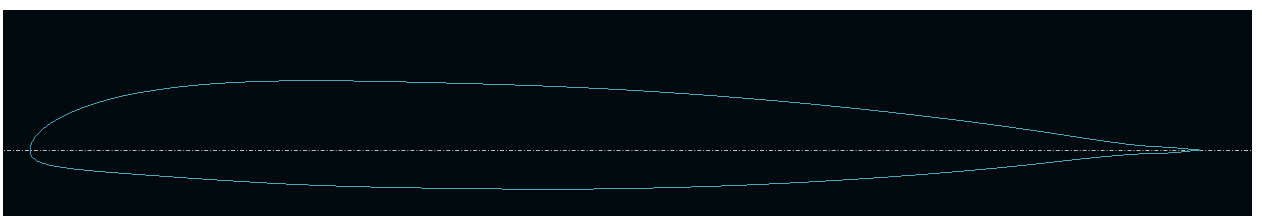

Figure 8-14:NH1036
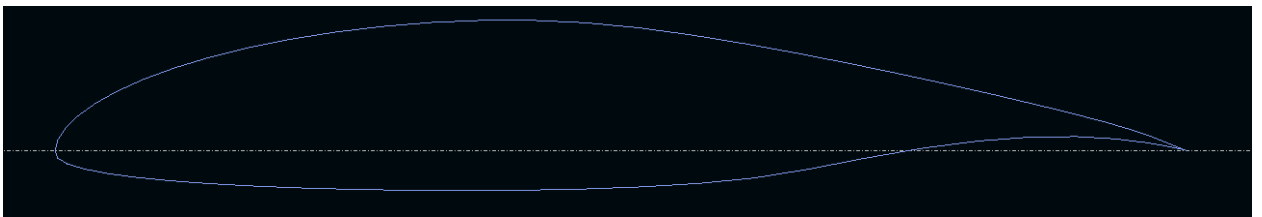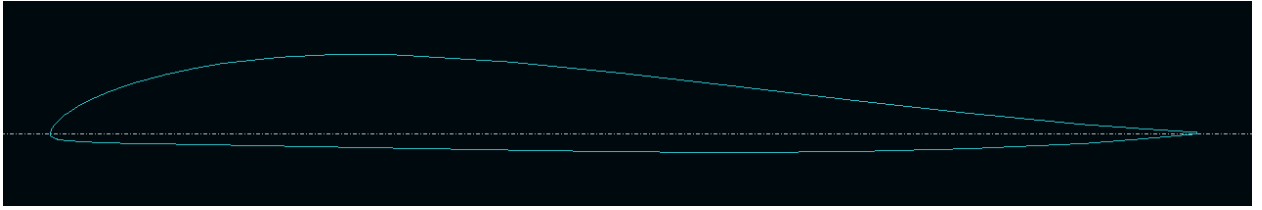

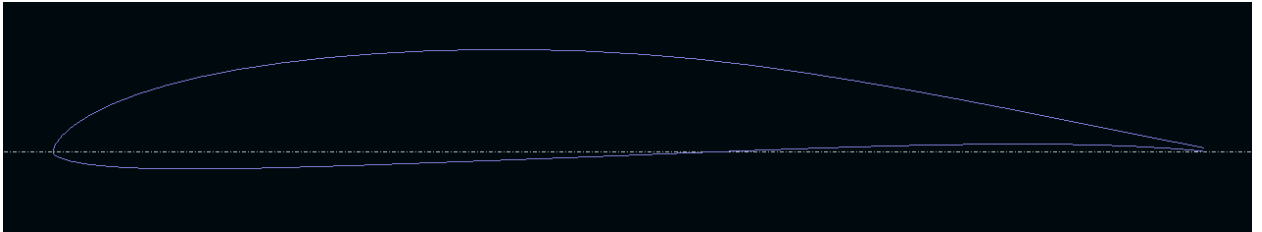Figure 8-15:NLF0215F
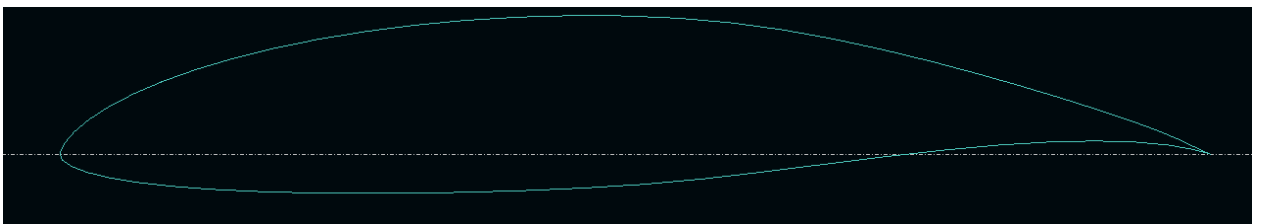
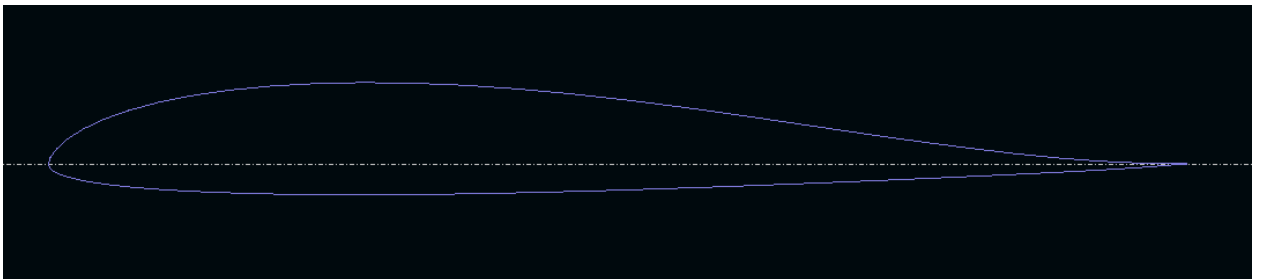Figure 8-16:NLF1015

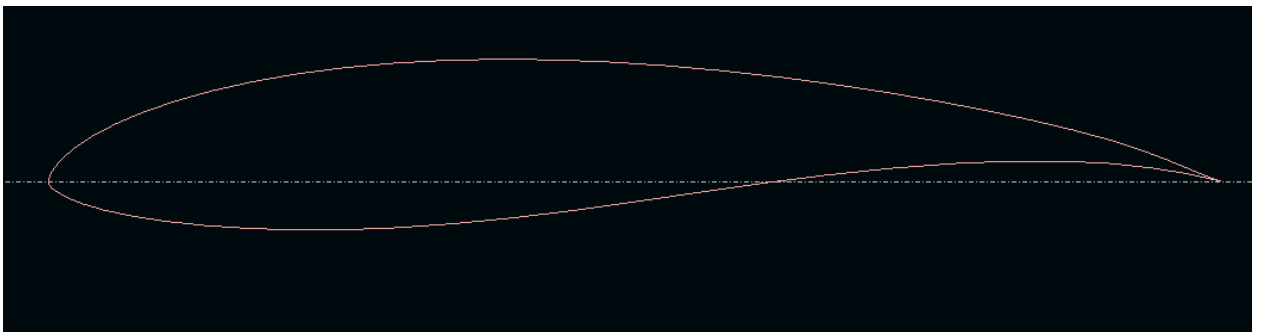Figure 8-17:OA209

Figure 8-18:PHOENIX

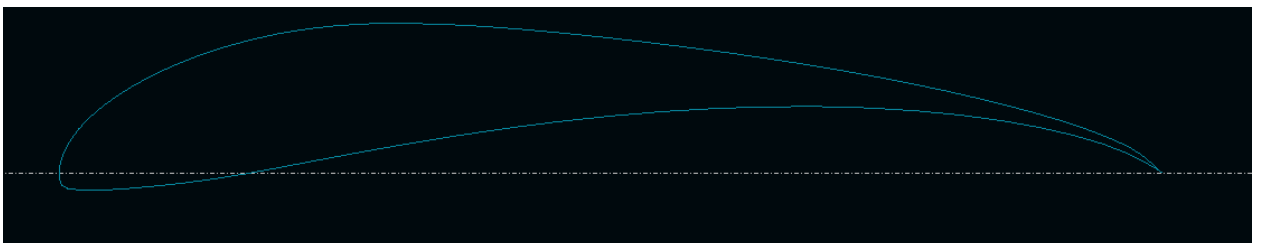Figure 8-19:PSU94-097

Figure 8-20:S510
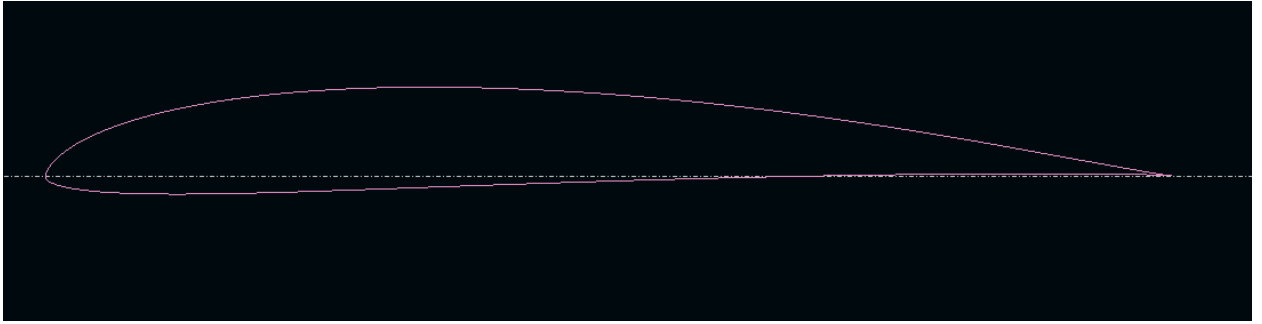

Figure 8-21:S905
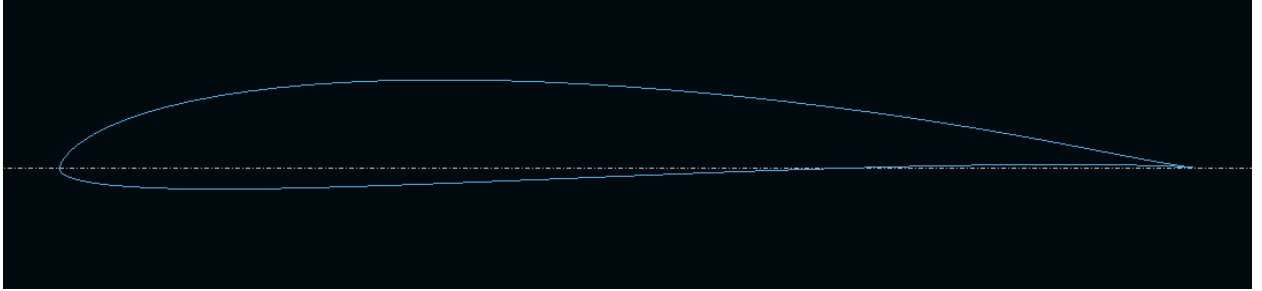

Figure 8-22:SELIG1223
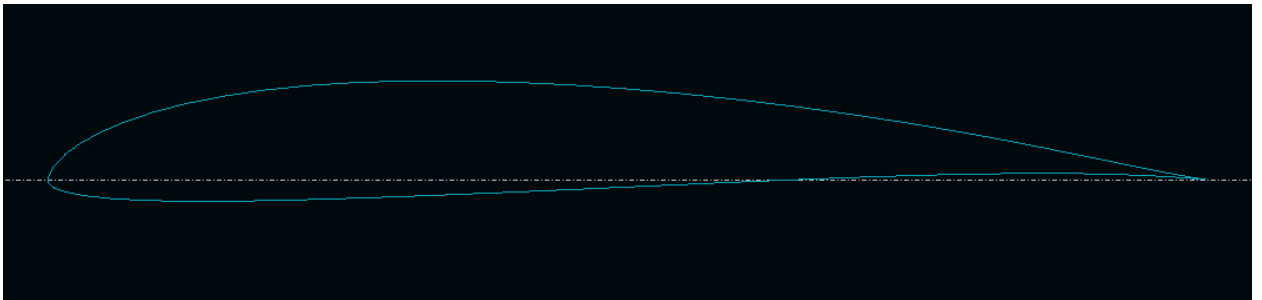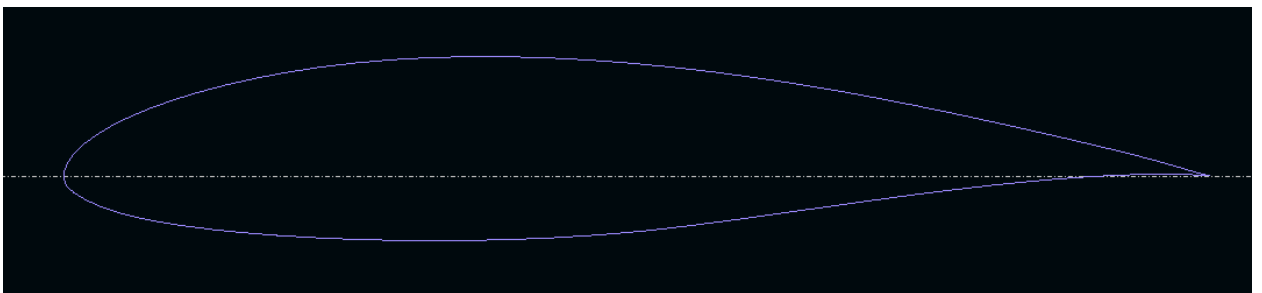
Figure 8-23:S9037

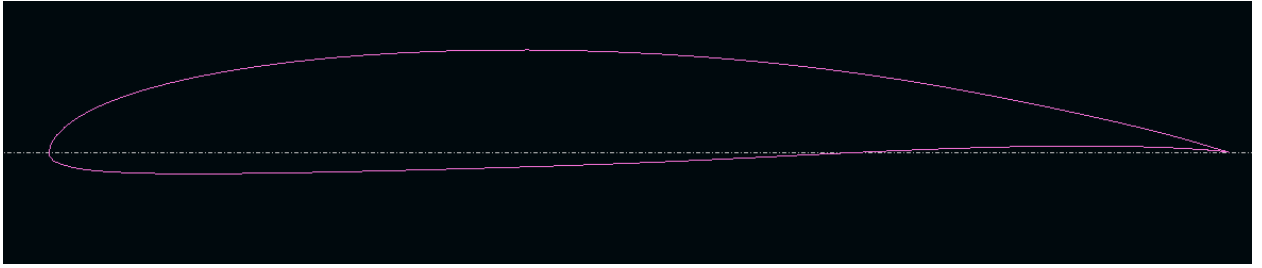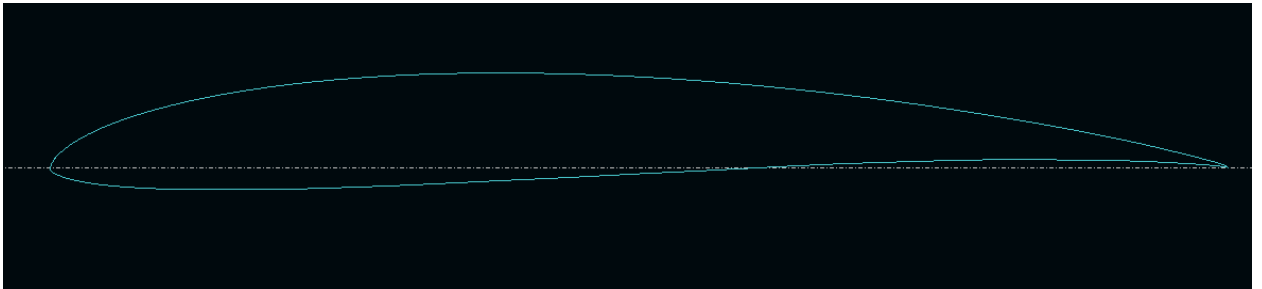Figure 8-24:SA7038

Figure 8-25:SD7032

Figure 8-26:SG6040

Figure 8-27:SG6042

Figure 8-28:WE3.55

Table 8-1: Geometrical Parameters of the Final Wing

FINAL WING DIMENSIONS					
Spanwise	Chord (m)	offset (m)	dihedral(degrees)	Twist(degrees)	Airfoil
0.047	0.78	0.28	0	0.5	psu
0.07	0.76	0.26	0	0.5	psu
0.094	0.74	0.24	0	0.5	psu
0.141	0.73	0.21	0	0.7	psu
0.188	0.7	0.18	0	0.8	psu
0.234	0.66	0.15	0	1.5	psu
0.281	0.62	0.12	0	1.5	psu
0.328	0.575	0.08	0	1.5	psu
0.375	0.54	0.05	0	2	psu
0.422	0.51	0.03	0	2	psu
0.469	0.49	0.015	0	3	psu
0.516	0.47	0.01	0	3	psu
0.563	0.45	0.005	0	3.5	psu
0.609	0.44	0.005	0	4	psu
0.656	0.43	0.005	0	4.5	psu
0.703	0.425	0.002	0	4.5	psu
0.75	0.43	0.001	0	4.5	psu
1.125	0.4	0	0	4.5	psu
1.5	0.4	0	0	4	psu
2.365	0.34	0	0	4	psu
2.775	0.32	0	0	3	psu
3.2	0.3	0	0	0.7	psu
3.378	0.3	0	0	0.3	psu
3.55	0.3	0	0	0	Naca0012

Chapter9: Bibliography

A. Weider, H. L. (2006). *SunSailor: Solar Powered UAV.*

Bruscoli, S. (2011). *Airfoil Optimization for a Solar Powered Aircraft.*

D.Raymer. (1992). *Aircraft Design. A Conceptual Approach.*

Eun-Mi Kwon, K.-H. Y.-J.-Y. (2011). *Design Considerations and Modeling of a Small and Low Altitude Solar Powered UAV.*

Gudmundsson, S. (2014). *General Aviation Aircraft Design Applied Methods and Procedures.*

http://www.airfoiltools.com. (n.d.).

J.Hartney, C. (2011). *DESIGN OF A SMAL SOLAR-POWERED UNMANNED AERIAL VEHICLE.*

Johansson, M. (2011). *Project Solaris – Construction of Solar.*

Joseph Katz, A. P. (2001). *Low speed aerodynamics.*

Karthik Reddy Buchireddy Sri, P. A. (2016). *Design Analysis of Solar-Powered Unmanned Aerial Vehicle.*

Lan, D. J.-T. (1997). *Airplane Aerodynamics and Performance.*

Lee, K. (2004). *DEVELOPMENT OF UNMANNED AERIAL VEHICLE (UAV).*

NOTH, A. (2008). *Design of Solar Powered Airplanes.*

P. Panagiotou, P. K. (2016). *Aerodynamic design of a MALE UAV.*

Parvathy Rajendran, H. S. (2016). *Modelling of solar irradiance and daylight duration for solar-powered UAV sizing.*

Pedro David Bravo-Mosquera, L. B.-B.-G.-M. (2017). *Aerodynamic design analysis of a UAV for superficial research.*

Poonsong, P. (2004). *DESIGN AND ANALYSIS OF A MULTI-SECTION VARIABLE CAMBER WING.*

Sultan, A. (2011). *Project Solaris - The Design of a Solar Powered UAV.*

Tsagarakis, M. (2011). *Project Solaris – Analysis of airfoil for solar powered flying wing UAV.*

Vinayak Bembrekar, A. R. (2018). *Design of a Wing with Bell-shaped Span-load using VLM Method.*

Weisheng Chen, L. P. (2008). *Design and Performance of Low Reynolds Number Airfoils.*

(http://www.airfoiltools.com, n.d.)